2

Solid State Research

1964

Lincoln Laboratory

MASSACHUSETTS INSTITUTE OF TECHNOLOGY

Lexington, Massachusetts

2

Solid State Research

1964

Issued 1 September 1964

Lincoln Laboratory

MASSACHUSETTS INSTITUTE OF TECHNOLOGY

Lexington, Massachusetts

INTRODUCTION

1. SOLID STATE DEVICE RESEARCH

Laser action has been observed at 12°K in diodes of PbTe which had been prepared by diffusing lead into appropriately annealed p-type material. The emitted coherent radiation was at 6.5 microns as compared to 5.2 microns from InSb diodes, the longest wavelength semiconductor laser previously reported. For a diode with a cavity length of 0.62 mm, mode structure has been observed in the spectrum of the output radiation with a spacing between maxima of 67 Å; this should be compared to a value of 59 Å calculated using the room-temperature value of 5.75 for the refractive index and neglecting the dispersion term. The width of the individual modes is less than the 20-Å resolution of the spectrometer used. Lead telluride, a IV-VI compound, is a direct-gap semiconductor and has its band extrema at the edge of the Brillouin zone in the $\langle 111 \rangle$ direction (L-point), rather than at $k = 0$ as in the III-V laser compounds. Thus, in addition to extending the wavelength range of semiconductor lasers to 6.5 microns, we have demonstrated that laser action is not restricted to III-V compounds and may be associated with direct transitions other than those at $k = 0$. The range of semiconductor materials in which laser action should be possible has been further expanded.

Interface-alloy junctions between InAs and GaSb have been studied. In particular, results have been obtained for junctions formed between an A $\{111\}$ face of n-GaSb and a B $\{111\}$ face of p-InAs under an inert gas pressure of 80 atmospheres. Visual microscopic inspection and electron beam microprobing indicate that the junction itself is single crystal and the transition region is approximately 5 microns wide. The heterojunctions when forward biased emit considerable radiation at 0.4 ev (the forbidden energy gap of InAs) and a very much smaller amount of radiation at 0.8 ev (the forbidden energy gap of GaSb). The GaSb acts as a transparent substrate for the 0.4-ev radiation. The photovoltaic response of these heterojunctions has been investigated as a function of the energy of the incident photons. A small relatively constant response is seen for photon energies between that of the two bandgaps and an abrupt increase in photovoltage is observed as the photon energy reaches the bandgap of GaSb. These electro-optical results suggest a band model in which there is a barrier in the conduction band at the heterojunction interface. Such a barrier could be produced by a plane of dislocations in a graded heterojunction and is also predicted by the Anderson model for an abrupt heterojunction, in which case the barrier is caused by the bandgap discontinuity.

In the vapor growth of $(Ga_xIn_{1-x})As$ single crystals, it has been found that 2.75 atomic percent indium produces material that lases at 77°K at a wavelength of 8700 Å which is quite close to the pumping band of the Nd^{+3} paramagnetic ion laser. Work is in progress to grow high-quality crystals of this mixture and decrease the threshold current density from its present value at 77°K of 10,000 amp/cm^2.

The spectrum of the instability in the current through samples of n-GaAs at high electric fields — the Gunn effect — is affected by the value of impedance used to terminate the sample.

For high termination impedance the spectrum is very broad. As the impedance is lowered, a narrow peak begins to appear in the spectrum at $f = v_d/L$ and also at $f = 2v_d/L$. As the impedance is further lowered, the power in the broad-band noise decreases and the peak at $f = v_d/L$ increases in amplitude with a bandwidth that is apparently limited by the length of the voltage pulse applied to the sample. Magnetic effects on the instability have been more carefully investigated. Neither longitudinal nor transverse magnetic fields have any effect on the threshold. Above threshold, the amplitude of the instability is reduced considerably by a transverse field, and to a lesser extent by a longitudinal field, with the longitudinal effect possibly due to misorientation of the sample. The critical electron drift velocity corresponding to the threshold is higher at 77° than at 300°K, contrary to what might be expected for most plasma effects in which there is competition between drift and thermal velocities.

II. LASER RESEARCH

Stimulated Raman emission in nitrobenzene at 90° to the ruby laser beam has been obtained. This is the first step toward constructing a Raman laser which is pumped by an array of ruby lasers at 90° to the Stokes beam and provides further support for certain theoretical models of the Raman laser action. The previously described cylindrical focusing of the ruby beam into a Fabry-Perot cavity was used.[†] Spectral analysis of the 90° Stokes emission indicates that more than four axial modes and a continuum of transverse (or walk-off) modes are oscillating in the Raman cavity. The beam divergence is about 2 mrad, the amount expected for the small cavity that was used. There are strong indications that a stimulated Brillouin-shifted Stokes emission exists at 90°. Estimates of the single-pass gain at 90° are close to previous estimates of the gain at 0°.

Stimulated Raman emission in bromoform occurs in a wide spectrum of combination Stokes and anti-Stokes lines. The data on frequency shifts and emission angles agree with calculations.

Laser properties of grown single crystals of CeF_3 and the transfer of lattice energy which leads to stimulated emission from $CeF_3:Nd^{+3}$ have been investigated. CeF_3 is an interesting laser host because of a direct energy transfer from the lattice to the rare-earth ion, radiative energy transfer due to the intense fluorescence (d→f) of Ce^{+3}, and the rapid depopulation of the terminal laser state within the $F_{7/2}$ lattice absorption. This absorption can also be used to modulate the laser output.

Laser-created gaseous breakdown of air and argon has been studied by means of emission spectra, frame and streak photographs, and magnetic field and pressure effects. The spark temperature is estimated from the spectral continuum to be about 7000°K. The luminous front of the spark grows parallel to the laser beam at about 5×10^5 cm/sec. A DC magnetic field of about 100 kgauss produced no reduction of the breakdown electric field, in agreement with theoretical estimates that diffusion and hence magnetic field effects are negligible. The

---

[†] Solid State Research Report (1964:1), p. 19, DDC 601830.

measured breakdown threshold in argon as a function of pressure (between 20 and 2000 psi) agrees with that observed by Meyerand and Haught.

A pulsed laser dosimeter has been developed to warn of dangerously high laser energy being reflected from surfaces into the eye. The instrument consists of a commercially available gamma-ray detector, used as an electrometer, which is connected in parallel with a photo-tube. When the dosimeter is held to the eye and is pointed at the illuminated surface, the meter reads according to the amount of photocurrent produced by the incident laser light. The safety level was set by clinical data on the critical energy density for retinal damage by spiking ruby lasers with total pulse widths of 175 μsec.

Experimental results have been obtained on the statistics of the photoelectron counts of photo-multipliers illuminated by laser light at 6328 Å, both above and below oscillation threshold. These results indicate that the mean-square fluctuations of a laser oscillating in a single mode are those of a Poisson distribution, while the fluctuations of the noise below oscillation threshold are those of a few narrow-band Gaussian-distributed oscillators. The experimental curves for the mean-square fluctuations as functions of the observation time have yielded estimates for the depth of modulation of the laser output.

Laser oscillation at 2.02 microns in pure xenon has been observed in a 20-cm triode gas laser tube. A gain of 50 percent per meter was measured. The triode structure provides an approximately mono-energetic electron current which should produce population inversion more efficiently than a discharge current. Feasibility of a crossed electron and atom beam high-gain laser experiment is being determined by how low an atom density will still sustain oscillation.

Experiments in which attempts have been made to produce laser oscillation in a mercury-molecule vapor system show promise of output powers at about 5000 Å in the kilowatt range. It is believed that the rapid emptying of the lower state by dissociation yields population inversion during pulsed operation at nearly atmospheric pressure. Power saturation, it is estimated, would occur at about 1-Mw output power.

III. MATERIALS RESEARCH

It has been found that the power output of an RF generator can be conveniently measured by determining the equilibrium temperature of a black-body load with an optical pyrometer and by using the black-body formula to obtain the power radiated by the load. Graphite is an excellent dummy load for studying the output of generators to such relatively high-resistivity loads as plasmas and semiconductors. The pyrometer method has been used to determine the coupling efficiency of a generator as a function of the ratio of load diameter to coil diameter.

Analysis of crystal growth from the vapor shows that constitutional supercooling, which results in instability of the growth interface, can occur in the gas phase as well as in a melt. The analysis yields an expression for the maximum rate of growth from the vapor (v_{max}) which is possible without constitutional supercooling. Evidence for constitutional supercooling has been obtained in experiments on the growth of iodine by forced convection. At sufficiently

low growth rates the interface is smooth, but it becomes rough when the growth rate exceeds a value close to the calculated value of v_{max}.

The temperature dependence of the Seebeck coefficient and resistivity have been measured for polycrystalline samples of CrO_2 and CrO_{2+y}, and for single crystals of Cr_2O_3 and MnO. A molecular orbital energy diagram is proposed for CrO_2 which accounts for the ferromagnetism and metallic conductivity of this compound. An energy diagram is also proposed for Cr_2O_3. According to this diagram, Cr_2O_3 is expected to be a semiconductor with hopping-electron conductivity. The observed electrical properties are consistent with this prediction.

The heat of transformation for the α-β transition in Ag_2Se has been calculated by application of the thermodynamic relation $(dT/dP) = T\Delta V/\Delta H$ to previous data for the pressure dependence of the transition temperature. The value obtained is 2.56 kcal/mole, which is in fairly good agreement with the value of 2.19 kcal/mole measured with a differential scanning calorimeter.

The temperature dependence of the rate at which cubic $PrO_{1.5}$ is transformed into the stable hexagonal form has been investigated by annealing carefully dried samples of the cubic phase in a high-temperature x-ray diffraction camera. The results are consistent with previous data, obtained by x-ray diffraction measurements at room temperature of samples that had been annealed and then quenched, which show that in the range 800° to 850°C the transformation rate rapidly increases to high values.

The high-pressure tetragonal phase of InSb ($InSb_{II}$) and solid solutions of $InSb_{II}$-Sn prepared at high pressure can be retained as metastable phases at atmospheric pressure by cooling them to 77°K before the high pressure is removed. Resistivity measurements made as the temperature slowly increases above 77°K have been used to study the temperature dependence of the rates at which $InSb_{II}$ and the solid solutions are transformed into the zincblende phase ($InSb_I$) stable at atmospheric pressure and into two-phase mixtures of $InSb_I$ and tin, respectively. Rapid transformation occurs for InSb at about 200°K and for the solid solutions at higher temperatures, which increase with increasing tin content.

The room temperature resistance R of $Cd_xHg_{1-x}Te$ samples with x between 0 and 0.20 has been measured as a function of pressure up to 70 kbar. For HgTe, R increases abruptly by four orders of magnitude at about 15 kbar due to a phase transformation from zincblende to cinnabar structure. Similar but smaller increases are observed at somewhat higher pressures in the samples containing cadmium, presumably because of the same transformation. Below the transformation pressure, there are significant changes in R which are probably due primarily to the effect of pressure on the band structure.

The partial pressures of Cd(g) and Te_2(g) in equilibrium with congruently subliming CdTe(c) between 780° and 939°C have been determined by measuring the optical density of the vapor between 2000 and 6000 Å with a double-beam spectrophotometer. The partial pressures are given by $\log p_{Te_2}$ (atmospheres) $= -(1.00 \times 10^4)/T + 6.346$ and $p_{Cd} = 2p_{Te_2}$. The expression for the Gibbs free energy of formation calculated from these equations is in good agreement with the results of electrochemical and effusion experiments at lower temperatures.

Manganese in MnO and cobalt in CoO have been determined by automatic potentiometric EDTA titrations. Automatic titration methods are being developed for the determination of indium, antimony, and tellurium in samples containing these three elements as the major constituents. Satisfactory results have been obtained so far in analyses on samples weighing 0.5 gram or more.

IV. BAND STRUCTURE AND SPECTROSCOPY OF SOLIDS

Several new observations have been made in the magnetospectroscopic investigations of various materials. Reststrahlen reflection has been observed from the surface of HgTe at low temperatures. From these data one obtains values for the lattice absorption frequency, the high-frequency dielectric constant, and the effective charge which are $\nu_o = 3.45 \times 10^{12}$, $\epsilon_o = 14$, and $q^* = 0.6e$, respectively. The data also show a broad absorption band in the same region which may be due to an interband transition.

The magneto-optical reflectivity data from another semimetal, antimony, has also proved interesting. Two types of magnetic behavior were observed: (1) a large magnetoplasma effect and (2) an oscillatory term in the reflectivity, smaller in magnitude than the magnetoplasma effect, but in the same photon energy region. The oscillatory term, which arises from the deHaas-Shubnikov mechanism, leads to results in good agreement with other determinations of the periods along the single-crystal axes. The features of the oscillatory term can be understood on the basis of a simple parabolic conduction band. It is believed that this effect has not previously been observed experimentally.

The indirect transition in germanium has been re-examined using improved measurement techniques, higher magnetic fields and the Faraday configuration. Magneto-absorption data as a function of wavelength show transitions from the valence band edge to the electronic Landau ladders in the conduction band. Superimposed on these large intensity effects is a fine structure due to hole ladders in the valence band. In addition, a spin splitting in the conduction band was observed corresponding to electronic g-factors of 1.8 and 1.5 in the [100] and [110] orientations, respectively. These are in agreement with the theoretical predictions. The Zeeman splitting of the indirect exciton was also observed for various orientations. This effect has been measured in magnetic fields sufficiently high (at the National Magnet Laboratory, M.I.T.) so that the magnetic energy is much greater than the electric energy of the exciton, and a linear behavior is observed. It will be necessary to extend the theory to the high-magnetic-field region to compare with the experimental data.

Measurements in the ultraviolet of the reflectivity of Mg_2Ge show spectral structure in the region between 2.5 and 11 ev. Since the available band structure calculation is limited in accuracy, positive identification of the spectral peaks is not possible at present. It is expected that measurements on Mg_2Si will make identification easier.

Galvanomagnetic measurements on HgTe have been initiated. Rotational measurements of the magnetoresistance, with magnetic field perpendicular to the current, indicated little if any anisotropy. In measurements of the magnetic field dependence of the magnetoresistance

and Hall effects, several interesting effects were observed which are incompatible with a one-band model of the material. However, the experimental results are consistent with mixed electron and hole conduction. The data are additional evidence for the semimetal band model of HgTe. Measurements and calculations are being continued.

A general theory for the Seebeck coefficient tensor in a magnetic field has been developed in terms of symmetry properties. Tables providing easy access to the results of the theory including the spatial symmetry properties are being prepared. These results have been useful in understanding the galvano-thermomagnetic properties of bismuth.

V. MAGNETISM AND RESONANCE

Our present program includes work on three classes of electrons found in solids: broad-band electrons, narrow-band electrons, and localized electrons.

Experimental studies on narrow-band electrons have been hindered by a failure to know what type of material to study. We have shown that there are three classes of transition-metal compounds whose physical properties are dominated by narrow-band electrons, and that all three classes can be found among transition-metal oxides. Primarily ionic compounds which have a cation-cation separation so small that a cation-sublattice d-band is formed are illustrated by high-temperature VO or V_2O_3. Covalent compounds having partially filled π^* bands are illustrated by the bronzes Na_xWO_3 or by metallic ReO_3. Covalent compounds having partially filled σ^* bands are illustrated by metallic $LaNiO_3$. High-temperature VO_2 contains electrons in overlapping cation-sublattice and π^* bands. In order to demonstrate the validity of this explanation of the metallic properties of Na_xWO_3 as against the two proposals extant in the literature, pure ReO_3 and ordered $SrMg_{0.5}Re_{0.5}O_3$ have been prepared and shown to be metallic and semiconducting, respectively.

In order to study the transport properties of the vanadium spinels, which illustrate primarily ionic compounds having a cation-cation separation near the critical separation for collective-electron vs localized-electron behavior, a method has been developed for the preparation of single crystals of controlled chemistry.

The band structure of PbSe is being investigated by cyclotron resonance. A resonance has been observed in p-type material at 70 Gcps and 4.2°K.

A theoretical study of the six-membered hydrogen ring has led to a one-parameter formulation of the electronic wave functions that reduces, for one limit of the parameter, to the molecular-orbital formalism applicable at very small internuclear distances and, for the other limit, to atomic Wannier orbitals with near-neighbor spins correlated antiparallel, which is the correct boundary condition for large separations. A high degree of symmetry makes calculation relatively simple, and the calculated binding energies were better for all separations than those obtained by an alternant-molecular-orbital calculation. The method can be extended to three-dimensional lattices containing two sublattices.

The complex spin configurations of the rare-earth metals can be derived from a Hamiltonian that includes a Ruderman-Kittel exchange interaction and magnetic anisotropy. Exchange

striction has been added to the Hamiltonian, and it is shown that below the Curie temperature there should be an observable sinusoidal variation in the c-axis spacing of the linear and the high-temperature magnetic phase of erbium.

Spin-wave resonance provides an important check on the theory of magnetic exchange interactions. In order to examine some new exchange effects and to obtain the greater accuracy that will be required, this technique has been extended from 10 to 70 Gcps.

Magnetic susceptibility of the compound $MnAs_{0.9}P_{0.1}$ indicates that with decreasing temperature there is spin quenching over the 120°C temperature interval below the $B31 \rightleftarrows B8_1$ transition temperature.

The Jahn-Teller Mn^{3+} ion has been shown to be unique in its destruction of long-range ionic ordering in $Li_{0.5}M^{3+}_{2.5}O_3$ spinels.

Spin-resonance observations in $CoCr_2O_4$ have been extended to 315 Gcps. The spectrum as a function of temperature shows a behavior that extrapolates smoothly from lower frequency data. Although $CoCr_2O_4$ and $MnCr_2O_4$ have complex-spiral spin configurations, neutron diffraction and high-field studies reveal that $MnCr_2S_4$ has a collinear Néel configuration with a $\mu_{Mn} = 4.7 \mu_B$, rather than a spin-only $5\mu_B$ and a Cr-Cr interaction that is ferromagnetic rather than antiferromagnetic.

A calculation of the first-order effect of spin-orbit coupling on a $3d^5$ unperturbed S-state ion in a cubic crystal field has given a new anisotropy contribution to the spin density. In $\alpha - Fe_2O_3$, this new term is the same order of magnitude as the spherical Dzialoshinsky term that contributes to the parasitic ferromagnetism. This term plus the Dzialoshinsky term can account for the highly aspherical ferromagnetic spin-density distribution found in recent neutron-diffraction work.

The temperature dependence of attenuation of 70-Gcps phonons in quartz has been determined. Attenuation measurements, made chiefly on the first echo, have led to a fourth-power dependence with temperature.

TABLE OF CONTENTS

ORGANIZATION

SOLID STATE DIVISION

A. L. McWhorter, *Acting Head*
P. E. Tannenwald, *Assistant Head*
M. J. Hudson, *Assistant*
D. T. Stevenson*

GROUP 81
SEMICONDUCTOR PHYSICS

J. M. Honig, *Leader*
T. C. Harman, *Assistant Leader*

Argyres, P. N.	Kelley, P. L.
Brebrick, R. F.	Kleiner, W. H.
Chapin, D. S.	Mason, V. J.
Dresselhaus, G. F.	Paladino, A. E.
Duston, D. K.†	Rawson, N. B.*
Gottschalk, M.	Sillers, S. J.
Hilsenrath, S.	Trent, P. H.
Houghton, B. H.*	Work, C. C.

GROUP 83
ELECTRONIC MATERIALS

E. P. Warekois, *Leader*
A. J. Strauss, *Assistant Leader*

Andrews, H. I.†	Gardels, M. C.
Bachner, F. J.†	Giardino, N. A.
Banus, M. D.	Kafalas, J. A.
Button, M. J.	LaFleur, W. J.
Carter, F. B.	Lavine, M. C.*
Cornwell, J. C.	Nye, S. D.†
Ehlers, H. H.	Owens, E. B.
Fahey, R. E.	Plonko, M. C.
Farrell, L. B.	Reed, T. B.
Finn, M. C.	Roddy, J. T.
Fischler, S.	Siuta, V. P.†

GROUP 82
MAGNETISM AND RESONANCE

J. B. Goodenough, *Leader*
H. J. Zeiger, *Associate Leader*

Arnott, R. J.	Menyuk, N.
Bermon, S.	Newman, W. A.
Burke, J. W.	Parker, C. D.
Delaney, E. J.	Perry, F. H.
Dwight, K., Jr.	Raccah, P. M.
Feldman, B.	Ridgley, D. H.
Ferretti, A.	Rogers, D. B.
Germann, R. W.	Stickler, J. J.
Kaplan, T. A.	Thaxter, J. B.
Kern, S.	Weber, R.
Kernan, W. C.	Weinberg, D. L.
Larson, E. G.*	Whipple, E. R.

GROUP 84
SOLID STATE SPECTROSCOPY

J. G. Mavroides, *Leader*
G. B. Wright, *Assistant Leader*

Curran, E. A.	Halpern, J.
Dickey, D. H.	Kolesar, D. F.
Dimmock, J. O.	Krag, W. E.
Dresselhaus, M. S.	Mason, W. C.
Edwards, D. F.	Mastromattei, E. L.
Fulton, M. J.	Scouler, W. J.

GROUP 85
APPLIED PHYSICS

R. H. Rediker, *Leader*
R. J. Keyes, *Assistant Leader*

Bates, D. H.	May, W. G.†
Butler, J. F.	Melngailis, I.
Calawa, A. R.	Palermo, J. S.
Caswell, F. H.	Phelan, R. J.
Clough, T. F.	Quist, T. M.
Donaldson, P. L.	Stopek, S.
Foyt, A. G.‡	Sullivan, F. M.
Grant, C. R.	Ward, J. H. R., III
Hinkley, E. D.	Youtz, P.
Hurwitz, C. E.	

GROUP 86
OPTICS AND INFRARED

R. H. Kingston, *Leader*
F. L. McNamara, *Associate Leader*
M. M. Litvak, *Assistant Leader*

Billups, R. R.	Pitts, R. F.
Carbone, R. J.	Rotstein, J.
Chatterton, E. J., Jr.	Schlickman, J. J.
Dennis, J. H.	Soref, R.
DiMarzio, E. W.	Underwood, D. I.
Freed, C.	Wong, G. W.
Longaker, P. R.	Ziegler, H. L.
Merrill, E. R.	Zieman, H. E.
O'Connor, J. R.	Zimmerman, M. D.

*Part Time
† Research Assistant
‡ Staff Associate

REPORTS BY AUTHORS
ENGAGED IN SOLID STATE RESEARCH

15 April through 15 July 1964

PUBLISHED REPORTS

Journal Articles*

JA No.

2253A	The Nernst-Ettingshausen Energy Conversion Figure of Merit for Bi and Bi-4% Sb Alloys	T.C. Harman J.M. Honig S. Fischler	Solid-State Electronics 7, 505 (1964)
2265	Superconductivity in the High-Pressure InSb-Beta-Sn System	S.D. Nye M.D. Banus H.C. Gatos	J. Appl. Phys. 35, 1361 (1964)
2268	Galvanomagnetic Effects in n-Type Germanium	W.E. Krag M.C. Brown	Phys. Rev. 134, A779 (1964)
2270	Partial Pressures in Equilibrium with Group IV Tellurides. I. Optical Absorption Method and Results for PbTe	R.F. Brebrick A.J. Strauss	J. Chem. Phys. 40, 3230 (1964)
2285	Partial Pressures in Equilibrium with Group IV Tellurides. II. Tin Telluride	R.F. Brebrick A.J. Strauss	J. Chem. Phys. 41, 197 (1964)
2293	Growing Helical Density Waves in Semiconductor Plasmas	C.E. Hurwitz A.L. McWhorter	Phys. Rev. 134, A1033 (1964)
2296	Growth of $(Ga_xIn_{1-x})As$ Single Crystals by Vapor Phase Reaction	R.C. Sirrine	J. Electrochem. Soc. 111, 750 (1964)
2303	2000-A Pulse Generator	N.A. Sullivan	Rev. Sci. Instr. 35, 639 (1964)
2307	Impurity States in Semiconducting Masers	H.J. Zeiger	J. Appl. Phys. 35, 1657 (1964)
2372	Lattice Energy Transfer and Stimulated Emission from $CeF_3:Nd^{+3}$	J.R. O'Connor W.A. Hargreaves[†]	Appl. Phys. Letters 4, 208 (1964)
MS-881	AC Susceptibility Measurements on Transition Metal Superconductors Containing Rare Earth and Ferromagnetic Metal Solutes	M. Strongin[‡] E. Maxwell[‡] T.B. Reed	Rev. Modern Phys. 36, 164 (1964)

---

* Reprints available.

† Author not at Lincoln Laboratory.

‡ Division 4.

UNPUBLISHED REPORTS

Journal Articles

JA No.

2305	Diffused Junction Diodes of PbSe and PbTe	J. F. Butler	Accepted by J. Electrochem. Soc.
2332	Partial Pressures in Equilibrium with Group IV Tellurides. III. Germanium Telluride	R. F. Brebrick	Accepted by J. Chem. Phys.
2335	Band Edge Structure of PbS, PbSe, and PbTe	J. O. Dimmock G. B. Wright	Accepted by Phys. Rev.
2344	Galvano-Thermomagnetic Effects in Semiconductors and Semi-metals. IV. Mercury Selenide	T. C. Harman	Accepted by J. Phys. Chem. Solids
2366	Spontaneous Bending of Thin {111} Crystals of III-IV Compounds	M. C. Finn H. C. Gatos	Accepted by Surface Science
2370	Theory of Electromagnetic Field Measurement and Photoelectron Counting	P. L. Kelley W. H. Kleiner	Accepted by Phys. Rev.
2376	Cyclotron Resonance: (Diamag-netic Resonance)	G. F. Dresselhaus	Accepted by Encyclopedia of Physics
2379	The Pulsed Laser Dosimeter: An Optical Safety Monitor	J. J. Schlickman R. H. Kingston	Accepted by Electronics
2383	Partial Pressures and Gibbs Free Energy of Formation for Congruently Subliming CdTe(c)	R. F. Brebrick A. J. Strauss	Accepted by J. Phys. Chem. Solids
2388	Lasers	R. H. Kingston	Accepted by Encyclopedia of Physics
2398	Temperature Dependence of At-tenuation of 70 Gcps Acoustic Waves in Quartz	J. B. Thaxter P. E. Tannenwald	Accepted by Appl. Phys. Letters
2399	Galvano-Thermomagnetic Phe-nomena and the Figure of Merit in Bismuth. I. Transport Properties of Intrinsic Material	T. C. Harman J. M. Honig B. M. Tarmy	Accepted by Advanced Energy Conversion
2405	PbTe Diode Laser	J. F. Butler A. R. Calawa R. J. Phelan. Jr. T. C. Harman A. J. Strauss R. H. Rediker	Accepted by Appl. Phys. Letters
2410	Diamagnetism	J. B. Goodenough	Accepted by Encyclopedia of Physics

Unpublished Reports (Continued)

Meeting Speeches*

MS No.

797A	Growing Helical Density Waves in Semiconductor Plasmas	C. E. Hurwitz	Symposium, Boeing Aircraft Company, Seattle, Washington, 29 June 1964
983A	Stoichiometry of Electronic Materials	A. J. Strauss	Colloquium, Texas Instruments, Inc., Dallas, Texas, 11 June 1964
985A	Experiments on Room Temperature Nernst-Ettingshausen Refrigerators	T. C. Harman J. M. Honig S. Fischler A. E. Paladino	SAE-ASME National Aeronautic and Space Meeting, New York, 27-30 April 1964
989	Concerning the Existence of Subsequioxides of Praseodymium	D. S. Chapin J. M. Honig	Fourth Rare Earth Conference, Phoenix, Arizona, 22-25 April 1964
1001A	Band Edge Structure of PbS, PbSe, and PbTe	J. O. Dimmock G. B. Wright	Seminar, U. S. Naval Ordnance Laboratory, Silver Spring, Maryland, 16 April 1964
1006	Phonon Generation at 70 kMcps	J. B. Thaxter P. E. Tannenwald	PTGMTT International Symposium, New York, 19-21 May 1964
1006A	Generation of Ultrasonic Phonons in Quartz at 70 kMcps	J. B. Thaxter	Physics Seminar, University of Maine, 13 May 1964
1024A	Stimulated Raman Scattering	H. J. Zeiger	Colloquium, Lowell Technological Institute, 6 May 1964
1032	Photographic Emulsions as Ion Detectors in Quantitative Mass Spectrography	E. B. Owens	ASTM Committee E-14 Symposium on Techniques of Solids, McGill University, 10 June 1964
1036	Magnetoreflection Experiments in Pyrolytic Graphite	M. S. Dresselhaus	Seminar, Purdue University, 9 April 1964; Seminar, M.I.T., 14 April 1964; Seminar, Ohio State University, 2 June 1964
1061	Thermal Plasmas: Part I. Calculation of Equilibrium Plasma Properties Using Linear Plasma Thermodynamics	T. B. Reed	American Physical Society, Washington, D. C., 27-30 April 1964
1062	Thermal Plasmas: Part II. Plasma Flame Temperature Measurement Using Aureole Isotherms	T. B. Reed	

---

* Titles of Meeting Speeches are listed for information only. No copies are available for distribution.

MS No.

1093A	Stimulated Raman Processes	H.J. Zeiger	General Telephone and Electronics Laboratories, Bayside, New York, 28 May 1964
1096	Interface–Alloy Epitaxial Heterojunctions	R.H. Rediker S. Stopek J.H.R. Ward	The Electrochemical Society, Toronto, Canada, 3-7 May 1964
1104	Syllabus Pertaining to Physical Adsorption of Gases on Solids	J.M. Honig	Summer Conference Lecture, University of Michigan, 25-27 May 1964
1110	Principles of Injection Lasers	R.H. Rediker	IEEE Computer Elements Sub-committee, Atlantic City, New Jersey, 16-17 April 1964
1116	Transition–Metal Oxides with Metallic Conductivity	J.B. Goodenough	Conference on the Structure and Properties of Dielectric Materials, M.I.T., 16-17 June 1964
1119	Injection Lasers	I. Melngailis	Seminar, Carnegie Institute of Technology, 16 April 1964
1121	Optical Maser Spectra Deduced from Photoelectron Counting	C. Freed H.A. Haus*	Twenty–Second Annual Conference on Electron Device Research, Cornell University, 24-26 June 1964
1125	Electrochemical Dember Effect in Semiconductor	W.W. Harvey M.C. Finn	International Conference on Physics and Chemistry of Solid Surfaces, Brown University, 21-26 June 1964
1127	Galvano–Thermomagnetic Effects in Semiconductors and Semimetals. IV. Mercury Selenide	T.C. Harman	Seminar, M.I.T., 8 May 1964
1130	Transfer Characteristics and Spectral Response Measurements on Infrared	R.R. Billups L.D. Miller*	IRIS Specialty Group Meeting, Santa Barbara, California, 16 June 1964
1136	Gunn Effect in GaAs	A.G. Foyt A.L. McWhorter	
1137	Properties of InAs–GaSb Interface–Alloy Junctions	E.D. Hinkley R.H. Rediker	IEEE 1964 Solid State Device Research Conference, Boulder, Colorado, 1-3 July 1964
1148	Injection Luminescence in PbTe Diodes	J.F. Butler A.R. Calawa R.J. Phelan, Jr. T.C. Harman A.J. Strauss R.H. Rediker	

* Author not at Lincoln Laboratory.

Unpublished Meeting Speeches (Continued)

MS No.

| 1142 | Magnetoreflection Experiments in Antimony | M.S. Dresselhaus | Seminar, National Magnet Laboratory, M.I.T., 23 June 1964 |
| 1147 | Valence-Bond-Molecular Orbital Study of an Hexagonal Ring of Hydrogen Atoms | E.G. Larson W.R. Thorson* | Symposium on Molecular Spectroscopy, Ohio State University, 15 June 1964 |

---

* Author not at Lincoln Laboratory.

I. SOLID STATE DEVICE RESEARCH

A. PbTe DIODE LASER

Since the original development of the GaAs diode laser,[1-3] laser action has been reported in other direct-gap III-V compounds, namely InAs,[4] InP,[5] and InSb[6,7] as well as <u>alloys</u> of III-V compounds.[8-10] We have now observed laser action in diodes of PbTe, a IV-VI compound. Lead telluride, also a direct-gap semiconductor,[11] has band extrema at the edge of the Brillouin zone in the $\langle 111 \rangle$ direction (L-point),[11] rather than at k = 0 as in the lasing III-V compounds. Laser action in PbTe diodes occurs at 6.5 microns as compared to 5.2 microns from InSb diodes, the longest wavelength semiconductor laser previously reported.

The diode lasers were prepared from single-crystal p-type PbTe wafers which were spark-cut from a Bridgman grown ingot. By annealing 1.5-mm-thick wafers at 600°C for 12 days under a tellurium vapor pressure produced by pure tellurium at 287°C, the carrier concentration at 77°K was reduced from 4×10^{18} cm^{-3} to 7×10^{17} cm^{-3} in agreement with the results of Sato, <u>et al</u>.[12] The n-p junction was formed by heating a cleaved sample with a two-phase lead-rich PbTe ingot in an evacuated quartz ampoule at 450°C for one hour.[13] A junction depth of 20 microns below a cleaved (100) surface was obtained. A Fabry-Perot cavity with parallel reflecting faces was formed by cleaving two planes perpendicular to the n-p junction. Typical dimensions of lasers are 0.62 × 0.25 × 0.25 mm, the longer dimension being the distance between the reflecting faces. Diodes have also been fabricated from unannealed PbTe but the intensity of the injection luminescence from these diodes was orders of magnitude below the incoherent luminescence of diode lasers made from appropriately annealed material. Unannealed PbTe also has shown significantly less photoluminescence than the annealed material, in agreement with the results of Washwell and Cuff.[14]

To measure the radiation, the diodes were mounted on a conduction cooled block of a liquid helium dewar with CaF$_2$ windows. Forward current was supplied in 2-μsec pulses. Figure I-1(a) shows the spectra above and below threshold for a diode operating at a temperature of 12°K. The spectra have been normalized to illustrate line narrowing. The intensity of the radiation above threshold is about two orders of magnitude higher than that below threshold. The short wavelength peak of the spectrum below threshold increases superlinearly with current and more rapidly than the broad portion of the spectrum. Experiments with diodes of larger area have shown that this peak disappears at sufficiently low current densities. The mode structure of the laser line, omitted from Fig. I-1(a) for simplicity, is shown in Fig. I-1(b) in which the laser line is plotted on an expanded wavelength scale. The average wavelength separation between the modes in Fig. I-1(b) is 67 Å. Using the usual expression for the mode spacing in a Fabry-Perot cavity, a value of 5.75 for refractive index[15] and neglecting the dispersion term, the mode separation is calculated to be 59 Å for the cavity length of 0.62 mm. This value is in good agreement with the experimental result. In calculating the spacing of 59 Å we have used the room-temperature value of the refractive index and have neglected its dispersion. As can be seen from the figure, the 20-Å width of the main peak in Fig. I-1(b) is resolution limited.

(a)

(b)
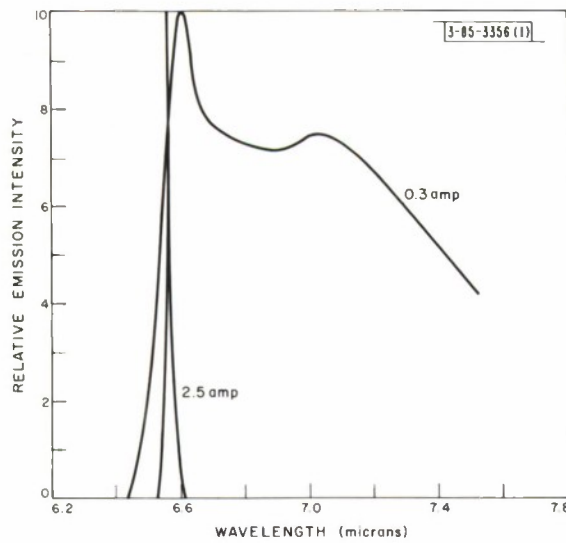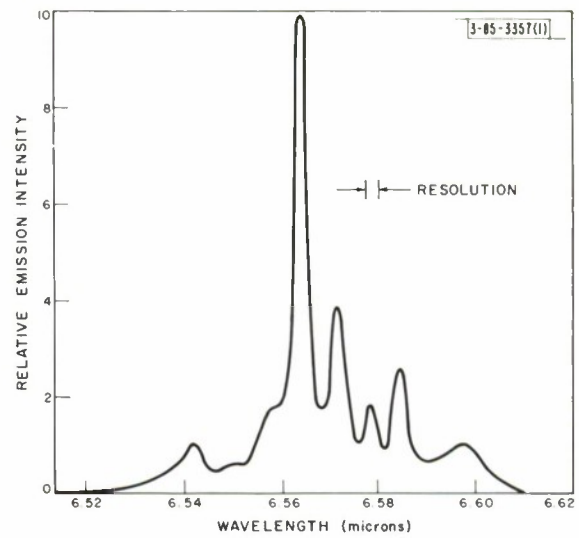
Fig. I-1. Spectra of infrared emission from cleaved surface of PbTe diode at 12°K below (0.3 amp) and above (2.5 amp) threshold for laser action. The mode structure of the 2.5-amp line, omitted for simplicity in (a), is shown on an expanded wavelength scale in (b).
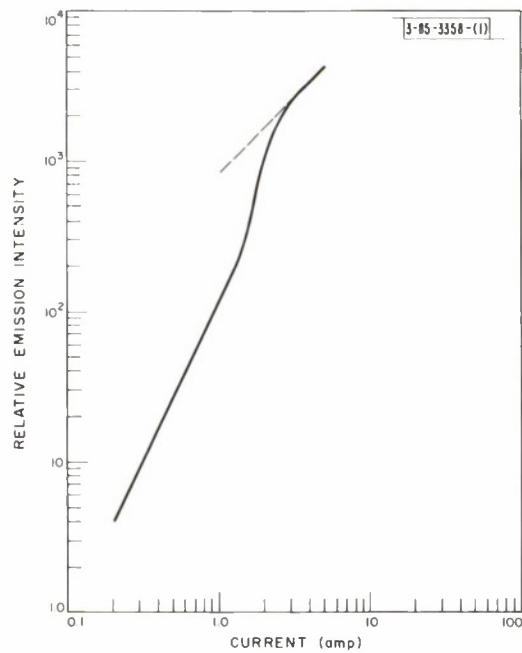

Fig. I-2. Light emission from cleaved surface of PbTe diode as a function of current at 12°K.

Figure I-2 is a plot of radiation intensity from the cleaved end of the diode as a function of forward diode current. The superlinear behavior of this curve between 0.2 and 1.7 amp reflects the rapid growth of the short wavelength peak exhibited at 0.3 amp in Fig. I-1(a). The increase in slope at about 1.7 amp indicates the onset of laser action and gives a threshold current density of 1100 amp/cm^2. Results of observations on the spectrum of the radiation as a function of current confirm this threshold value. Note on the figure that the slope becomes linear at high currents, as is expected if the quantum efficiency reaches a limiting value.

In addition to extending the wavelength range of semiconductor lasers to 6.5 microns, we have demonstrated that laser action is not restricted to III-V compounds and may be associated with direct transitions other than those at k = 0. Thus, the range of semiconductor materials in which laser action should be possible has been further expanded.

J. F. Butler   T. C. Harman
A. R. Calawa   A. J. Strauss
R. J. Phelan, Jr.   R. H. Rediker

B. PROPERTIES OF InAs-GaSb INTERFACE-ALLOY JUNCTIONS

We are attempting to correlate the results of metallurgical, electrical, and electro-optical measurements made on interface-alloy junctions between dissimilar semiconductors. Such junctions have been fabricated between GaAs and Ge,[16] GaAs and GaSb,[16] and between InAs and GaSb.[17] Junctions made between InAs and GaSb are of particular interest because these two semiconductors represent a combination having approximately equal lattice constants in which the higher energy gap material has the lower melting point.

The fabrication technique for producing InAs-GaSb interface-alloy junctions is illustrated in Fig. I-3. The semiconductor disks which are 0.010 inch thick are placed on a carbon heater strip. By passing a current through the heater strip, a temperature gradient is set up across the pair of semiconductors so that the InAs, which has the higher melting point, is at a higher temperature than the GaSb. The temperature is increased to the point where, under microscopic observation, the bottom face of the GaSb (the hottest part of this material) is observed to melt at the interface with the InAs. Heater strip current is then turned off. An inert gas pressure of 80 atmospheres is maintained in the chamber in order to reduce loss of arsenic from the InAs at the high temperatures involved.
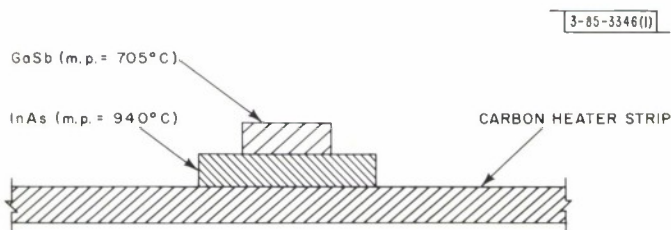

Fig. I-3. Experimental arrangement for InAs-GaSb interface-alloying. An inert gas pressure of 80 atmospheres is maintained in order to reduce deterioration of the InAs surface at the high temperatures involved.
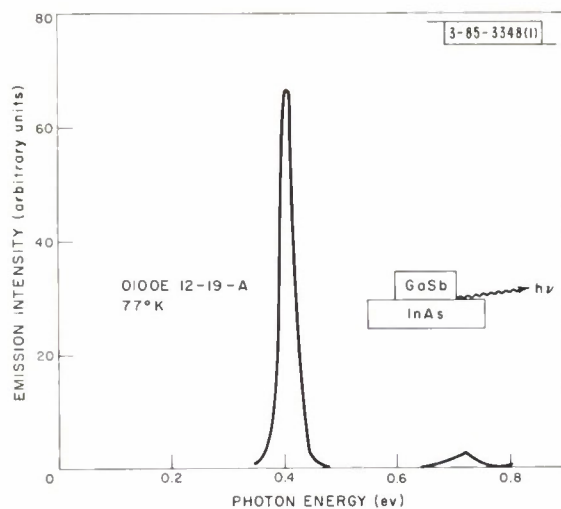
Fig. I-4. Infrared emission spectrum of a forward-biased InAs-GaSb p-n junction. Radiation emanating from the edge of the junction is being detected. The large intensity at 0.4 ev indicates injection of carriers from the wide bandgap to the narrow bandgap semiconductor. Junction current density is approximately 1000 amp/cm².
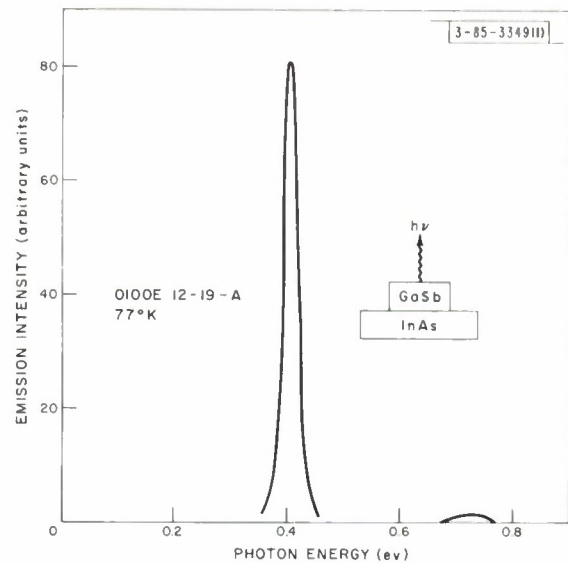
Fig. I-5. Infrared emission spectrum of a forward-biased InAs-GaSb p-n junction. Radiation is detected after having passed through the larger bandgap GaSb. Junction current density is approximately 1000 amp/cm².

Fig. I-6. Photovoltaic spectral response per incident photon of an InAs-GaSb p-n junction at 77°K. Incident radiation is directed toward the junction edge.

Fig. I-7. Energy-band diagram of an n-p heterojunction (after Anderson[20]). The dashed lines are for on applied voltage V.

Prior to the alloying procedure the InAs and GaSb disks were polished and etched. The etch consisted of a 10-percent solution of bromine in methyl alcohol. Furthermore, for $\{111\}$-oriented disks, the etch pits were used to diff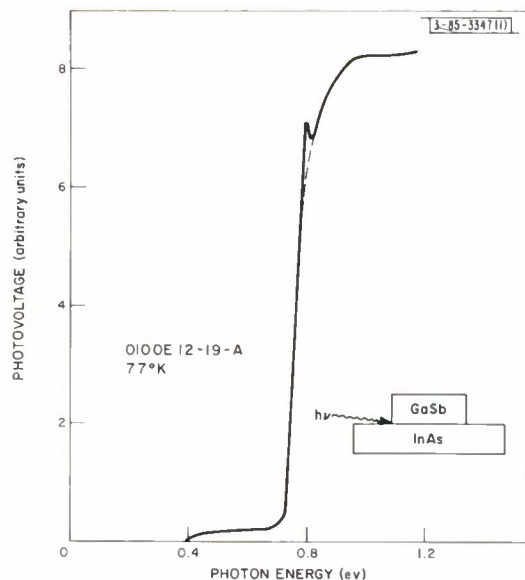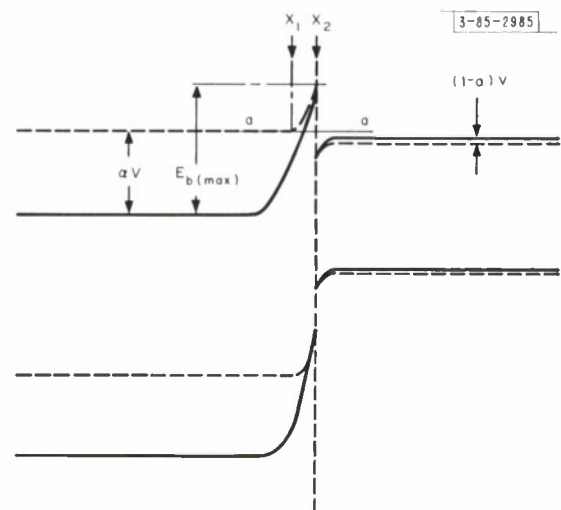erentiate between the A- and B-surfaces. The results described here are from junctions formed between an A$\{111\}$ face of GaSb and a B$\{111\}$ face of InAs. The GaSb is n-type, tellurium doped, with a carrier concentration of approximately $10^{17}/cm^3$. The InAs is p-type, zinc doped, with a carrier concentration of $5 \times 10^{17}/cm^3$.

After alloying, some of the junctions were prepared for metallurgical investigation by lapping and polishing in a plane perpendicular to the junction. Visual inspection, electron-beam microprobing, and Kossel pattern analysis constitute the metallurgical program.

Microscopic inspection of the etched cross section showed that the junction itself was free of any visible imperfections. Although in some cases a crack has been observed in the InAs in a region away from the junction, it is not certain whether these cracks were produced by strains set up during the interface-alloying or in the subsequent handling. The GaSb has shown grain boundaries in the recrystallized region, but these were also well away from the junction.

The results of electron beam microprobing indicate the transition region to be approximately 5 microns wide. This is concluded on the basis of the interdiffusion of the four elements constituting the host semiconductors. Kossel line experiments, which can tell us about the single-crystal nature of the junction, are presently under way for the InAs-GaSb system. Although we have no results on this system as yet, Kossel patterns for GaAs-GaSb heterojunctions,[16] in which the lattice mismatch is much larger, and for GaAs-Ge junctions, indicate that interface-alloying does produce single-crystal junctions.

Ohmic contacts were alloyed to the InAs-GaSb p-n junction in preparation for the electrical and electro-optical experiments. The infrared emission and photovoltaic experiments to be described were taken with the diode immersed in liquid nitrogen.

Figure I-4 illustrates the spectral distribution of the infrared emission from the edge of a forward-biased junction. The large emission intensity at 0.4 ev (the forbidden energy gap of InAs) indicates injection of electrons from the n-type GaSb into the p-type InAs, where radiative recombination takes place. (A small amount of emission is also observed at an energy near the GaSb bandgap.) We believe that these results show that we have wide-bandgap emission as originally proposed by Shockley[18] and Kroemer.[19] In Fig. I-5 it is clear that the GaSb is acting as a transparent substrate for the InAs radiation, which is to be expected.

Monochromatic incident radiation produced a detectable voltage across the junction. A plot of this photovoltaic response is shown in Fig. I-6. No photovoltage is observed below the energy gap of the InAs. In the region between the energy gaps, a small, relatively constant response is seen. An abrupt increase in photovoltage is observed as the incident photon energy reaches the GaSb energy gap. The spike occurring at 0.8 ev is probably caused by a surface trapping mechanism. This is a DC phenomenon occurring when the incident light is chopped at 13 cps, but disappearing, as indicated by the dashed line, when the chopping rate is increased to 800 cps. Futhermore, the spike is virtually eliminated by etching the diode surface immediately prior to the photovoltaic measurements. The spectral distribution of the photocurrent, obtained by shunting the diode, is essentially identical to the photovoltaic results shown in Fig. I-6.

These electro-optical results suggest a band model for the InAs-GaSb p-n junction which, in its simplest form, is shown in Fig. I-7. This is a model originally proposed by Anderson[20]

for abrupt Ge-GaAs p-n heterojunctions. The salient feature of this model is the barrier in the conduction band at the interface. A barrier produced by a plane of dislocations in a nonabrupt heterojunction can also explain the results. We feel that our results are too preliminary at this time to distinguish between the details of these two models, although chemical analysis indicates a graded heterojunction.

The solid lines in Fig. I-7 represent the equilibrium situation with no applied voltage. Application of a forward bias changes the band picture to that shown by the dashed lines. When the forward bias is such that the electrons in the GaSb have an energy equal to that of allowed states in the InAs, then tunneling through the barrier can occur. The tunneling is represented here by the line a-a. That tunneling is the major transport mechanism is indicated on the basis of the I-V measurements made at 77° and 300°K. The forward current was found to vary as $I_o \exp[AV]$, the value of A being approximately $14.4 \, V^{-1}$.* Radiative recombination of the minority carriers in the p-type InAs yields the observed radiation corresponding to the InAs bandgap. Also, since the energy of the radiation is substantially less than the forbidden energy gap of GaSb, the absorption coefficient in this material is low and the GaSb acts as a transparent substrate.

The photovoltaic measurements can also be explained on the basis of the model shown in Fig. I-7. At photon energies less than the InAs gap, carriers are not created to any detectable extent by the incident radiation. Between 0.4 and 0.8 ev, electron-hole pairs are generated at the junction on the InAs side. The electrons produced in the p-type InAs are trapped in the notch. The electrons in the notch will tend to tunnel through the barrier, and since the junction is open-circuited it will forward bias itself in order to create an equal (but opposite) current so that the net current is zero. Thus, we have a small photovoltage produced — it is small because the tunneling probability is small — and in the short-circuit case, a small photocurrent for incident radiation between the bandgaps. At photon energies larger than the forbidden gap of GaSb, electron-hole pairs are created in this n-type semiconductor. Holes produced within a diffusion length of the junction are swept into the InAs and are responsible for the large photovoltaic response above 0.8 ev.

E. D. Hinkley
R. H. Rediker
Mary C. Lavine

C. GROWTH OF $(Ga_xIn_{1-x})As$ SINGLE CRYSTALS BY VAPOR PHASE REACTION

Lasers have been fabricated from mixed crystals of $Ga_xIn_{(1-x)}As$ which were grown from the vapor phase in a closed system. When the doping level is in the range of $(5-10) \times 10^{17}/cm^3$, the threshold currents and light output are comparable to that of pure GaAs lasers. In all cases observed so far, the laser line is at higher energy than the low-current spontaneous peak. For example, a crystal with a nominal indium concentration of 2.3 atomic percent had its spontaneous peak at 8600 Å at a current density of $\sim 300 \, amp/cm^2$ and at 77°K. On the other hand, when this material lased at a current density of $\sim 3000 \, amp/cm^2$ the coherent radiation was at 8520 Å. The uniformity was good, three out of four diodes having lased at essentially identical current densities and wavelengths.

_____

* These results are similar to those which have been obtained in GaAs-GaSb junctions (Ref. 16) in which the forward current was found to vary as $I_o \exp[AV]$ over a range of temperatures from 77° to 400°K.

6

A number of crystals richer in indium have been grown. One of them, with a nominal 2.75 atomic percent indium concentration, has lased at just over 8700 Å, which is quite close to the Nd^{+3} pump band. In this particular case, the threshold current density was $\sim 10,000\,amp/cm^2$ at 77°K, probably because the mechanical properties of the crystal caused erratic cleaving and produced a poor optical cavity. Several other crystals with similar indium concentrations have been grown and are in process of evaluation.

S. Stopek

D. GUNN EFFECT IN GaAs

1. Introduction

During the past quarter, further work has been done on the Gunn effect[21] in n-type GaAs. This report will include the effects of termination impedance, as well as additional results on the magnetic field and temperature dependence of the instability.

The circuit used for these experiments is shown in Fig. I-8. The sample, which is terminated on either side by resistors of smaller value than the sample resistance, sees an impedance

MEASURING CIRCUIT

TYPICAL SAMPLE
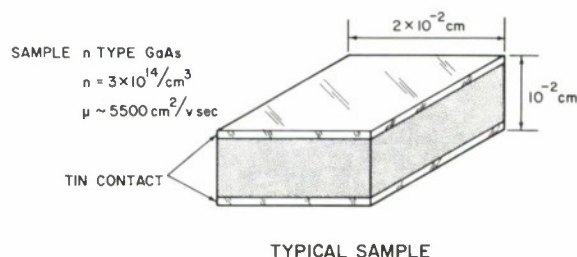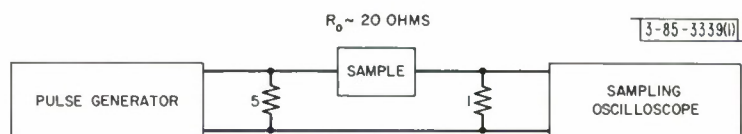
Fig. I-8. Diagram of measuring circuit for Gunn effect.

that is smaller than its static resistance. Also, the electrical path around this loop (sample plus two resistors) has been kept short so that the stray inductance is minimized. This termination impedance has a strong effect on the instability, as will be discussed later. Voltage is applied to the sample from a delay-line pulse generator, used to avoid heating the sample. The voltage across and the current through the sample are observed with a sampling oscilloscope.

Figure I-8 also shows typical sample parameters and dimensions. The upper and lower faces of the sample, which have the alloyed contacts, are lapped and etched, while the side faces are cleaved. The sample length of 10^{-2} cm corresponds to a frequency of about 1 Gcps.

Typical voltage-current curves are shown in Fig. I-9 both for room temperature (300°K) and 77°K. The curves are linear (ohmic) for low electric fields and begin to bend slightly as the

7

Fig. I-9. Voltage vs current for a typical sample at 300° and 77°K.

Fig. I-10. Voltage vs time and current vs time for a typical sample at 300°K.

Fig. I-11. Current vs time from Fig. I-10 on expanded time scale.

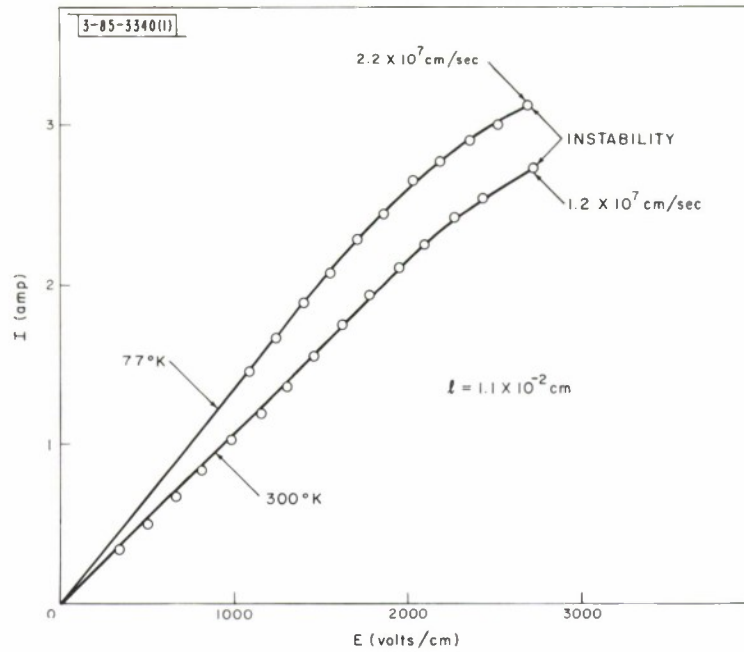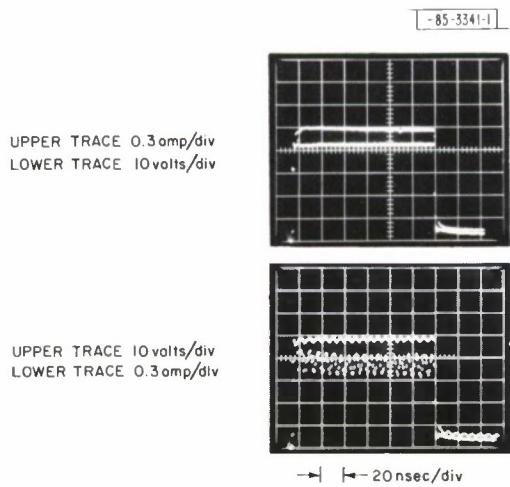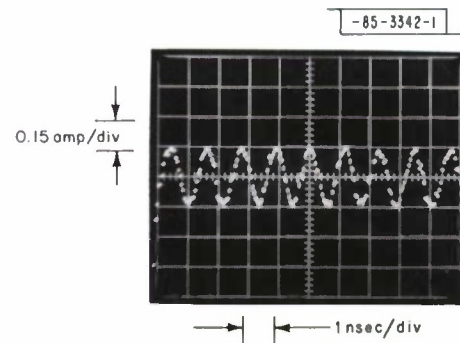electric field is increased. At some critical velocity, which is different for different temperatures, the current becomes unstable in time. Although the instability is relatively unchanged at 77°K, it is interesting to note that the threshold drift velocity is higher at the lower temperature, contrary to what might be expected for most plasma effects, in which there is competition between drift and thermal velocities. The relation $f = v_d/L$ is followed at both temperatures. The instability may be seen in Fig. I-10 which shows the voltage and current waveforms as a function of time. Below threshold, the current follows the voltage and shows nothing unusual. However, above the instability threshold the current varies in time and the average current drops noticeably. It is apparent that the effect is a large one with the peak-to-peak amplitude 20 percent of the average value of the current for this case. An expanded view of the current vs time shown in Fig. I-11 indicates the sinusoidal nature which the instability may have. For this case, the frequency is slightly less than 1 Gcps.

2. Magnetic Field Effects

Three features of the magnetic field dependence were noted. First, there was no effect on the threshold from either a longitudinal or a transverse magnetic field. Second, above threshold there was no effect on the frequency, but there was a large effect on the amplitude of the instability with a transverse field, with the amplitude reduced to less than five percent of its zero-field value at $B_o \sim 20$ kgauss. Third, with a longitudinal field there was only a relatively small effect on the instability amplitude above threshold. The last two features are shown in Fig. I-12. There is some question about whether the longitudinal field effect is actually present, because the instability amplitude was very sensitive to orientation of the magnetic field around the longitudinal direction, and it is possible that a longitudinal direction was never achieved. Also, the contacts might have been slightly nonuniform, making the current flow not purely longitudinal. More work will be needed to resolve this question.

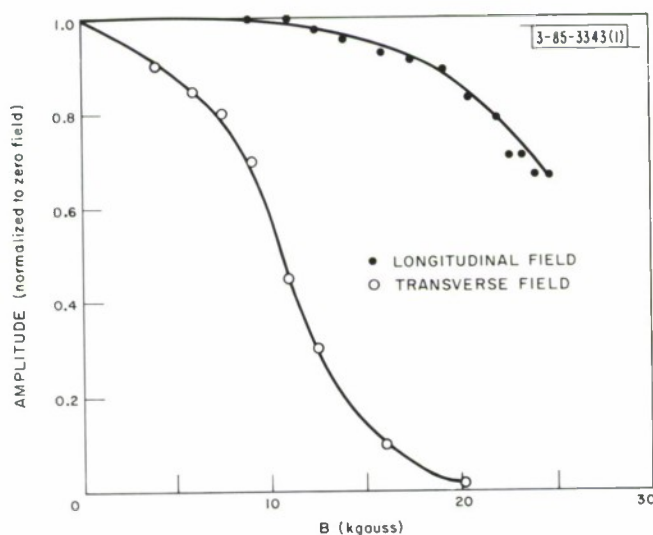Fig. I-12. Amplitude of instability vs magnetic field at 300°K.
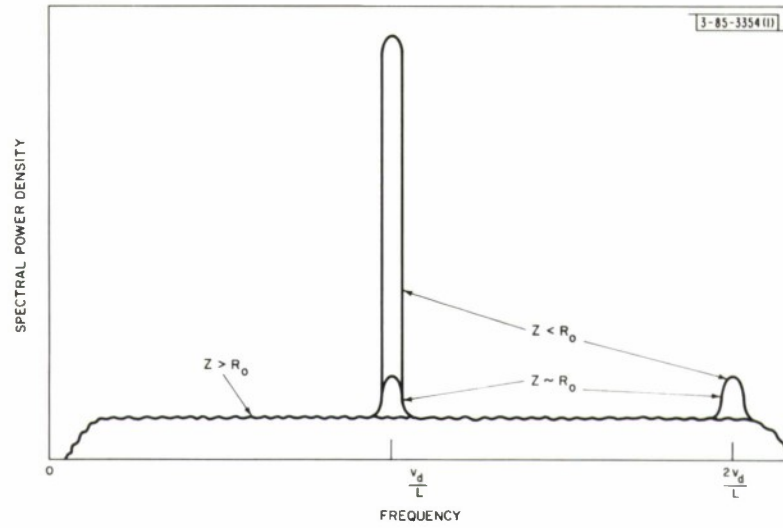
Fig. I-13. Spectral power density of instability vs frequency for three termination resistances.
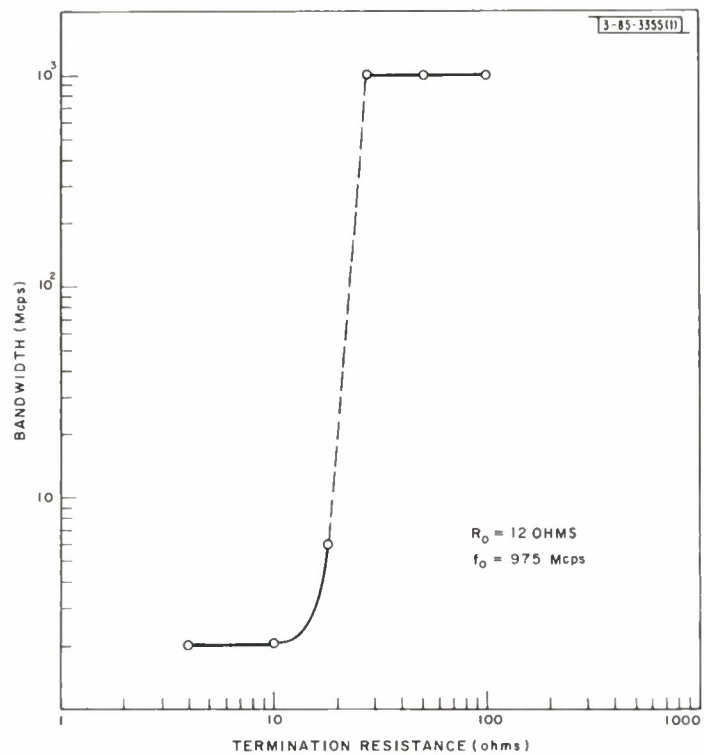
Fig. I-14. Bandwidth of instability vs termination resistance for a typical sample.

3. Impedance Effects

The effects of termination impedance on this instability are by far the strongest and most interesting that have been found. The instability does occur regardless of the termination impedance, and the threshold current (velocity) is relatively independent of termination. However, the spectrum of the instability is greatly affected by the termination, as shown in Fig. I-13. For high termination impedance the spectrum of the instability is very broad, with contributions from low frequency to about 2 Gcps, and the spectral power density is low. As the impedance is lowered, a narrow peak begins to appear in the spectrum at $f = v_d/L$ and also at $f = 2v_d/L$. As the impedance is lowered further, the peak at $f = v_d/L$ increases in amplitude, with a bandwidth that is apparently limited by pulse length, and the power in the broad-band noise decreases. Although the spectral transition occurred for the present samples at $Z \sim R_o$, there is no reason at this time to believe this is true generally. The peak at $f = 2v_d/L$ varies in an erratic fashion from sample to sample, usually being small, but occasionally becoming as large as the fundamental. This erratic behavior appears to be due to imperfect contacts.

Figure I-14 shows some features of the transition from high impedance to low impedance in a graph of bandwidth vs termination impedance. There are two important things to note: first, the very rapid change in bandwidth as the impedance is lowered through the sample resistance, as if some new mechanism is coming into play; second, the large difference between the bandwidth of the high impedance case (~ 1 Gcps or more) and the low impedance case (~ 2 Mcps, limited apparently by pulse length).

A. G. Foyt
A. L. McWhorter

REFERENCES

1. R.N. Hall, G.E. Fenner, J.D. Kingsley, T.F. Soltys, and R.O. Carlson, Phys. Rev. Letters 9, 366 (1962).

2. M.I. Nathan, W.P. Dumke, G. Burns, F.H. Dill, Jr., and G. Lasher, Appl. Phys. Letters 1, 62 (1962).

3. T.M. Quist, R.H. Rediker, R.J. Keyes, W.E. Krag, B. Lax, A.L. McWhorter, and H.J. Zeiger, Appl. Phys. Letters 1, 91 (1962).

4. I. Melngailis, Appl. Phys. Letters 2, 176 (1963).

5. K. Weiser and R.S. Levitt, Appl. Phys. Letters 2, 178 (1963).

6. R.J. Phelan, Jr., A.R. Calawa, R.H. Rediker, R.J. Keyes, and B. Lax, Appl. Phys. Letters 3, 143 (1963).

7. C. Benoit á la Guillaume and P. Lavallard, Solid State Commun. 1, 148 (1963).

8. N. Holonyak, Jr., and S.F. Bevaqua, Appl. Phys. Letters 1, 82 (1962).

9. I. Melngailis, A.J. Strauss, and R.H. Rediker, Proc. IEEE 51, 1154 (1963).

10. F.B. Alexander, V.R. Bird, D.R. Carpenter, G.W. Manley, P.S. McDermott, J.R. Peloke, H.F. Quinn, R.J. Riley, and L.R. Yetter, Appl. Phys. Letters 4, 13 (1964).

11. K.F. Cuff, M.R. Ellett, and C.D. Kuglin, Proceedings of the International Conference on the Physics of Semiconductors, Exeter (1962), p. 316.

12. Y. Sato, M. Fujimoto, and A. Kobayashi, Japanese J. of Appl. Phys. 2, 688 (1963).

13. J.F. Butler, J. Electrochem. Soc. (to be published).

14. E.R. Washwell and K.F. Cuff, Bull. Amer. Phys. Soc. 9, 293 (1964).

15. A.K. Walton and T.S. Moss, Proc. Phys. Soc. 81, 509 (1963).

16. R.H. Rediker, S. Stopek, and J.H.R. Ward, Solid State Electronics (to be published).

17. Solid State Research Report, Lincoln Laboratory, M.I.T. (1964:1), pp. 17-19, DDC 601830.

18. W. Shockley, U.S. Patent 2,569,347 (25 September 1951).

19. H. Kroemer, Proc. IRE 45, 1535 (1957).

20. R.L. Anderson, Solid State Electronics 5, 341 (1962).

21. J.B. Gunn, Solid State Commun. 1, 84 (1963).

II. LASER RESEARCH

A. RAMAN LASER PROGRAM

1. Stimulated Raman Emission at 90° to Ruby Beam

As mentioned in the last Solid State Research Report,[*] the proposal for a multiple-pumped Raman laser[1] is being investigated experimentally. Since one convenient configuration for such multiple pumping is one in which the Raman output is taken at right angles to a series of parallel, primary ruby lasers, the initial experiment was designed to investigate the feasibility of obtaining stimulated Raman emission at 90° to the ruby laser beam. Ninety degree stimulated Raman emission has been obtained, and some of the quantitative results of the gain and laser characteristics are described below.
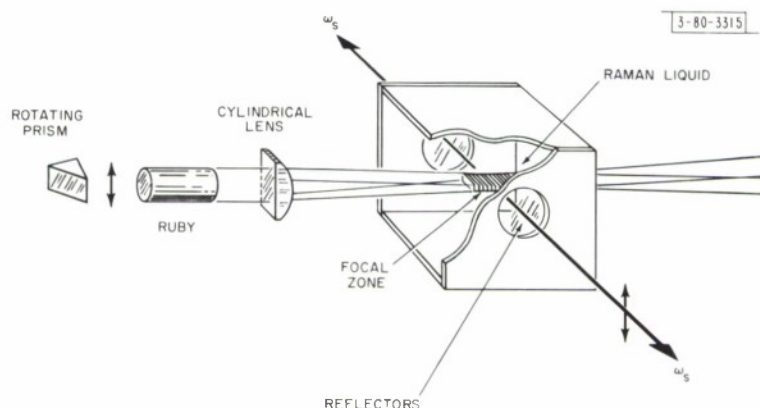
Fig. II-1. Experimental setup.

The experimental arrangement is shown in Fig. II-1. A 30-nsec Q-switched ruby pulse of a few megawatts is focused by a 10-cm cylindrical lens into a cavity structure which has two side walls consisting of optical flats spaced 2.12 cm apart. The dielectric-coated flats are 99-percent reflecting at the first Stokes wavelength of nitrobenzene, are parallel to each other, and are at 90° to the forward ruby beam.

When the ruby beam is fired into the cavity filled with nitrobenzene, stimulated Raman radiation is emitted at right angles to the forward direction. The evidence for this is:

    (a) The magnitude of the 90° Stokes radiation (at 0.765 micron), as detected by a photoelectric double monochromator, has a sharp threshold as a function of ruby-laser power, the threshold occuring at approximately 2 Mw. The pulse width is approximately 10 nsec.

    (b) The intense Stokes output is detected only when the two reflectors are parallel to within a few minutes of arc.

13

-SS-3385

(a)

(c)

(b)

(d)
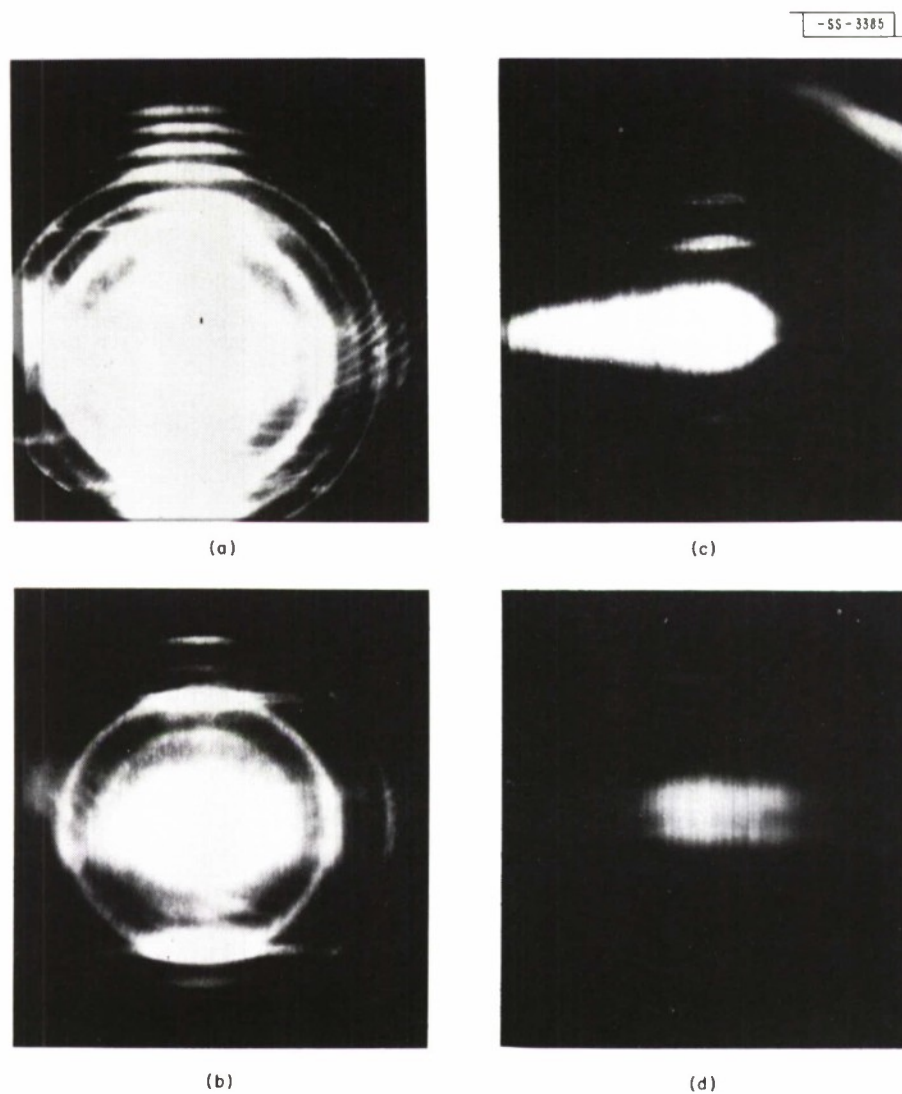
Fig. II-2. Far-field patterns af 90° Stakes radiatian taken with a 2-meter facal length lens. Decreasing exposures are shown in (a) through (d).

(c) Direct-image photographs (no lens, and filtered against ruby light) of the radiation emitted at 90°, which were taken on infrared film, both at a 40-cm distance and at 2 meters, show only a very small amount of beam spreading. The observed dimensions of the radiating region are 0.5 cm wide (the diameter of the ruby beam), 2 cm long (the aperture of the reflectors), and 0.1 cm high at the center of the cavity, broadening out to 0.25 cm at the limits of the 2-cm aperture. With a 5-Mw ruby pulse, the Raman cavity radiates over this entire region. Just above threshold (2 Mw), it radiates only in the center — the point of maximum concentration of the ruby pump.

(d) The intense Stokes output disappears when the cylindrical lens is rotated between 5° and 10° about a longitudinal axis. This agrees roughly with the finite height of the observed active region (0.1 cm) and the width of the ruby beam (approximately 0.5 cm). That is, a ray skewed at 0.1 cm/0.5 cm = 0.2 radian to the transverse axis of the cylindrical lens will still traverse the active region while remaining perpendicular to the side reflectors.

(e) The second Stokes radiation (S_2) at 0.853 micron is observed at 90° with an intensity of about one percent of the first Stokes radiation (S_1). Since the cavity reflectors also transmit less than one percent at S_2, this S_2 must be generated by 90°-directed S_1 radiation rather than by scattered forward S_2.

The peak Stokes power emitted in the forward direction and at 90° has been measured with a Korad K-D1 detector. At the maximum ruby power available (approximately 5 Mw) the measured Stokes output power at 90° was about 10 kw, the measurable external output being severely limited by the 0.3-percent transmitting reflectors. The corresponding forward Stokes power was measured as approximately 150 kw.

Some limits can be placed on gain estimated in the right-angle direction. At threshold, the gain must just equal the loss, so that for 99.1-percent reflectors (0.3-percent transmission loss, estimated 0.6-percent absorption loss) and no other losses, the gain would be

$$\alpha = (1 - R)/\ell = \frac{1 - 0.991}{0.5\,\text{cm}} \cong 0.02\,\text{cm}^{-1} \quad (\text{at } 2\,\text{Mw}/0.05\,\text{cm}^2) \quad .$$

(This is equivalent to $0.16\,\text{cm}^{-1}$ for a 300-Mw/cm^2 incident ruby beam density, an arbitrary beam density which is sometimes used as a convenient standard for comparison purposes.) On the other hand, allowing at most an additional 1-percent loss per round-trip path, $\alpha \cong 0.04\,\text{cm}^{-1}$. This loss is an upper limit because of the large number of walk-off modes observed, as mentioned below.

A number of models have been proposed for the mechanism of Stokes and anti-Stokes generation in a laser-pumped Raman-active medium. The theories differ in detail, among other things, with respect to the traveling-wave gain that can be obtained in an arbitrary direction to the ruby beam. For example, one model[2] predicts that Stokes radiation should emerge predominantly in the forward direction due to momentum transfer from the incident beam. Comparing our 90° gain estimate with previously estimated[3] forward gain in nitrobenzene of 0.1 to 1 cm^{-1} (at 300 Mw/cm^2), the Stokes gain at 90° is not drastically smaller than forward Stokes gain. The uncertainties arise in part from the filamentary structure of the ruby pump beam, which leads to a possible difference between geometric and effective Raman active path lengths. The 90° emission also permits determination of the Raman scattering cross-section dependence on polarization, although this has not been carried out yet.

Figure II-2(a-d) shows a series of far-field photographs of the 90° laser radiation taken with a 2-meter lens. The rings correspond to the Fabry-Perot modes of the cavity from scattered
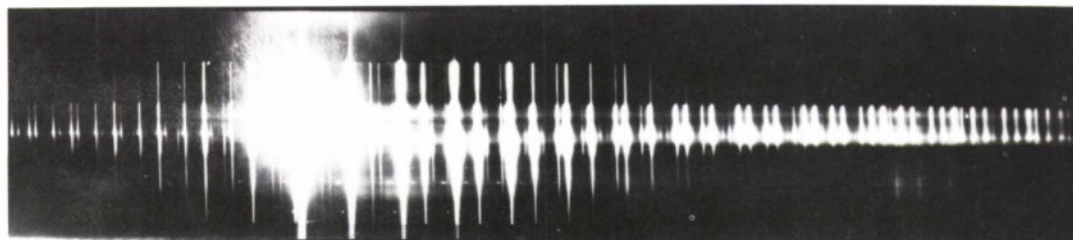
-SS-3386

Fig. II-3. Stimulated Roman scattering in bromoform.
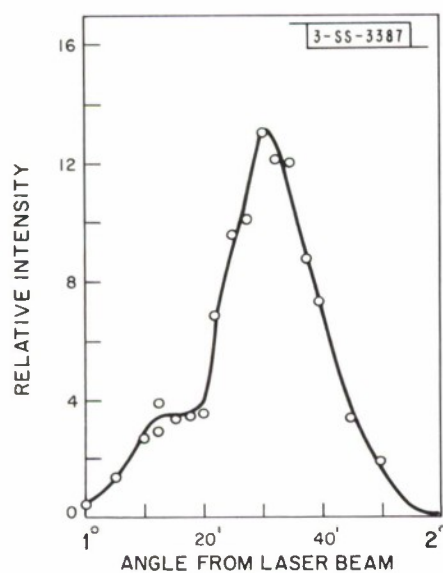

3-SS-3387

Fig. II-4. Angular emission of first "combination anti-Stokes line."

light of the central Stokes frequency. The width of the central maximum is determined primarily by the number of walk-off paths that stay within the active region long enough to get above threshold; these walk-off modes are oscillating in a continuum of frequencies centered about the frequency which is exactly resonant perpendicular to the plane of the reflectors. This continuum extends over about one-third the interorder separation. The beam divergence is estimated to be about 2 mrad. Actually, this particular far-field pattern is no indication of the ultimate beam quality attainable from 90° stimulated Raman emission because the many off-axis modes that contribute to beam spreading are simply characteristic of the small optical cavity used. A frequency-analyzing picture taken with an external etalon of 17-kMcps interorder spacing shows complete overlapping of orders, indicating that the Raman cavity, whose interorder spacing is 4.7 kMcps, is oscillating in more than four axial modes.

The fainter rings inside the major rings just barely visible in Fig. II-2(a) and the splittings in (b), (c), and (d) are compatible with a 5.9-kMcps shift and thus could be the result of stimulated Brillouin[4] scattered Stokes radiation in nitrobenzene. This remains to be proven. The present 90° cylindrical geometry allows both focusing and the use of resonant structure in an optimum optical configuration for plane-parallel reflectors. Theoretically, the same gain per pass would be obtained with spherical focusing, but the local heating spoils the optical homogeneity of the cavity.

The program will be continued with investigation, among other things, of the effects of stimulated Brillouin scattering on the quality of the 90° Raman beam.

Jane H. Dennis
P. E. Tannenwald

2. Stimulated Raman Scattering in Bromoform

In using bromoform as a test medium for the development of laser power, we have uncovered an extremely rich source of stimulated Raman emission. Figure II-3 shows the spectrum that results when a giant-pulsed ruby laser is focused into a cell of bromoform. This spectrum contains approximately 150 lines which can be accounted for by the excitation of two vibrational levels of the molecule with energy spacings of 222.3 and 538.6 cm^{-1}. The former is excited to at least the fourteenth Stokes and eleventh anti-Stokes line and the latter to the sixth Stokes and fourth anti-Stokes line. However, the profusion of frequencies is caused by combination or "second generation" frequencies resulting from multiple Raman scattering from vibrational species.

The angular variation of one of these second generation anti-Stokes Raman lines is shown in Fig. II-4. The predicted emission angles, calculated from phase matching conditions, for this frequency ($\omega_L + \omega_a + \omega_b$, where ω_L is the ruby laser frequency and ω_a and ω_b are the frequencies of the two vibrational levels) are 1.496° and 1.516°, depending upon whether the first step of the multiple scattering produces the ω_a shift or the ω_b shift. The agreement with the experimentally measured 1.50° is very good.

S. Kern
B. Feldman

B. OPTICAL MASER PROPERTIES OF CeF$_3$. ENERGY TRANSFER AND STIMULATED EMISSION FROM CeF$_3$:Nd^{+3}

Divalent rare-earth ions have strong visible f → d optical transitions.[5] These ions are easily pumped as optical masers. Trivalent rare-earth ions are characterized by weak f → f transitions
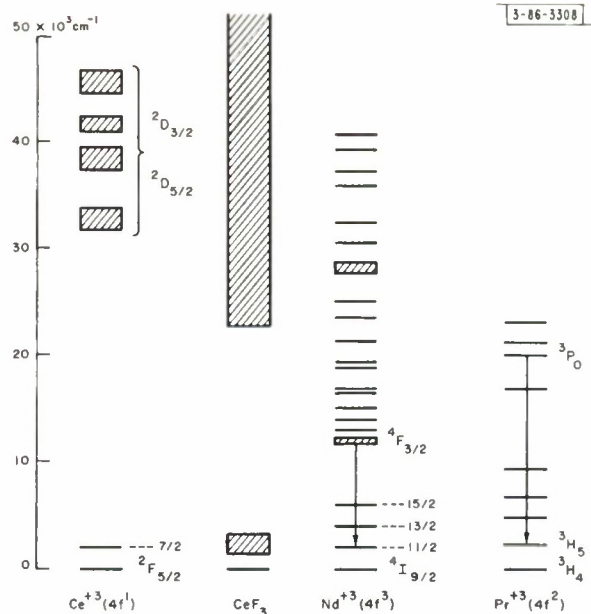
Fig. II-5. Atomic energy levels of Ce^{+3}, Nd^{+3}, and Pr^{+3}. Lattice obsorptian bands of CeF$_3$.

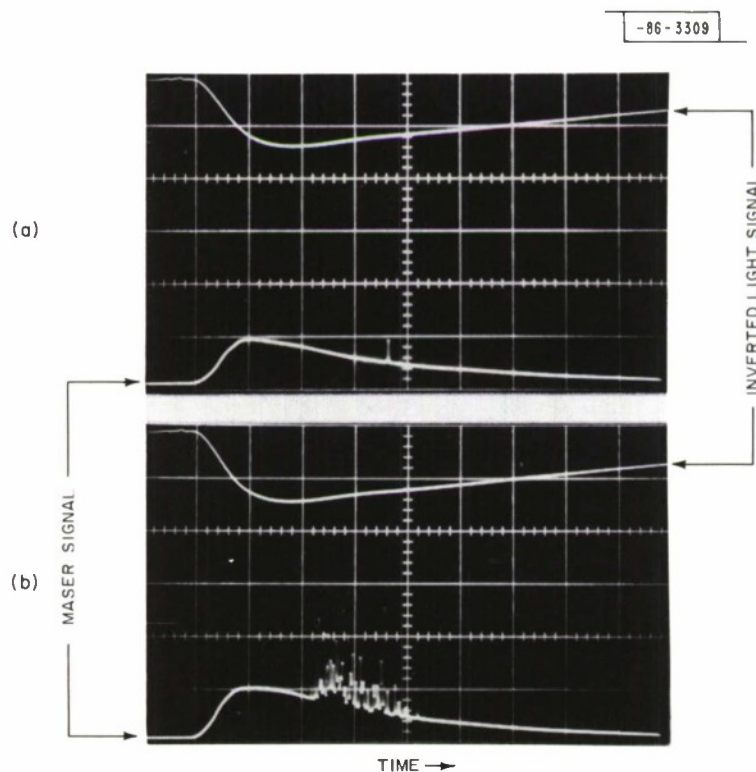Fig. II-6. Maser ond flashlamp intensity signols os o function of time (50 μsec per divisian). (o) CeF$_3$:Nd^{+3} moser ot threshold (~41 joules). (b) Moser output obove threshold.

18

and are not easily pumped. One way of circumventing this problem is to develop an active maser host, whereby energy can be transferred from the lattice to the rare-earth ions. Some of the maser properties of grown single crystals* of CeF_3 and in particular the transfer of lattice energy in order to stimulate emission from $CeF_3:Nd^{+3}$ are described.

The ground state of Ce^{+3} contains one 4f electron shielded by $5s^2 5p^6$ shells. The energy levels of Ce^{+3} are shown in Fig. II-5. One f → f transition occurs at 2000 cm^{-1} and f → d transitions start at ~31,000 cm^{-1}. Energy levels of CeF_3 show that ion-ion coupling causes the $^2F_{7/2}$ level to become an absorption band (1500 to 3800 cm^{-1}) and lowers the initial f → d transition to ~22,000 cm^{-1}. CeF_3 is an interesting maser host because of: (1) direct energy transfer from the lattice to the rare-earth ion; (2) radiative energy transfer to the rare-earth ion due to the intense d → f fluorescence (Ref. 6) of Ce^{+3} from 3000 to 4500 Å; (3) rapid depopulation of any terminal state (e.g., Nd^{+3}, Pr^{+3}) within the $^2F_{7/2}$ lattice absorption. Conversely, this absorption can be used to efficiently populate a terminal state so as to modulate the maser output.

The energy levels of $CeF_3:Nd^{+3}$ are shown in Fig. II-5. The excited ion fluoresces due to radiative transitions from the $^4F_{3/2}$ level to one of the levels of the ^4I multiplet. Absorption and fluorescent measurements were made at 77°K to determine the position of these levels. The results can be summarized as follows:

(1) Resonance transitions to the $^4F_{3/2}$ levels are observed at 11,620 cm^{-1}.

(2) Levels of the ^4I multiplet lie at 2222 cm^{-1}(11/2), 3876 cm^{-1}(13/2), and 5910 cm^{-1}(15/2).

(3) Strong emissions are observed at 1.06 microns with a halfwidth of 9 cm^{-1} and a lifetime of 225 μsec at 77°K.

Excitation experiments were performed on crystals (4 cm × 0.5 cm), containing 0.1 atomic percent neodymium, fabricated into cylindrical etalons. The end faces were flat (~λ/4), parallel (approximately 6 seconds) and silvered. The crystals were held in a cooled chuck. Emission was monitored by a photomultiplier tube through an interference filter. Figure II-6(a) shows the maser at threshold when the etalon is illuminated with approximately 41 joules of pump light. Figure II-6(b) shows the maser output 10 percent above threshold. The maser output was focused into a grating spectrometer. Stimulated emission occurs at 1.0638 microns and is π polarized.[†]

Interactions between the CeF_3 lattice and Nd^{+3} ions were observed. In one experiment, filters were used to remove flashlamp radiation at wavelengths < 5000 Å. This procedure increases the threshold of a 0.5-joule $CaWO_4:Nd^{+3}$ maser by approximately 20 percent. For $CeF_3:Nd^{+3}$, however, stimulated emission was not observed even though threshold conditions were exceeded by a factor of four which implies that a large amount of lattice energy excites Nd^{+3} ions. In another experiment a 2-mm-diameter maser was positioned so that it could be illuminated with filtered, 3- to 6-micron radiation from a 3000-watt tungsten ribbon filament. At a given pump level, the time required for stimulated emission to occur was measured with and without the tungsten illumination. Using simple maser rate equations,[7] an increase in threshold of approximately 7 percent is computed when the maser is irradiated with infrared

---

photons.   This shows that the CeF_3 lattice, which strongly absorbs 3- to 6-micron radiation, populates the $^4I_{11/2}$ level of Nd^{+3}.   This population decreases the negative temperature of the Nd^{+3} system and leads to a higher threshold.

<div align="right">J. R. O'Connor</div>

C. GASEOUS BREAKDOWN BY A GIANT-PULSED RUBY LASER

A number of experiments to determine the mechanism for laser-created gaseous breakdown have been initiated.   These include studies of the emission spectra, temporal properties of the spark, magnetic field effects and pressure effects.   So far, most of the work has been limited to air and argon, with some preliminary work in nitrogen.

1. Air

Spectrum:— The spectrum of the spark created in air has been examined in an attempt to identify some of the excited species.   The spectra are in general complex, and identification so far is incomplete, but they consist of many lines superimposed on a "gray or black-body" background.   The maximum temperature of this "black body" is about 6900 to 7200°K as estimated from the Wien displacement formula.   This is to be compared for example with the surface temperature of the sun which is about 5800°K or the color temperature of an exploding wire which is about 20,000°K.

Temporal Properties:— The temporal properties of the air spark were examined with the aid of a Space Technology Laboratory image converter camera.   Only the afterglow region of the spark could be examined with this instrument, as it was used.   When some camera triggering modifications have been made, it will be possible to examine the spark through its entire lifetime.   Figure II-7 shows three photographs of the air spark 150, 250, and 350 nsec (top to bottom) after the ruby pulse.   The photographs were taken three times for each of the three different sparks.   The exposure time for each frame is 20 nsec.   The laser pulse is propagating in the direction indicated.   In the top frame, which is about 150 nsec after the ruby pulse, the spark consists of a cylindrical plasma about 4 mm long and 1/2 mm in diameter surrounded by a shockwave.   The cylindrical luminous zone grows laterally and longitudinally.

A streak photograph of the air spark is shown in Fig. II-8.   This photograph starts about 60 nsec after the ruby pulse and lasts for 1 μsec.   The air spark grows at a rate of about 5 × 10^5 cm/sec in the directions parallel and antiparallel to the ruby pulse propagation direction.

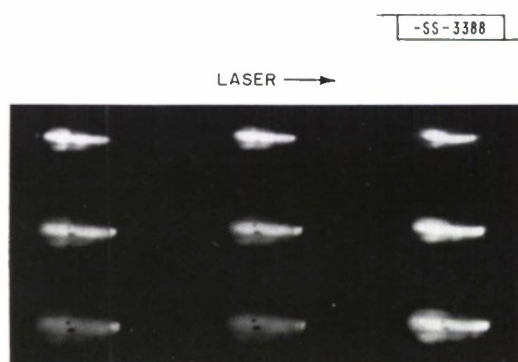<div align="center">| -SS-3388 |</div>

LASER ⟶

Fig. II-7. Framing photograph of laser-created spark in air. Frames are 150, 250, and 350 nsec (top to bottom) after the ruby laser pulse. Photographs were taken three times for three different sparks.

Fig. II-8. Streak photograph of laser-created spark in air. Photograph starts about 60 nsec after start of spark with a 1-µsec streak time. Time runs from top to bottom.
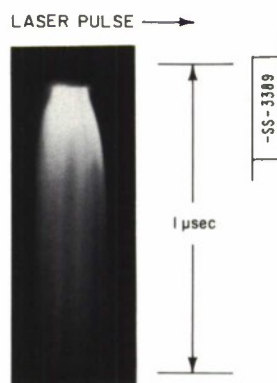
Structure suggestive of a converging recompression shockwave can also be seen in the photograph. Assuming that the spark is created in the focal volume, about $10^{-5}\,cm^3$, the total enthalpy within the spark would be about 10^{-3} joule which is one-tenth of one percent of the ruby pulse energy (60-Mw peak power with a halfwidth of about 20 nsec). This would be only a moderate conversion of ruby energy into the spark.

A careful measurement was made of the rise and decay times of the air spark as well as of the delay of the spark relative to the ruby pulse. These data will be compared with similar data obtained for monatomic and diatomic gases to assist in studying the breakdown mechanism. The ruby pulse rise times* are typically 9 nsec, whereas the spark rise times vary from 10 to 15 nsec. The delay between the start of the spark and the start of the ruby pulse is from 5 to 12 nsec. The decay times of the air spark are typically 80 nsec.

Magnetic Field Effects:— The effects of a magnetic field on the breakdown threshold were examined to gain insight into the dominant loss mechanism in the spark. Lax, et al.,[8] have given an expression for the effect of a DC magnetic field in the breakdown electric field. Applying this expression to the optical frequency case with magnetic field of the order of 100 kgauss, the ratio of the breakdown electric field with a DC magnetic field to that without a DC magnetic field is

$$\frac{E_m}{E} = [1 + \omega_c^2 \tau^2]^{-1/2} \quad .$$

Here $\omega_c = eH/mc$ is the cyclotron frequency. For optical frequencies, $\omega \gg \omega_c$. The scattering time τ depends inversely on the pressure. For pressures less than about 0.1 atmosphere, the ratio E_m/E is less than unity and decreases with decreasing pressure. Gould and Roberts[9] have developed a theory of breakdown at microwave frequencies in which they consider the cases of CW and single-pulse breakdown. Applying the single-pulse expressions to the laser-created breakdown, it is found that for the laser pulsewidths available (20 nsec) the effect of diffusion in removing electrons from the spark is negligible. Therefore, magnetic field effects should be negligible since they enter through the diffusion properties of the free electrons.[8] Air breakdown experiments in magnetic fields up to 93 kgauss† confirm this conclusion.

---

* The rise and decay times are taken at the 1/e points.

† These high magnetic field experiments were conducted at National Magnet Laboratory, M.I.T.

21

2. Argon

Spectrum:— The spectrum of the laser-created argon spark has been analyzed in order to determine the various breakdown species produced. Special care was taken to eliminate the xenon flashlamp radiation from entering the spectrometer. At atmospheric pressure, many spectral lines corresponding to published argon spectra are observed. The identification of the complex argon spark is incomplete at the present time.

Temporal Properties:— The rise, decay, and delay times relative to the ruby pulse are being examined. Preliminary studies indicate that the delay between the argon pulse and ruby pulse is less than 1 nsec for pressures between an atmosphere and 1000 psi. This is in contrast to the 5- to 12-nsec delay for the air spark.

Pressure Effects:— The intensity of the spark spectrum decreases as the gas pressure is increased. For pressures greater than about 400 psi, the line spectra have negligible intensity. The breakdown threshold in argon has been measured as a function of pressure between atmospheric pressure and 2000 psi. The curve has the same general slope as that given by Meyerand and Haught[10] and by Minck.[11] The peak powers for breakdown agree approximately with those given in Ref. 10 but are about ten times greater than those given by Minck, possibly because of the relative mode purities of the laser pulses and different focal length lenses used. The experimentally reproducible step-wise variations of the curve cannot be accounted for and are being investigated.

D. F. Edwards

D. PULSED LASER DOSIMETER

An optical safety monitor has been developed to measure the level of laser energy reflected from a target surface in order to warn of danger to the observer's eye. When the dosimeter is held to the eye and is pointed at the illuminated surface, the dosimeter needle will deflect by an amount (measured in roentgens) proportional to the laser light which enters the dosimeter. The instrument consists of a gamma-radiation detector, used as an electrometer, which is connected in parallel with an RCA 925 phototube. Figure II-9 illustrates both the electrical and optical components of this system.
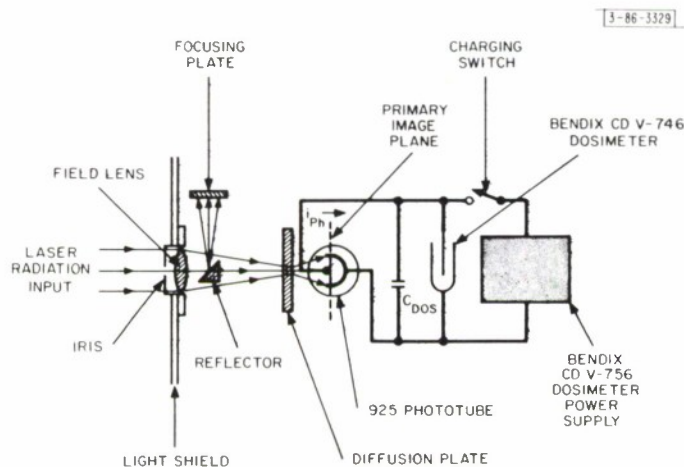

Fig. II-9. Schematic diagram of pulsed laser dosimeter.

The full-scale sensitivity of the instrument is based on a critical retinal energy density of 0.7 joule/cm for an 800- to 1200-micron retinal spot and a pulse length of 175 μsec. This criterion was established by Ham and Geeraets of the Medical College of Virginia in ruby laser experiments on rabbits' eyes. A one-tenth scale deflection on the dosimeter is taken to be the danger level to assure a safety factor of at least ten.

The experimental linear response of the dosimeter to a spiking ruby laser can be summarized as

$$\delta R \simeq k \, \frac{\tau i(\tau)}{C_{dos}} \quad ,$$

where k = 8.8 roentgens/volt, δR is the scale deflection in roentgens, τ is the total length of the laser pulse train, and $i(\tau)$ is the peak value of the photocurrent. The photocurrent, at which the system's response becomes nonlinear for an individual laser pulse of approximately 1/2 μsec, is 4 ma. With δR = 600 roentgens, $i(\tau) < 4$ ma, and $\tau \simeq 200$ μsec, C_{dos} must be < 12,000 pfd. Since the present dosimeter has a capacitance of approximately 1000 pfd, the shortest laser train allowed for full-scale linearity is approximately 20 μsec.

The energy density $J(\lambda)$ (in joules/cm^2) at the field lens required for a full-scale deflection may be written

$$J(\lambda) = \frac{\delta R C_{dos}}{k S(\lambda) \, \sigma F(\lambda)} \quad ,$$

where $S(\lambda)$ is the photosurface sensitivity (in amperes/watt), σ is the optical system's aperture (in square centimeters), $F(\lambda)$ is the optical system's attenuation factor, and δR, C_{dos}, and k are as previously defined. Therefore, the maximum sensitivity for the dosimeter when the aperture is fully open to 14 cm^2, for ruby radiation and $F(\lambda)$ equal to unity, is approximately 2×10^{-6} joule/cm^2. The iris shown in Fig. II-9 permits a five-order-of-magnitude increase in this value for both ruby and neodymium laser radiation.

The dosimeter is presently designed for spiking ruby lasers with total pulse length about 175 μsec. Clinical data obtained with Q-spoiled lasers indicate that retinal damage also depends upon the peak laser power and not just the energy density. Therefore, redesign of the dosimeter for very short pulse lasers is being considered.

A more detailed report concerning the operation of the dosimeter has been accepted for publication in Electronics.

J. J. Schlickman
R. H. Kingston

E. GAS LASER PROGRAM

1. Detection of Light Intensity Fluctuations by Means of Photoelectron Counting

Measurements of the amplitude modulation noise of optical maser light have been in progress for some time. Results of spectrum analyses of photodetector currents produced by illumination of the photocathode with a variety of He-Ne oscillators at 6328 Å have been reported.[12] The theoretical and experimental results on the statistics of the photoelectron counts of photomultipliers illuminated by optical maser light at 6328 Å, both above and below the threshold of oscillation, are discussed here.

Suppose light with a time-dependent power P(t) is incident upon the photocathode of a photomultiplier. Each of the emitted photoelectrons produces a current pulse in the anode circuit of

the photomultiplier. The probability that a photoelectron is emitted in the time interval t, t + dt, is given by p(t) dt as

$$p(t) \ dt = \frac{\eta}{h\nu} \ P(t) \ dt \quad , \tag{1}$$

where

η = quantum efficiency of the detector,

h = Planck's constant,

ν = frequency,

P(t) = time dependent power of incident light.

If it is assumed that the emission of photoelectrons within each differential time interval is independent of the emission of photoelectrons within preceding or following time intervals, then Eq. (1) leads to a time-varying Poisson distribution for the observed photoelectrons. Dark current is disregarded because it was negligible in all these experiments.

The average number of photoelectrons counted within a time interval T is then obtained from the time varying Poisson distribution and is given as

$$\bar{n}_T = \frac{\eta}{h\nu} \ \bar{P}T \quad . \tag{2}$$

The bar over n and P indicates an average over the ensemble of samples taken. Typically several hundred to several thousand samples are taken for each counting interval T_i. In the experiments under discussion we take a large number of counts n_{T_i} in each fixed interval T_i and observe the fluctuations in n_{T_i} over a sequence of such intervals. It can be shown[13] that the mean-square fluctuations in n_T are related to the autocorrelation function of the light power P(t) as follows:

$$\overline{n_T^2} - \bar{n}_T^2 = \overline{n_T}(1 + \frac{\eta}{h\nu} \ \bar{P}\tau_0) \quad , \tag{3}$$

where

$$\tau_0 = \int_{-\infty}^{\infty} |\rho|^2 \ d\tau \quad ,$$

and

$$\overline{P(t) \ P(t + \tau)} = \overline{P^2}(1 + |\rho|^2) \quad .$$

Consider the behavior of the mean-square fluctuations as a function of observation time T for:

(a) Narrow-band Gaussian light,

(b) Weakly modulated coherent maser oscillator light.

For narrow-band Gaussian light with a Lorentzian line-shape, a correlation time $\tau_0 = (1/\pi\Delta\nu)$ is determined by the spectral bandwidth $\Delta\nu$ of the light. For this case, the mean-square fluctuations in the photoelectron counts n_T, which are normalized with respect to the average count $\overline{n_T}$, become

$$\frac{\overline{n_T^2} - \overline{n}_T^2}{\overline{n_T}} = 1 + r\tau_o \left[1 - \frac{\tau_o}{2T} \left(1 - e^{-2T/\tau_o} \right) \right] \quad , \tag{4}$$

where $r = (\overline{n_T})/T$ is given counting rate for each plot of $(\overline{n_T^2} - \overline{n}_T^2)/n_T$ as a function of T.

For observation (counting) times T very much less or very much larger than the correlation time τ_o, Eq. (4) may be simplified to

$$\frac{\overline{n_T^2} - \overline{n}_T^2}{\overline{n_T}} = \begin{cases} 1 + rT & \text{for } T \ll \tau_o \\[2mm] 1 + r\tau_o & \text{for } T \gg \tau_o \end{cases} \quad . \tag{5}$$

For a weakly modulated optical maser oscillating in a single mode (as in our experiments), the time dependence of the electric field amplitude of the light and the definition of the modulation coefficient are the same as in low-frequency circuitry. Thus, we may write for the electric field amplitude

$$A = [A_o + a(t)] \cos[\omega(t) + \Theta(t)] \tag{6}$$

for the modulation coefficient

$$m^2 = \frac{\overline{a(t)^2}}{A_o^2} \quad ,$$

for the correlation function

$$\rho_a(\tau) = \frac{\overline{a(t) \, a(t + \tau)}}{\overline{a(t)^2}} \tag{7}$$

and for the mean-square fluctuations (normalized to $\overline{n}_T$)

$$\frac{\overline{n_T^2} - \overline{n}_T^2}{\overline{n_T}} = 1 + \frac{8m^2 \overline{n}_T}{T^2} \int_o^T (T - \tau) \, \rho_a(\tau) \, d\tau \quad , \tag{8}$$

where $m^2 \ll 1$ (which is always true for the experiments being discussed).

If we now assume that the amplitude modulation $a(t)$ is noise with a Lorentzian line-shape, then the corresponding equations become

$$\rho_a(\tau) = e^{-|\tau|/\tau_o} \tag{9}$$

and

$$\frac{\overline{n_T^2} - \overline{n}_T^2}{\overline{n_T}} = 1 + 8m^2 r\tau_o \left[1 - \frac{\tau_o}{T} \left(1 - e^{-T/\tau_o} \right) \right] \quad , \tag{10}$$

which may again be simplified to

25

Fig. II-10. Theoretical variation of normalized mean-square fluctuations in photoelectron counts as a function of observation time for the following cases:

Curve A: Narrow-band Gaussian light corresponding to a single TEM_{ooq} noise mode of the maser below threshold of oscillation.

Curve B: Weakly modulated maser light corresponding to a single TEM_{ooq} mode above threshold of oscillation.

Curve C: Unmodulated "ideal" maser light.

$$\frac{\overline{n_T^2} - \overline{n}_T^2}{\overline{n}_T} = \begin{cases} 1 + 4m^2 rT & ; \quad T \ll \tau_o \\ 1 + 8m^2 r\tau_o & ; \quad T \gg \tau_o \end{cases} \tag{11}$$

The bandwidth of the noise expected for a maser oscillating in a single mode will be generally narrower than the bandwidth of the optical cavity. This narrowing is due to the negative resistance of the maser material. Therefore, the noise bandwidth is generally a function of the excitation level of the maser.

Now, comparison can be made between the mean-square fluctuations expected for a maser oscillating in a single mode and those of a narrow-band Gaussian light, such as a single noise mode of an optical maser below the threshold of oscillation. Figure II-10 shows these curves based on Eqs. (5) and (11) computed for an assumed (Lorentzian) bandwidth of $\Delta\nu$ = 32 cps, a modulation index $m^2 = 10^{-4}$ and a photoelectron counting rate of r = 10^6/sec. From Fig. II-10 it is strikingly apparent that for identical bandwidths and photoelectron counting rates the mean-square fluctuations in photoelectron counts of Gaussian light will always rise above unity (which corresponds to shot noise) much sooner and will in general saturate at a much higher level than the corresponding fluctuations of an optical maser oscillator.

Figure II-11 shows two typical experimental curves, obtained with an internal mirror and a quiet and stable optical maser at 6328 Å (above and below the threshold of oscillation), respectively.

Since the indicated photoelectron counting rate of 12.7×10^6 is relatively high considering the finite resolving time (22 nsec) of the counter, a smoothing effect will occur because photoelectrons released within the resolving time are only counted as one. It can be shown that the resulting Poisson limit will reduce to exp $[-\overline{n}]$ instead of 1 ($\overline{n}$ denotes the average count per resolution time). Therefore, if r = 12.7×10^6/sec and the resolving time is approximately 22 nsec, then $\overline{n} \simeq 0.28$ and exp $[-\overline{n}] \simeq 0.7$. With this correction the experimental points fit extremely well to the theoretical shape expected and we may compute a modulation coefficient of $m^2 \simeq 1.2 \times 10^{-5}$ and a noise modulation bandwidth of 48 cps. When above the threshold of oscillation, the maser was carefully adjusted to provide a single longitudinal [TEM_{ooq}] mode output. The power output of the oscillating mode was so far above the combined output of the nonoscillating noise modes, that their contribution was negligible.

On the other hand, when below the threshold of oscillation, all longitudinal noise modes will contribute in varying degrees to the light power incident upon the photomultiplier. Spatial filtering can effectively remove the radial modes only. Thus, it was found that the experimental points shown on Fig. II-11 could not fit to a single noise mode. However, by assuming there were several contributing longitudinal modes, the experimental points fitted very well again. Since the below-threshold counting rate r = 1.16×10^6 was about eleven times less than in the previous case, no appreciable smoothing of the Poisson value resulted on account of resolving time limitation. No attenuators were inserted between the maser and detector for below-threshold measurements, whereas approximately 30-db attenuation was necessary for the oscillating condition of Fig. II-11.

The experimental setup is shown in the block diagram of Fig. II-12. The DC-excited laser emits light at both ends. On the left-hand side the light is used in part to stabilize the power output against long-term drifts. The light is detected in a photomultiplier and the output of the photomultiplier is compared with a standard voltage. Any deviation of the photomultiplier output
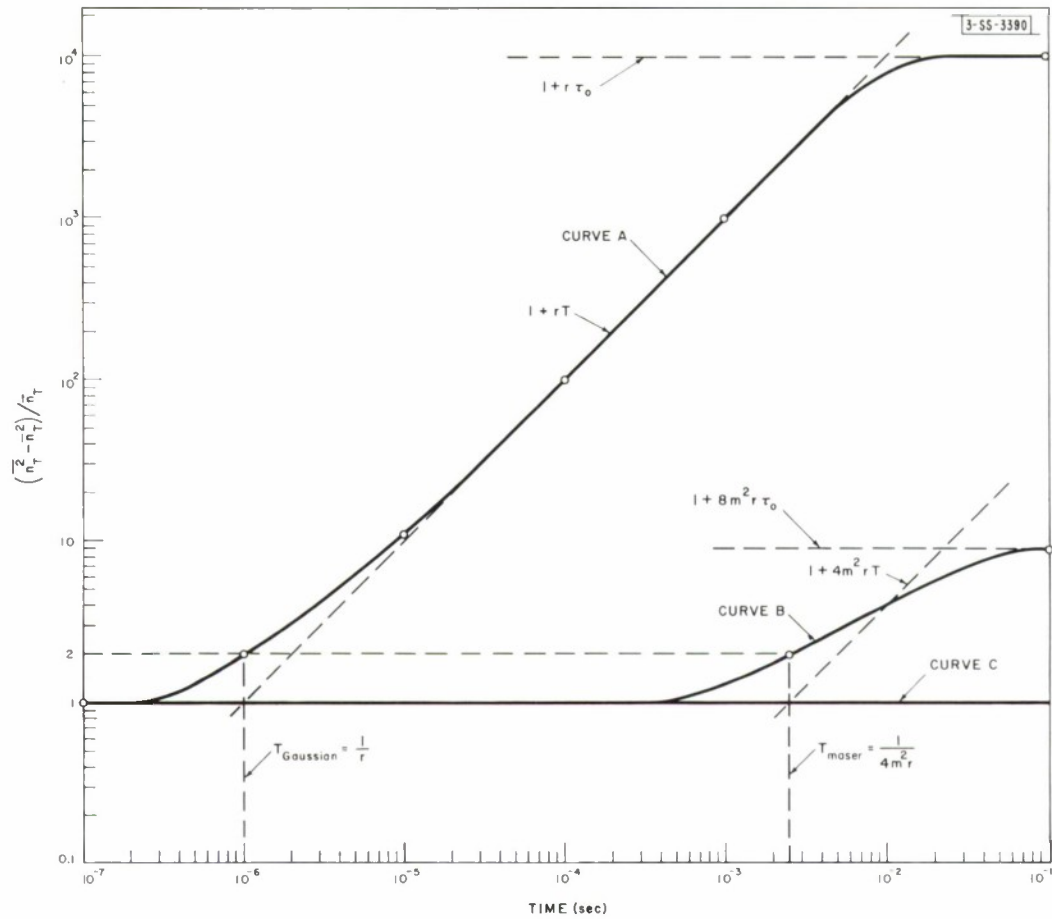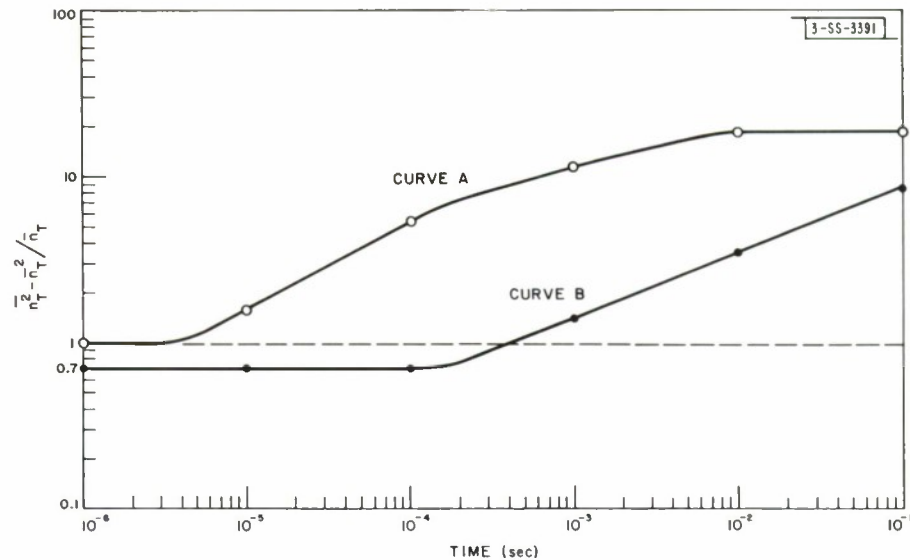
Fig. II-11. Experimental variation of normalized mean-square fluctuations in photoelectron counts as a function of observation time for the two cases:

Curve A: Maser below threshold of oscillation. Fluctuations are caused by the set of TEM_{ooq} noise modes which cannot be spatially filtered. The mode separation $\Delta f = 190$ Mcps and the photoelectron counting rate $r = 1.17 \times 10^6$/sec.

Curve B: Maser above threshold of oscillation. Fluctuations are caused by a single TEM_{ooq} mode. No other oscillating modes are present. The photoelectron counting rate $r = 1.27 \times 10^7$/sec.
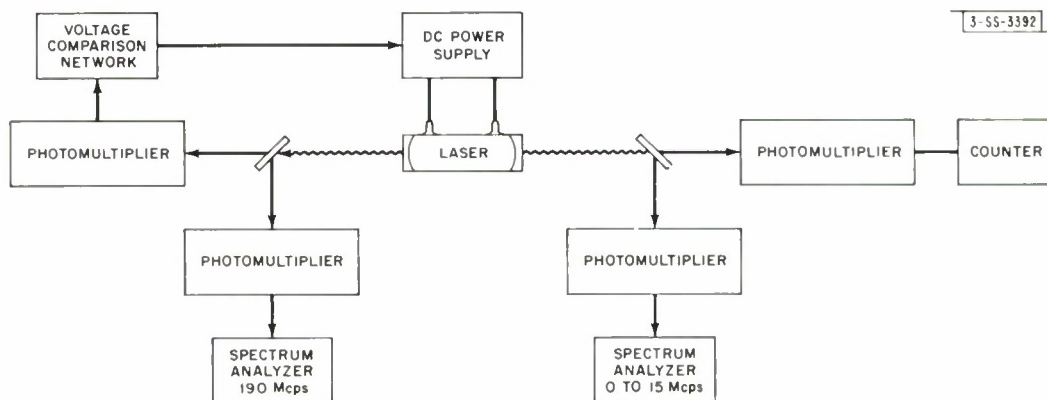
Fig. II-12. Simplified block diagram of experimental setup used in single channel photoelectron counting experiments.

28

from the desired voltage value is fed back as a correction signal into the DC power supply. Another portion of the light is detected in another photomultiplier whose output is displayed on a spectrum analyzer centered around 190 Mcps. This analyzer is used to detect the presence of higher order axial modes. The experiment is run so that it is well below the threshold of oscillation of multiple axial and radial modes. The light emerging on the right-hand side of the laser is fed partly to the photomultiplier and counter and partly to another photomultiplier and a spectrum analyzer capable of displaying the spectrum from 0 to 15 Mcps. This spectrum analyzer was used to see whether the laser was in quiet operation. Quite often, if no precautions were taken, plasma oscillations were clearly visible on the spectrum analyzer. They could be removed by the introduction of a local magnetic field near the discharge.

C. Freed
H. Haus[*]

2. Triode Gas Laser

Several experiments are in progress using a specially built gas laser tube, inside of which is a plane-parallel triode structure comprised of a grid and anode spaced 0.5 and 4.5 mm from a 19×0.6 cm heated cathode. The electron beam formed in the grid-anode region selectively excites the atomic states of a gas according to the electrode voltages. Investigations are under way to determine whether the triode current, being approximately monoenergetic, produces population inversion more efficiently than a discharge current.

Laser oscillation at 2.02 microns in pure xenon has been achieved with the triode at pressures ranging from 1 to 100 microns Hg. A gain of approximately 50 percent per meter was measured in this transition when the grid was pulsed 30 volts positive with respect to the cathode (resulting in a grid current of 4 amp). Because oscillation has been sustained at low atom densities, high-gain laser action might be obtained by injecting an atomic beam at right angles to both the electron beam and the axis of the optical resonator.

R. A. Soref
R. J. Carbone

3. High-Pressure Mercury Laser

The results of experiments to obtain pulsed laser oscillation at approximately 5000 Å in a high-pressure mercury vapor discharge tube look promising. The radiating system is the lowest excited state of the mercury molecule $^3 0_u$, with a radiative lifetime of about 2 msec. This state fluoresces in a blue-green band about 1300 Å wide. The width is due to the unstable lower state which is emptied by atomic dissociation in less than 10^{-13} sec. It is the combination of a metastable upper state and an extremely short-lived lower state that recommends this system, or similar ones, for high-power, high-pressure lasers. The possibility of laser action in hydrogen and mercury was first pointed out by Houtermans in 1960 (Ref. 14). The mercury system is particularly interesting because its emission is in the visible instead of the ultraviolet as in hydrogen. Furthermore, the large population in the resonance level $^3 P_1$ which is built up by electron impact and by resonance-radiation trapping can be efficiently diverted to the metastable

---

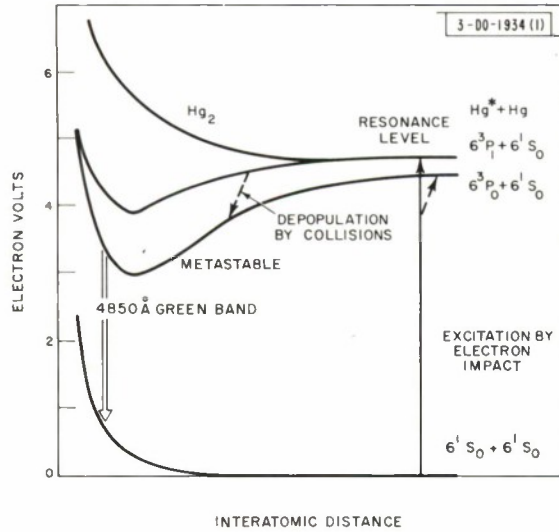[*] Department of Electrical Engineering, M.I.T.

Fig. II-13. Mercury potential curves.

states $^3P_0$ and ^3O_u by the frequent heavy particle collisions at high pressures. The kinetic proc-esses and the molecular states of mercury are indicated in Fig. II-13.

To achieve a laser gain of 1 percent per meter, the inverted population must be sufficient to produce about 50 watts/cm^3 of spontaneous emission. Under these conditions, laser action should take place in many cavity modes, with a total power in the kilowatt range.

Preliminary experiments, under conditions which optimized the peak power of the spontaneous emission, have shown nearly 5-percent conversion of the mercury atoms to upper state molecules, as estimated from the observed 10 watts/cm^3 of band fluorescence. Enhancement of the emission by additions of rare gases is being considered so that sufficient gain will be obtained for oscillation.

Power saturation is estimated from the usual condition that

$$T_1 T_2 (\frac{\mu}{\hbar})^2 \overline{E^2} \simeq 1 \quad ,$$

where μ is the electric dipole moment for the transition, $\overline{E^2}$ is the mean-square electric field, T_1 is the relaxation time for approaching population equilibrium between upper and lower states, and T_2 is the phase-correlation time, which in this case is the time for dissociation of the lower state. When $\mu \simeq 10^{-20}$ esu, $T_1 \simeq 10^{-7}$ sec, and $T_2 \simeq 10^{-13}$ sec, the rms standing-wave power (totalled over all the modes) for saturation occurs at 10^8 watts/cm^2 inside the cavity or at about 1-Mw output power. This requires a pump rate of about 10^{23} upper-state molecules per cubic centimeter per second, which is not unreasonably large at nearly atmospheric pressure with pulsed currents of hundreds of amperes.

M. M. Litvak
R. J. Carbone

REFERENCES

1. W. H. Culver and E. J. Seppi, private communication.

2. N. Bloembergen, Bull. Am. Phys. Soc. 9, 77 (1964).

3. R. W. Hellwarth, private communication; R. W. Terhune, private communication.

4. R. Y. Chiao, C. H. Townes, and B. P. Stoicheff, Phys. Rev. Letters 12, 592 (1964).

5. D. S. McClure and Z. Kiss, J. Chem. Phys. 39, 3251 (1963).

6. P. O. Feofilov, Optics and Spectroscopy 6, 150 (1959).

7. H. A. Bostick and J. R. O'Connor, Proc. IRE 50, 219 (1962).

8. B. Lax, W. P. Allis, and S. C. Brown, J. Appl. Phys. 21, 1297 (1950).

9. L. Gould and L. W. Roberts, J. Appl. Phys. 27, 1162 (1956).

10. R. G. Meyerand, Jr., and A. F. Haught, Phys. Rev. Letters 11, 401 (1963).

11. R. W. Minck, J. Appl. Phys. 35, 252 (1964).

12. J. A. Bellisio, C. Freed, and H. A. Haus, Appl. Phys. Letters 4, 5 (1964).

13. E. M. Purcell, Nature 178, 1449 (1956).

14. F. G. Houtermans, Helv. Phys. Acta 33, 933 (1960).

III. MATERIALS RESEARCH

A. OPTICAL PYROMETER MEASUREMENT OF RF GENERATOR OUTPUT

We have found that the power output of an RF generator can be conveniently measured by determining the equilibrium temperature of a black-body load with an optical pyrometer and using the black-body formula to obtain the power radiated by the load. Graphite, with resistivity of about 10^{-3} ohm-cm, easy machinability, and good black-body characteristics, is an excellent dummy load for studying the output of RF generators to such relatively high-resistivity loads as plasmas and semiconductors.

The optical pyrometer method was tested by using it to measure the power transferred from a 5-kw 14-Mcps generator to a graphite cylinder heated in air, and comparing the results with those obtained by the conventional water-cooled calorimeter method.[1] First, water was circulated at a measured rate through the cylinder, and the power transferred at three different generator settings was calculated from the temperature rise of the water as it passed through the cylinder. Next, the cooling leads were removed, and the equilibrium temperatures of the cylinder for the same generator settings were measured with a disappearing-filament pyrometer which had been calibrated against a standard black body. The radiated power was calculated from these temperatures by assuming that the total emissivity of graphite is 0.80 (Ref. 2). The results obtained by the two methods, as given in Table III-1, agree to within 10 percent in all cases, and the agreement improves with increasing temperature. Apparently, the power radiated by the cylinder was large compared to the convection losses under the experimental conditions used.

TABLE III-1						
COMPARISON OF PYROMETER AND CALORIMETER POWER MEASUREMENTS						
RF Generator Conditions				Measured Power		
Plate Valtage (kv)	Plate Current (ma)	Grid Current (ma)	Plote Power (wotts)	Pyrometer Method ($^{\circ}$K)	(watts)	Calorimeter Method (watts)
2.27	500	50	1130	1200	685	621
3.40	750	75	2550	1520	1270	1324
4.42	1000	100	4420	1704	2270	2245

If the pyrometer method is to be used for long periods, it is necessary to protect the graphite against oxidation by using an inert gas or vacuum. However, graphite oxidizes slowly enough in air that the heat of oxidation and change in dimensions can be neglected for measurements lasting five or ten minutes.

The pyrometer method was used to determine the coupling efficiency of the RF generator as a function of the ratio of graphite cylinder diameter to coil diameter. Efficiencies of 27, 41, 59, and 63 percent were found for ratios of 0.46, 0.61, 0.77, and 0.92, respectively.

T. B. Reed
J. T. Roddy

B. VAPOR GROWTH OF CRYSTALS

1. Constitutional Supercooling in the Gas Phase

In order to obtain satisfactory single crystals by solidification, the growth rate must be low enough to prevent constitutional supercooling of the melt.[3] Our analysis of vapor growth shows that constitutional supercooling can also occur in the gas phase. The analysis yields an expression for the maximum growth rate which is possible without such supercooling. This rate is proportional to the temperature gradient in the gas phase, just as the maximum rate of stable growth from the melt is proportional to the temperature gradient in the melt.[4]

When a crystal grows from a dilute vapor transported either by natural convection or by a carrier gas, condensation of the vapor at the growth interface ($x = 0$) produces a gradient of partial pressure p in the gas phase ($x > 0$), as shown in Fig. III-1(a). Since there is a temperature gradient at the interface, there will also be a gradient of the saturated vapor pressure p_o, as shown in Fig. III-1(b). The stability of the interface depends upon the degree of saturation, $\sigma = (p - p_o)/p_o$. If dp_o/dx is greater than dp/dx at $x = 0$, as in Fig. III-1(c), the vapor is unsaturated ($\sigma < 0$) for $x > 0$, and the interface is stable. If dp_o/dx is less than dp/dx at $x = 0$, as in Fig. III-1(d), the vapor is supersaturated ($\sigma > 0$) in a region adjacent to the interface; the crystal may be expected to grow locally into this region, and surface roughness, platelike growth, or dendrite formation may result, depending on the degree of supersaturation. Thus, stable growth will occur only if $dp_o/dx \geqslant dp/dx$ at $x = 0$.

The molar growth rate of the crystal is equal to $v\rho/M$, where v is the linear growth velocity, ρ is the crystal density, and M is the molecular weight. There is always a layer adjacent to the growth interface through which the vapor is transported to the interface entirely by diffusion. The rate of diffusion is given by $D(dC/dx)$, where D is the diffusion constant of the vapor and $C = p/RT$ is the concentration. Setting the diffusion rate equal to the molar growth rate,

$$\frac{dp}{dx} = \frac{RT\rho v}{DM} + \frac{P}{T}\left(\frac{dT}{dx}\right) \quad . \tag{1}$$

Since $p_o = A \exp[-B/T]$, where A and B are constants and T is the absolute temperature, $(dp_o/dT) = Bp_o/T^2$. From $(dp_o/dx) = G(dp_o/dT)$, where G is the thermal gradient in the gas phase,

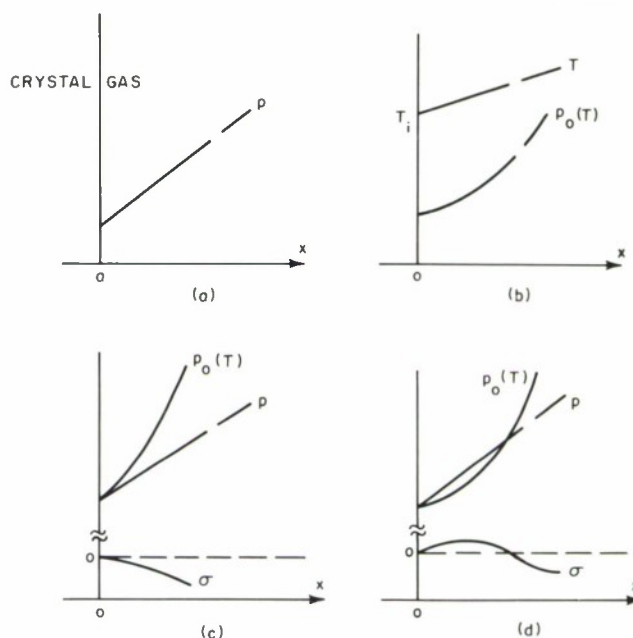$$\frac{dp_o}{dx} = \frac{p_o GB}{T^2} \quad . \tag{2}$$

Fig. III-1. Vapor constitutional supercooling. (a) Partial pressure gradient at growing interface. (b) Temperature gradient and associated saturated vapor pressure at growing interface. (c) p lies below p_0 for $x > 0$, $\sigma < 0$, and the interface is stable. (d) p lies above p_0 for $x > 0$, $\sigma > 0$, area beyond interface is supercooled, and interface may be unstable.

The maximum velocity for stable crystal growth is found by setting Eq. (1) equal to Eq. (2) and solving for v:

$$v_{max} = \frac{MDp_0}{\rho RT^2} \left(\frac{B}{T} - 1 \right) G \quad .$$

(3)

Values of v_{max} calculated from Eq. (3), for a reasonable choice of parameters, are within the range of linear growth velocities encountered in vapor growth. Although published experimental data are not generally sufficient to determine whether constitutional supercooling accounts for reported cases of dendritic growth, evidence for constitutional supercooling is being obtained in experiments on the vapor growth of iodine (see Sec. III-B-2).

T. B. Reed
W. J. LaFleur

2. Forced Convection Growth of Iodine Crystals

The apparatus[5] previously used in studying growth of iodine crystals has been replaced by a new apparatus which permits adjustment of the temperature gradient in the gas phase near the growth interface and measurement of temperatures in the gas phase and at the interface, as well as in the crystal. This apparatus has been used to study the influence of constitutional supercooling on interface morphology and the dependence of linear growth velocity on supersaturation.

The new apparatus is shown schematically in Fig. III-2. A Pyrex tube about one inch in diameter and two feet long is immersed in a water thermostat. (The tube is actually U-shaped, although drawn straight in Fig. III-2.) Inert gas entering the tube becomes saturated with iodine at the thermostat temperature T_0, is heated by means of an auxiliary heater to a temperature T_2,
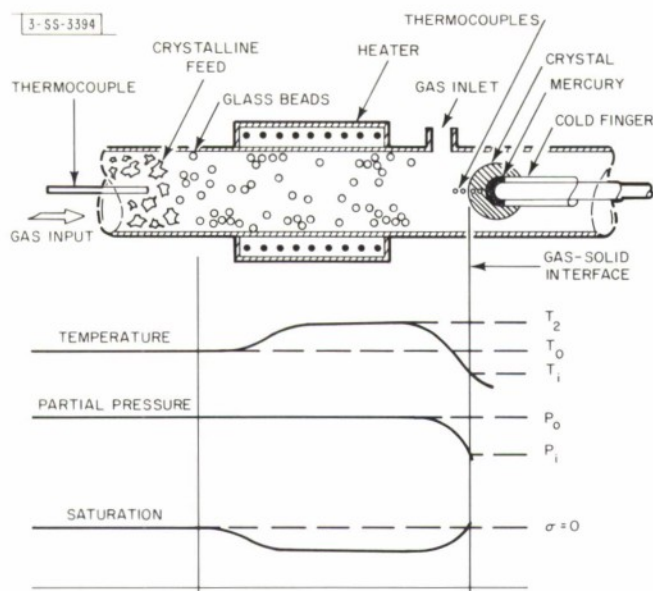
Fig. III-2. Apparatus for forced convection growth of iodine crystals.

and then passes around a glass cold finger where condensation occurs. The linear velocity of crystal growth on the cold finger is observed with a cathetometer. A gas inlet between the auxiliary heater and the cold finger permits the introduction of inert gas so that iodine can be removed from the cold finger by evaporation at a controlled rate. A thermocouple is located at the end of the iodine feed bed, and four thermocouples are mounted along the axis of the tube at 1-mm intervals from the tip of the cold finger. From the thermocouple readings, it is possible to determine the temperature at the interface and the thermal gradient in the gas phase, which can be adjusted by changing T_2. The variations in temperature, pressure, and degree of saturation along the tube under operating conditions are shown schematically in Fig. III-2.

Evidence for constitutional supercooling in the gas phase has been obtained in measurements of the linear growth velocity v as a function of interface temperature T_i for a flow rate of 1 liter/hour of helium saturated with iodine at $T_o = 90°C$. The variation of v with $T_o - T_i$ is shown in Fig. III-3. The crystal surface is extremely smooth [Fig. III-4(a)] for values of v up to about 1.3 mm/hour but becomes rough [Fig. III-4(b)] for higher velocities. In good agreement with this observation, $v_{max} = 1.6$ mm/hour is calculated from Eq. (3) by using the observed values $T_i = 82°C$ and $G = 3.1$ deg/cm, together with the calculated[6] value $D = 0.5$ cm^2/sec.

The degree of supersaturation required to sustain crystal growth from the vapor has been extensively studied. From Fig. III-3, an upper limit of 0.0075 (corresponding to a maximum supercooling of 0.2°C) is obtained from the variation of v with $T_o - T_i$ in the vicinity of the origin, for both positive and negative values of v. A supersaturation of 0.2 was required to nucleate the growth of iodine crystals on the clean cold finger.

T. B. Reed
W. J. LaFleur

Fig. III-3. Variation of linear growth velocity v with degree of supercooling $(T_o - T_i)$ in forced convection growth of iodine crystals.
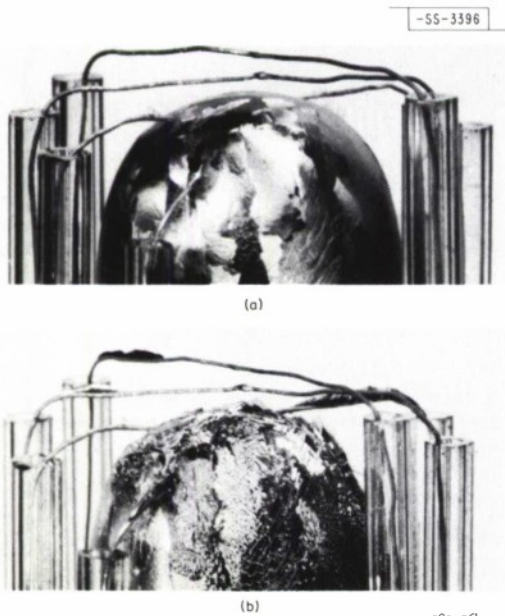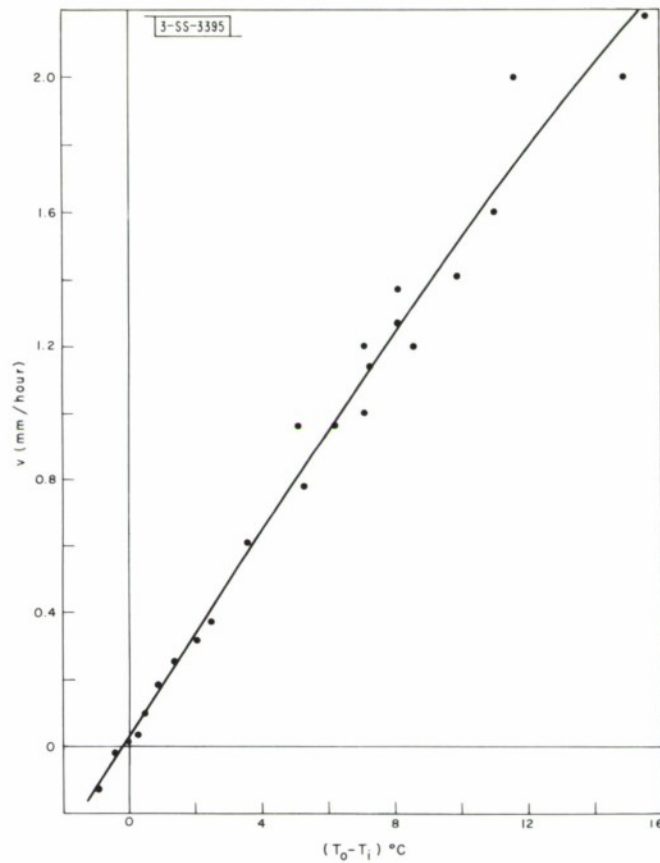
Fig. III-4. Iodine grown at two different rates by forced convection. The pattern of grains is the same in both cases, since growth occurred on the same substrate. The wires shown are the measuring thermocouples. (a) Linear growth velocity = 0.2 mm/hour. (b) Linear growth velocity = 1.5 mm/hour.
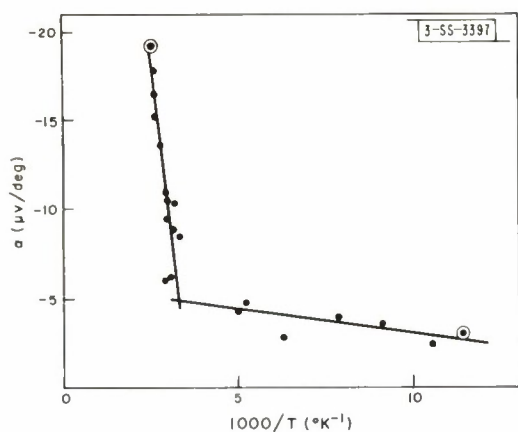
Fig. III-5. Seebeck coefficient σ vs reciprocal temperature for polycrystalline CrO_2.

Fig. III-6. Seebeck coefficient σ vs reciprocal temperature for polycrystalline CrO_{2+y}.
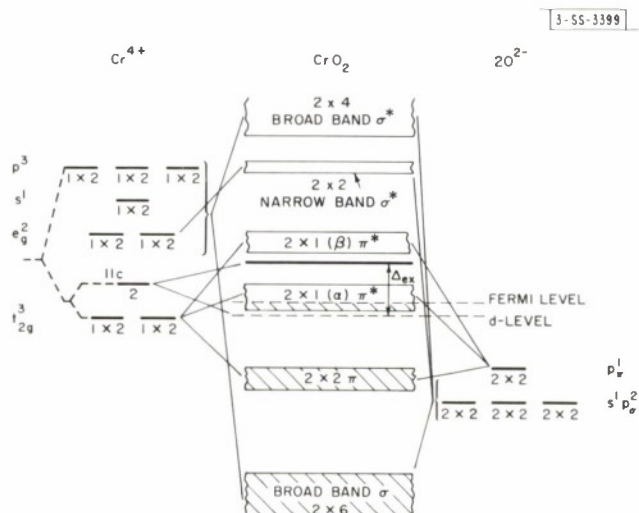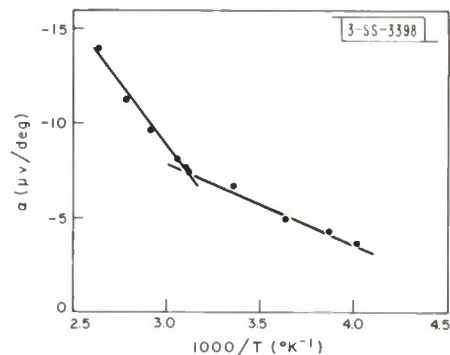
Fig. III-7. Schematic molecular orbital energy diagram for ferromagnetic CrO_2. The numbers at each level represent the number of ions per formula unit and the spin degeneracy, respectively. The numbers in each band represent the total number of orbitals per formula unit and the spin degeneracy, respectively. (With two molecules per unit cell, π^* bands could be further split into two parts which would render a stoichiometric compound semiconducting.)

C. ELECTRICAL PROPERTIES OF TRANSITION METAL OXIDES

1. Ferromagnetic CrO_2 and CrO_{2+y}

The Seebeck coefficient α and resistivity ρ of polycrystalline CrO_2 prepared under high pressure[7] have been measured in a new low-temperature apparatus. The variation of α with $10^3/T$ is shown in Fig. III-5. The data can be represented by two straight lines intersecting at approximately 300°K. Some hysteresis was observed in the measurements of ρ. The value of ρ, which is approximately 3 milliohm-cm at 88°K, increases with temperature over the range 88° to 400°K at a rate corresponding to an activation energy of approximately -7×10^{-3} ev.

An attempt has been made to prepare hot pressed samples of CrO_{2+y} in which excess oxygen is incorporated into the rutile-type lattice of CrO_2. Although the samples obtained do not exhibit deviations from stoichiometry large enough to be detected by the available analytical techniques, a small decrease in lattice constant relative to the CrO_2 sample described above indicates that they may contain excess oxygen. The value of ρ which is 29 milliohm-cm at 20°C, decreases with temperature at a rate corresponding to an activation energy of 6×10^{-3} ev, rather than increasing with temperature as in CrO_2. In the resistivity measurements, little hysteresis was observed between −35° and 20°C, but marked hysteresis occurred in the region 20° to 100°C. Values of α for a CrO_{2+y} sample are plotted against $10^3/T$ in Fig. III-6. As in the case of CrO_2, the data can be represented by two straight lines, intersecting for this sample at about 320°K.

We believe that the observed ferromagnetism and metallic conductivity of CrO_2 can be explained by the molecular orbital energy diagram shown in Fig. III-7, which is based on a model proposed by Goodenough[8] for his "class 2" oxides. Since CrO_2 has the rutile structure, the Cr^{4+} ions are surrounded octahedrally by O^{2-} ions, and each O^{2-} ion is in a nearly coplanar environment of three Cr^{4+} ions. Therefore, bonding occurs between sp^3d^2 Cr and sp_σ^2 O orbitals, forming a broad band occupied by 12 electrons per chromium ion. An additional four electrons are accommodated by π bonding and antibonding bands formed between the t_{2g}^2 orbitals of chromium which are not parallel to the c-axis and the p_π orbitals of two adjacent oxygen ions. Of the two remaining electrons, one occupies the exchange-split t_{2g} orbital parallel to the c-axis, producing the observed ferromagnetism. The other fills the lowest level of the anti-bonding π^* band, producing the observed metallic conductivity.

<div align="right">

D. S. Chapin
J. A. Kafalas
J. M. Honig

</div>

2. Single-Crystal Cr_2O_3

Values of α and ρ measured along the $[01\bar{1}2]$ axis of a single crystal of Cr_2O_3 are plotted against $10^3/T$ in Figs. III-8 and III-9, respectively. Since α is positive, remaining in the range 400 to 1700 μv/deg, and decreases with temperature, the conductivity of the crystal is p-type, possibly due to the presence of traces of altervalent ions or of a slight excess of oxygen over the stoichiometric amount. The value of ρ, which was measured by the four-probe technique with a Cary vibrating reed electrometer, increases with decreasing temperature.

A one-electron energy diagram for Cr_2O_3, constructed according to the method of Goodenough,[8] is given in Fig. III-10. The lower exchange-split t_{2g} levels are completely filled with three electrons per chromium ion. On the basis of this diagram, Cr_2O_3 is expected to be a semiconductor

Fig. III-8. Seebeck coefficient o vs reciprocal temperature far single-crystal Cr_2O_3 meosured alang the $[01\bar{1}2]$ axis.

Fig. III-9. Resistivity ρ vs recipracal temperature for single-crystol Cr_2O_3 measured alang the $[01\bar{1}2]$ axis.

Fig. III-10. Schematic molecular orbitol energy diagram for Cr_2O_3. The numbers at each level represent the number af ions per formula unit and the spin degenerocy, respectively. The numbers in eoch band represent the totol number of orbitals per formula unit ond the spin degenerocy, respectively.
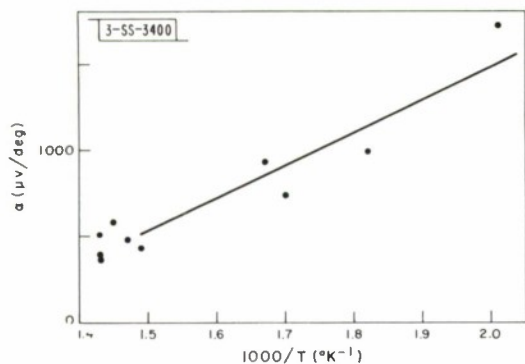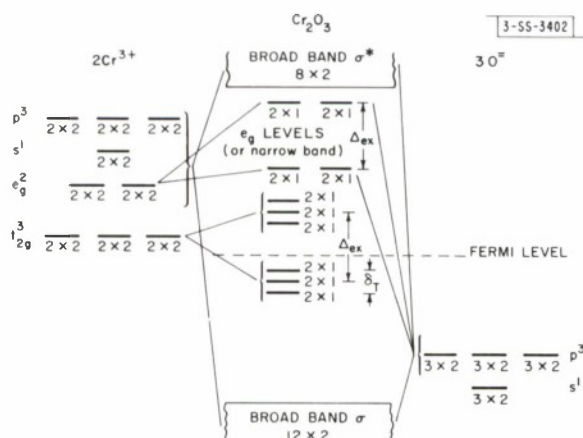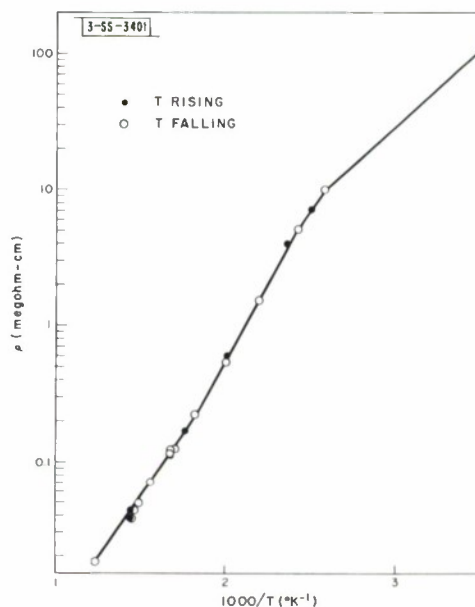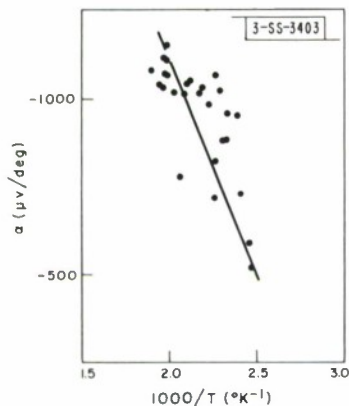
Fig. III-11. Seebeck coefficient a vs reciprocal temperature far single-crystal MnO measured along the [310] axis.

Fig. III-12. Resistance R vs reciprocal temperature far single-crystal MnO measured along the [310] axis.

with hopping-electron conductivity. The observed electrical properties are consistent with this prediction.

D. S. Chapin
J. M. Honig

3. Single-Crystal MnO

Values of α and resistance R measured along the [310] growth axis of a single crystal of MnO(Ref. 9) are plotted against $10^3/T$ in Figs. III-11 and III-12, respectively. Since α is negative and $|\alpha|$ increases with temperature, the conductivity of the crystal is n-type. At sufficiently high temperatures, R decreases with temperature at a rate corresponding to an activation energy of 0.6 ev. These properties are consistent with conduction by a hopping process.

D. S. Chapin
T. B. Reed
J. M. Honig

D. HEAT OF TRANSFORMATION OF Ag_2Se

Under atmospheric pressure Ag_2Se is transformed at about 130°C from the low-temperature α-form to the high-temperature β-form. Data for the pressure dependence of the transition temperature have been reported previously.[10] As a check on these data, a value for the heat of transformation has been calculated from them and compared with the value measured calorimetrically.

The calorimetric measurements were made with a Perkin-Elmer Model DSC-1 differential scanning calorimeter.† In this apparatus, the sample and a standard are heated or cooled at a constant rate, and the differential power necessary to keep the sample and standard temperatures

---

† The measurements were made through the courtesy and with the assistance of J. Justin, Perkin-Elmer Corporation, Norwalk, Connecticut.

equal throughout the run are recorded and integrated. For the experiments on Ag_2Se, the calorimeter was calibrated by melting-freezing runs on high-purity indium (T_m = 156.6°C, ΔH_m = 0.78 ± 0.02 kcal/g-atom). The heat of transformation (ΔH_t) for Ag_2Se was found to be 2.19 kcal/mole, 36 percent higher than the only published value, 1.61 kcal/mole, reported in 1888 (Ref. 11). The $\alpha \rightarrow \beta$ transition on heating began at 132.5°C and the reverse transition on cooling began at 113°C, in good agreement with the temperatures observed in resistivity measurements.

The value of ΔH_t, calculated from the pressure data, was obtained by applying the thermodynamic relation (dT/dP) = $T\Delta V/\Delta H$. The initial slope of the transition temperature vs pressure curve (Fig. III-7, Ref. 10) is (dT/dP) = 6.2°C/kbar. The molar volumes of the α- and β-phases, calculated from lattice parameter data,[12-14] are 35.57 and 37.26 cm^3/mole, respectively. From these values and the transition temperature of 406°K we obtain ΔH_t = 2.56 kcal/mole, in fairly good agreement with the calorimetric value. Since V_α and V_β were obtained from lattice parameters measured at 298° and 443°K, respectively, the value of ΔV used in the calculation is greater than the actual value at the transition temperature. Use of the true value of ΔV would reduce ΔH_t and improve its agreement with the result obtained calorimetrically.

<div align="right">M. D. Banus</div>

E. RATE OF CUBIC-TO-HEXAGONAL TRANSFORMATION IN $PrO_{1.5}$

The temperature dependence of the rate at which cubic $PrO_{1.5}$ is transformed into the stable hexagonal form has been investigated by annealing samples of the cubic phase in a high-temperature x-ray diffraction camera. The samples were freshly prepared by hydrogen reduction and sealed under vacuum in outgassed quartz capillaries under conditions designed to exclude residual gases, particularly water vapor. The results of the experiments are in good agreement with those obtained previously[15] by x-ray measurements made at room temperature on samples which were prepared in the same manner, annealed, and then quenched. In the previous experiments, it was found that substantial transformation occurred at about 800°C for samples annealed for 96 hours and at about 850°C for samples annealed for six minutes. In one series of high-temperature measurements, no x-ray lines due to the hexagonal phase were observed after 33 hours at 793°C, weak lines were observed after an additional 65 hours at 793°C, and strong lines were observed after an additional 33 hours at 808°C.

We believe that the variation reported in the literature for the transformation temperature of $PrO_{1.5}$ is due to differences between samples in their residual gas content (particularly water vapor) and in stoichiometry. The effect of water vapor has been studied by room-temperature x-ray measurements on samples exposed at room temperature to water vapor at a partial pressure of 5×10^{-4} torr before annealing and quenching. The results indicate that this treatment reduces the temperature for a given transformation rate by about 60°C.

<div align="right">D. S. Chapin
Mary C. Finn
J. M. Honig</div>

F. RATE OF TRANSFORMATION IN $InSb_{II}$-Sn ALLOYS

The mutual solubility of $InSb_{II}$ (high-pressure tetragonal phase) and β-Sn (tetragonal phase) is much greater than that of $InSb_I$ (atmospheric pressure zincblende phase) and β-Sn.

Superconductivity data[16] indicate that solutions containing up to 2.5 to 5 percent Sn ("β" will be omitted hereafter) in $InSb_{II}$ and about 35 percent $InSb_{II}$ in tin can be prepared at high pressure, whereas the solubilities at atmospheric pressure are less than 0.5 percent for tin in $InSb_I$ and about 8 percent for $InSb_I$ in tin. The $InSb_{II}$-Sn alloys, as well as $InSb_{II}$, are obtained as meta-stable phases at atmospheric pressure if they are cooled to liquid nitrogen temperature (77°K) before the high pressure is released. They are retained indefinitely if kept at 77°K but are transformed into the stable two-phase mixtures at sufficiently high temperatures.

We have used resistivity measurements to investigate the temperature dependence of the transformation rates. The measurements were made by the van der Pauw method,[17] using a point-contact apparatus. The samples were disks prepared[16] from high-purity InSb and tin in a "belt" high pressure apparatus at 37 kbar by first heating to 450° to 480°C (well above the melting points of $InSb_{II}$ and tin) for two hours, and then annealing in the solid state at 300°C before quenching to liquid nitrogen temperature.

For $(InSb)_{1-x}(2\ Sn)_x$ samples with x between 0 and 0.3, the resistivity was measured as the samples were allowed to warm up slowly from 77°K to room temperature. A typical drift run required six to eight hours. Results of these measurements are shown in Fig. III-13, where the resistivities are expressed relative to the values at 77°K. (The samples were annealed at 37 kbar for one hour at 300°C, like those in the superconductivity experiments.[16]) The resistivity of each sample first rises approximately linearly with temperature and then increases sharply over a narrow temperature range. In the linear region, the transformation rate is sufficiently small compared to the heating rate for the metastable phase to be retained. The abrupt increase in resistivity results from transformation to the stable phase, which occurs over a narrow range because the transformation rate is such a strong function of temperature. The transformation from $InSb_{II}$ to $InSb_I$ occurs at 200° to 210°K, as reported previously.[18] For the alloys, the effective transition temperature increases systematically with increasing tin content, reaching 280° to 290°K for x = 0.30. This continuing increase indicates that the solid solubility of tin in $InSb_{II}$ is greater than 20 percent rather than only 5 percent.

Evidence for still greater solubility of tin in $InSb_{II}$ is obtained from measurements of resistivity as a function of time at various fixed temperatures for x = 0.40 and 0.50. For these compositions, the rate of transformation is so slow that in a drift run the resistivity remains in the linear region almost up to room temperature. The samples, for which the period of annealing at 300°C under pressure was extended to 20 hours, were transferred directly from liquid nitrogen to an appropriate constant temperature bath. The results are given in Fig. III-14, where the resistivities are expressed relative to the first value measured after the sample had reached the bath temperature. At both 273° and 298°K, the rate of transformation is appreciably greater for x = 0.40 than for x = 0.50. This change in rate indicates that the solubility of tin in $InSb_{II}$ exceeds 40 percent. Detailed data for the first 24-hour period at constant temperature, which are not given in Fig. III-14, show that valid x-ray data for the untransformed alloys can be obtained if the measurements are completed within 24 hours at 240°K for x = 0.40 and within three hours at 298°K or eight hours at 273°K for x = 0.50. No evidence of transformation at 195°K was obtained for either x = 0.50 (data not shown) or for x = 0.40 over the entire period of measurement.
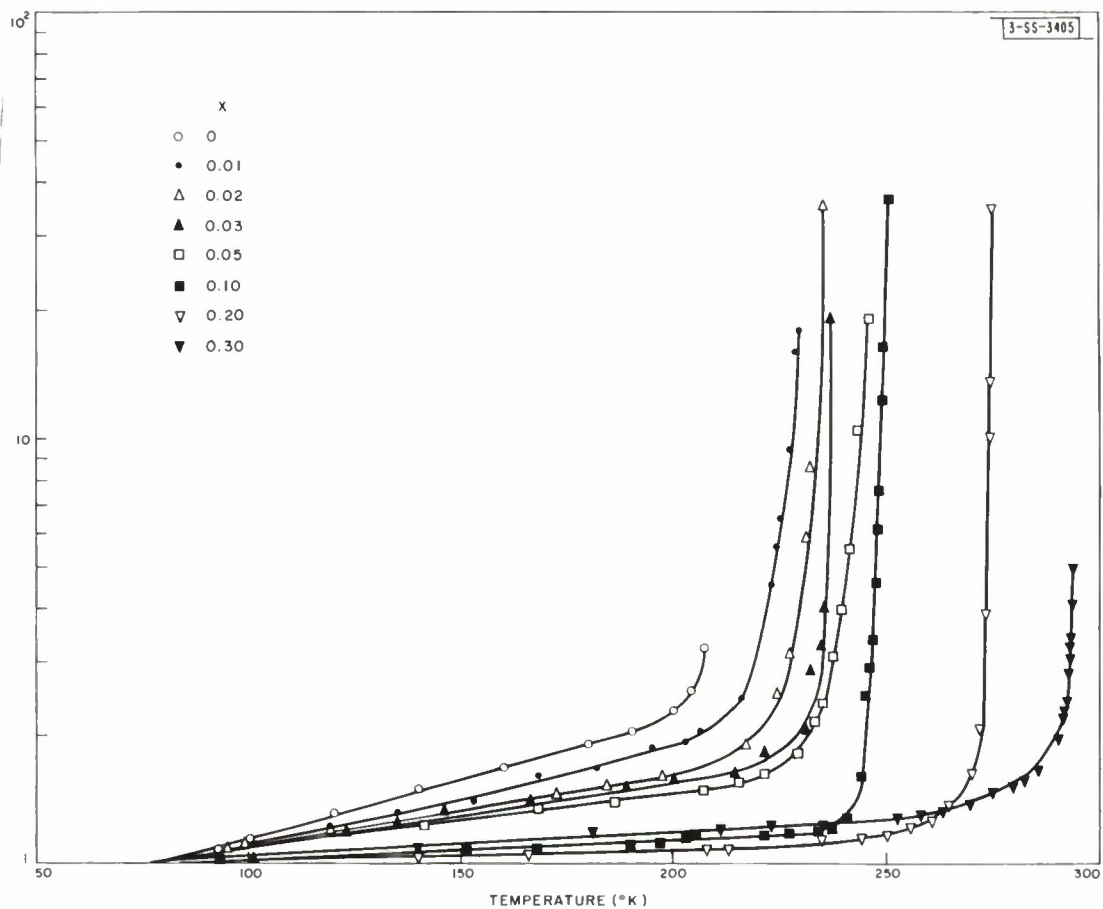
Fig. III-13. Variation of resistivity ratio (ρ/ρ_{77}) with absolute temperature measured in temperature drift runs an $(InSb)_{1-x}(2\,Sn)_x$ samples. Curves terminate at temperatures where cantacts became erratic due ta changes in sample dimensions.
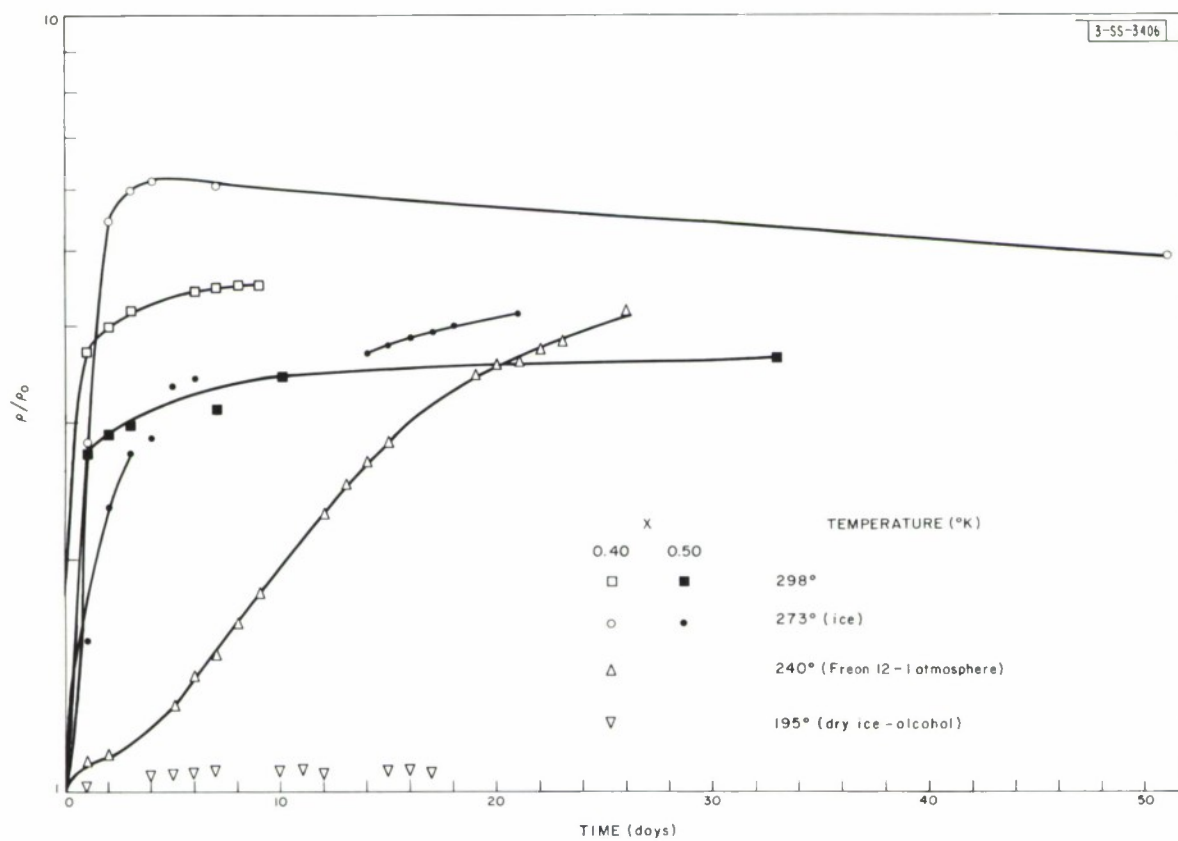
Fig. III-14. Variation of relative resistance (ρ/ρ_o) with time measured in constant temperature runs on $(InSb)_{1-x}(2\,Sn)_x$ samples.
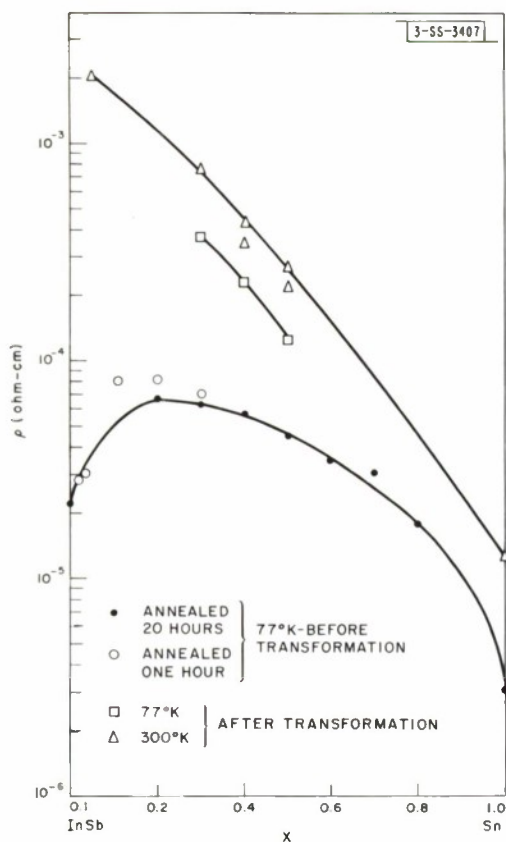
Fig. III-15. Resistivity ρ vs composition x for $(InSb)_{1-x}(2\,Sn)_x$ samples.

Fig. III-16. Resistance R vs applied load for $Cd_xHg_{1-x}Te$. An applied load of two tons produces a pressure of approximately 1 kbar.
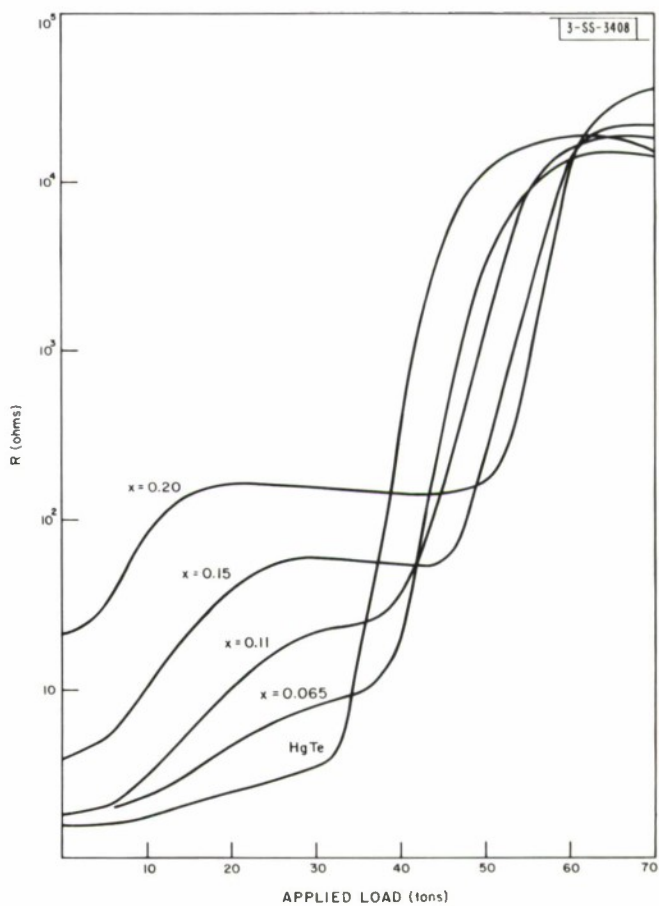
Absolute resistivity values for $InSb_{II}$-Sn samples at 77°K, and for some of these samples at 300° and 77°K after they had transformed into the stable forms, are plotted as a function of composition in Fig. III-15. In some cases, final values could not be obtained because the samples were pulverized during transformation. The data for the pure tin sample, which was subjected to the same pressure treatment as the alloys, are in good agreement with published values.[19]

M. D. Banus
Lynne B. Farrell
A. J. Strauss

G. PRESSURE DEPENDENCE OF RESISTANCE OF $Cd_xHg_{1-x}Te$

The room-temperature resistance R of $Cd_xHg_{1-x}Te$ samples with x between 0 and 0.20 has been measured as a function of pressure up to 70 kbar. The measurements were made with an opposed anvil apparatus[20] on powdered specimens obtained from ingots prepared by the Bridgman method. The results are shown in Fig. III-16. The resistance of HgTe, after initially rising slowly, rapidly increases by four orders of magnitude at about 15 kbar. The abrupt increase is due to a phase transformation, found by x-ray diffraction measurements,[21] from the low-pressure zincblende structure to the hexagonal cinnabar (HgS) structure. A similar increase in R is observed at pressures somewhat higher than 15 kbar for the samples containing cadmium. Since $Cd_xHg_{1-x}Te$ alloys all have the zincblende structure at atmospheric pressure, it can be assumed that this increase is caused by the same type of transformation as in HgTe.

Significant changes in the pressure dependence of R below the transformation pressure are produced by alloying with CdTe. The initial rate of increase in R increases with x, and R reaches a limiting value for the higher values of x. In this region the variation of R is probably due primarily to the effect of pressure on the electronic band structure. Further pressure experiments are planned in order to investigate the band structure of the alloys, which are semimetals for x below approximately 0.20 and semiconductors for higher values of x (Ref. 22).

J. A. Kafalas

H. PARTIAL PRESSURES AND GIBBS FREE ENERGY OF FORMATION FOR CdTe(c)

The vapor in equilibrium with CdTe(c) consists of Cd(g) and Te_2(g). The partial pressures of these species in equilibrium with congruently subliming CdTe(c) between 780° and 939°C have been determined by measuring the optical density of the vapor with a Cary Model 14-H double-beam spectrophotometer. The procedure was generally similar to the one used in studying partial pressures in the Pb-Te system.[23] Values of p_{Cd} and p_{Te_2} were calculated from the absorption at selected wavelengths (2287 for cadmium; 3650, 4357, and 5000 Å for Te_2) by using Beer's law relationships between optical density and pressure obtained by combining the results of calibration experiments on pure cadmium and tellurium with published vapor pressure data for these elements.

The measured partial pressures obey the relationship $p_{Cd} = 2p_{Te_2}$ which is characteristic of the vapor in equilibrium with congruently subliming CdTe(c). Since this vapor has the same average composition as the solid, it must be stoichiometric to within about 10^{-3} atomic percent, the maximum deviation from stoichiometry in CdTe(c). The values of p_{Te_2} vary with reciprocal absolute temperature according to the expression $\log p_{Te_2}$ (atmospheres) $= -(1.00 \times 10^4)/T + 6.346$.

If the vapor phase is ideal, the Gibbs free energy of formation of CdTe(c) from a standard state of Cd(g, one atmosphere) and Te_2(g, one atmosphere) is given by $\Delta G°[CdTe(c)] = RT \ln p_{Cd}(p_{Te_2})^{1/2}$. (A correction term for deviations from stoichiometry is omitted, since its value is calculated to be less than 10^{-3} kcal/mole up to 1000°C.) Substitution of the experimental results into this expression gives $\Delta G°[CdTe(c)] = -68.64 + 44.94 (10^{-3})$ T kcal/mole, in good agreement with equations which represent the data obtained in electrochemical[24] and effusion[25, 26] experiments at lower temperatures.

<div align="right">
R. F. Brebrick
A. J. Strauss
</div>

I.   WET CHEMICAL ANALYSIS

1.   MnO and CoO

Manganese in MnO and cobalt in CoO have been determined to an accuracy of within two parts per 1000 by automatic potentiometric EDTA titrations using the Reilley gold amalgam electrode.[27] Both elements were titrated directly in an NH_4OH-NH_4NO_3 buffer, manganese at pH 9.1 and cobalt at pH 10.0. A similar method was used for determining nickel in NiO (Ref. 28).

2.   In-Sb-Te System

Analytical methods, based on our procedure for analysis of In-Te samples[29] and on the work of Safronkova and Lyalikov,[30] are being developed for the analysis by automatic titration of samples containing indium, antimony, and tellurium as the major constituents. Satisfactory results have been obtained so far in analyses of samples weighing 0.5 gram or more, and extension of the method to smaller samples is being studied.

As in the In-Te procedure, indium is determined by direct titration with EDTA to a potentiometric endpoint, using the Reilley electrode.[27] It was necessary to modify the original method by increasing the pH from 2.4 to 5.3 and adding tartaric acid to prevent the hydrolysis of antimony and tellurium.

The dichromate oxidation of Te(IV) used in the In-Te procedure is unsuitable for In-Sb-Te samples, since Sb(III) is also oxidized by potassium dichromate. A substitute procedure has been adopted in which Te(IV) is reduced with potassium iodide and the liberated iodine is titrated with sodium thiosulfate. The endpoint is obtained by an amperometric method,[31] with the current due to a fixed voltage of 110 mv across duo-platinum electrodes being plotted automatically against titrant volume.

Antimony is determined by oxidation with potassium bromate to a potentiometric endpoint, using a potassium indicator electrode. Potassium permanganate, which is sometimes used in antimony determinations, is unsuitable because it also oxidizes Te(IV).

<div align="right">
M. C. Gardels
J. C. Cornwell
</div>

REFERENCES

1. R.A. Schrack, Radio Frequency Power Measurements, National Bureau of Standards Circular 536 (1953).

2. W.D. Kingery, Property Measurements at High Temperatures (Wiley, New York, 1959), p. 387.

3. J.W. Rutter and B. Chalmers, Can. J. Phys. 31, 15 (1953).

4. W.A. Tiller, K.A. Jackson, J.W. Rutter, and B. Chalmers, Acta Met. 1, 428 (1953).

5. Solid State Research Report, Lincoln Laboratory, M.I.T. (1963:4), p. 33, DDC 435023.

6. W.M. Rohsenow and H.Y. Choi, Heat, Mass, and Momentum Transfer (Prentice-Hall, Englewood Cliffs, N.J., 1961), p. 382.

7. Solid State Research Report, Lincoln Laboratory, M.I.T. (1963:3), p. 25, DDC 427340.

8. J.B. Goodenough, International Colloquium of the Centre National de la Recherche Scientifique, The Oxy-Compounds of the Transition Elements in the Solid State, Bordeaux, France (24-27 September 1964) (to be presented).

9. Solid State Research Report, Lincoln Laboratory, M.I.T. (1964:1), p. 27, DDC 601830.

10. Ibid., p. 33.

11. M. Bellati and S. Lussana, Alti. ist. Veneto (Ser. 6) 7, 1051 (1888-89).

12. P. Junod, Helv. Phys. Acta 32, 567 (1959).

13. J.B. Conn and R.C. Taylor, J. Electrochem. Soc. 107, 977 (1960).

14. R. Simon, R.C. Bourke, and E.H. Lougher, Adv. Energy Conv. 3, 481 (1963).

15. Solid State Research Report, Lincoln Laboratory, M.I.T. (1964:1), p. 33.

16. S.D. Nye, M.D. Banus, and H.C. Gatos, J. Appl. Phys. 35, 1361 (1964).

17. L.J. van der Pauw, Philips Research Reports 13, 1 (1958).

18. R.E. Hanneman, M.D. Banus, and H.C. Gatos, J. Phys. Chem. Solids 25, 293 (1964).

19. International Critical Tables (McGraw-Hill, New York, 1929), Vol. 6, p. 129.

20. J.A. Kafalas, H.C. Gatos, M.C. Lavine, and M.D. Banus, J. Phys. Chem. Solids 22, 1541 (1962).

21. A.N. Mariano and E.P. Warekois, Science 142, 672 (1963).

22. A.J. Strauss, T.C. Harman, J.G. Mavroides, D.H. Dickey, and M.S. Dresselhaus, Proceedings of the International Conference on Semiconductors, Exeter (1962), p. 703.

23. R.F. Brebrick and A.J. Strauss, J. Phys. Chem. 40, 3230 (1964).

24. J.H. McAteer and H. Seltz, J. Am. Chem. Soc. 58, 2851 (1963).

25. P. Goldfinger and M. Jeunehomme, Trans. Faraday Soc. 59, 2851 (1963).

26. I.V. Korneeva, A.V. Belyaev, and A.V. Novoselova, Russ. J. Inorg. Chem. 5, 1 (1960).

27. C.N. Reilley, R.W. Schmidt, and D.W. Lamson, Anal Chem. 30, 953 (1958).

28. Solid State Research Report, Lincoln Laboratory, M.I.T. (1964:1), p. 39, DDC 601830.

29. Solid State Research Report, Lincoln Laboratory, M.I.T. (1962:4), p. 28, DDC 400709.

30. N.N. Safronkova and Yu. S. Lyalikov, Zarod. Lab. 27, 21 (1961).

31. L. Levin and W.B. Swann, Talanta 1, 276 (1958).

IV. BAND STRUCTURE AND SPECTROSCOPY OF SOLIDS

A. RESTSTRAHLEN REFLECTION IN HgTe

During studies of the optical and magneto-optical properties of the HgTe-CdTe alloy system, the reststrahlen band in HgTe was observed by cooling relatively pure samples to a low enough temperature so that the plasma edge, due to free carriers, occurred at a much longer wavelength than the wavelength corresponding to the lattice vibration frequency. At approximately $10\,°K$, this latter wavelength is about 85 microns, whereas the plasma edge lies beyond 180 microns.

A trace of the variation of the observed reflectivity as a function of wavelength is shown in Fig. IV-1. Also included in this figure is a theoretical curve obtained by assuming a single classical Lorentz oscillator model. The parameters obtained from the theoretical fit are as follows: lattice absorption frequency $\nu_o = 3.45 \times 10^{12}$, high-frequency dielectric constant $\epsilon_o = 14$, and effective charge $q^* = 0.6\,e$. Comparison of the observed fundamental absorption frequency in HgTe with that of CdTe indicates that the force constants of these two materials are within 10 percent of each other.

The flat behavior displayed at the short wavelength end of the reststrahlen curve is unlike that predicted by either a single oscillator, or two oscillators with reasonable parameters. A Kramers-Kronig analysis of the experimental data indicates that, in addition to the sharp fundamental lattice absorption, there is a broader background absorption which peaks at approximately 70 microns. The mechanism for this broader absorption has not yet been established; however, one possibility is that this region marks the onset of an interband transition. This work has been accepted for publication in Solid State Communications.

D. H. Dickey
J. G. Mavroides

B. OPTICAL deHAAS-SHUBNIKOV EFFECT IN ANTIMONY[†]

In the course of investigating the magnetic field dependence of the optical reflectivity of a single crystal antimony surface, two general types of magnetic behavior have been observed in the photon energy range $0.1 < \hbar\omega < 0.3$ ev:

(1) A large nonoscillatory magnetoplasma effect, which is strongly dependent on photon energy, magnetic-field intensity, and crystal orientation,

(2) A smaller oscillatory term superimposed upon the magnetoplasma effect.

The oscillations in the reflectivity which are observed in the photon energy range $0.09 < \hbar\omega < 0.13$ ev have been attributed to the deHaas-Shubnikov mechanism. These oscillations are found to be most intense where the nonoscillatory magnetoplasma effect is largest, i.e., near the plasma edge.

Although the optical deHaas-Shubnikov effect has previously been discussed,[1] it is believed that the present experiment represents the first observation of the effect. On the basis of this
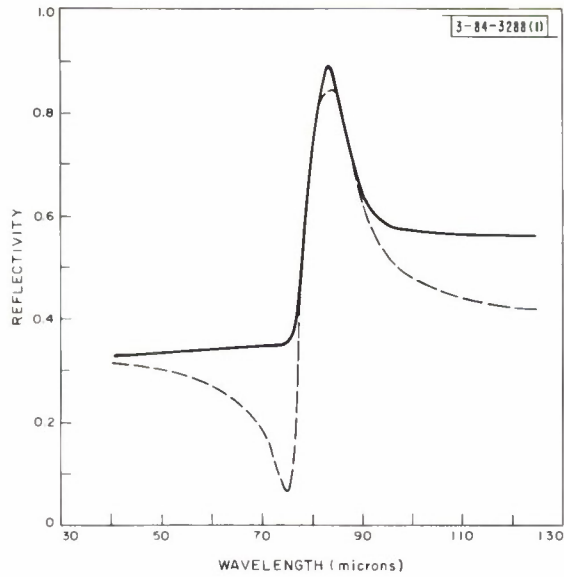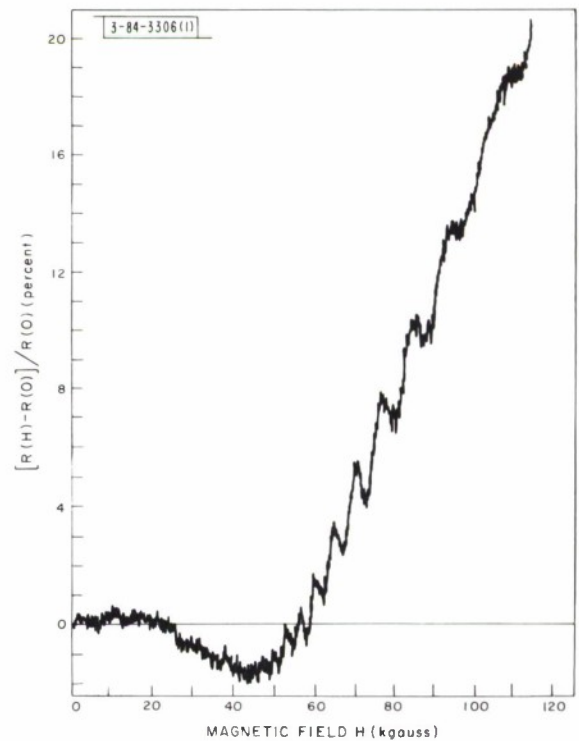
Fig. IV-1. Reststrohlen of HgTe. Solid curve is observed reflectivity ond doshed curve is colculoted on the basis of o Lorentz ascillotar. Porometers for oscillator ore given in the text.

Fig. IV-2. Variation of optical reflectivity with mognetic field ot $\hbar\omega = 0.1086$ ev for the mognetic field perpendicular to binary foce ond $T \sim 4°K$.

experiment, it would seem that any metal or semimetal exhibiting a deHaas-vanAlphen or a deHaas-Shubnikov effect could be expected to show optical deHaas-Shubnikov oscillations near the plasma edge.

A recorder trace showing the variation of the optical reflectivity with magnetic field at fixed photon energy, $\hbar\omega$ = 0.1086 ev, is given in Fig. IV-2 for a binary face. In this figure, the two basic types of magnetic behavior are demonstrated. The characteristic features of the optical deHaas-Shubnikov effect can be explained on the basis of a simple parabolic conduction band model of the metal. Analysis of the oscillatory magnetoreflection data in antimony yields values for the periods along the trigonal, binary, and bisectrix directions which are in good agreement with other determinations based on the oscillations in the magnetic susceptibility,[2] magnetoresistance,[3] and ultrasonic attenuation.[4]

This work will be submitted for publication.

Mildred S. Dresselhaus
J. G. Mavroides

C. INDIRECT TRANSITION IN GERMANIUM[†]

The magneto-absorption study of the indirect transition in germanium has been completed. The data were taken in the Faraday configuration (DC magnetic field parallel to propagation vector) for the cases of the propagation vector perpendicular to the (100), (111), and (110) faces, respectively. All measurements were made with the samples immersed in liquid helium which was pumped on to give a temperature of 1.7 °K. The data were taken using a 2-inch bore Bitter solenoid which gave magnetic fields of up to 74 kgauss. Although the optical system has a resolution of better than 0.1 mev, the factor limiting resolution experimentally was the inhomogeneity of the field over the (relatively) thick sample. This inhomogeneity, due to the radial access hole in the magnet which accommodates the dewar, gives rise to a broadening of the order of 0.2 to 0.3 mev.

An analysis of the data for the three orientations shows that the main transitions are from the top of the valence bands to the electronic ladders in the conduction band. A plot of the intensity ratio $I(H)/I(0)$ vs energy is shown in Fig. IV-3 for the [100] orientation. Strong transitions having periodic energy spacings were observed; these are indicated by the spacing A in the figure. When one divides the characteristic energy (eHh/m) = 0.85 mev by the energy spacings, one obtains effective masses that very clearly correspond to the electron effective masses in the conduction band for various orientations of the magnetic field. Fitting of the spacings for the three orientations gives, for the effective electron masses, the values shown in Table IV-1. These data are in excellent agreement with those obtained from cyclotron resonance measurements.[5] The effective masses associated with the individual ellipsoids in the conduction band are m_t = 0.079 m and m_ℓ = 1.74 m giving a mass ratio m_ℓ/m_t = 22.0.

The fine structure superposed on the periodic energy spacings reflects the energy level spacings in the valence bands. The peaks labelled 1 through 6 in Fig. IV-3 have been correlated with the valence band levels calculated by Goodman[6] for the [100] direction. Similarly, a number of valence band levels were identified in the results obtained for the [111] and [110] orientations.

---

† The experiment was carried out using the high-field facilities of the National Magnet Laboratory, M.I.T.

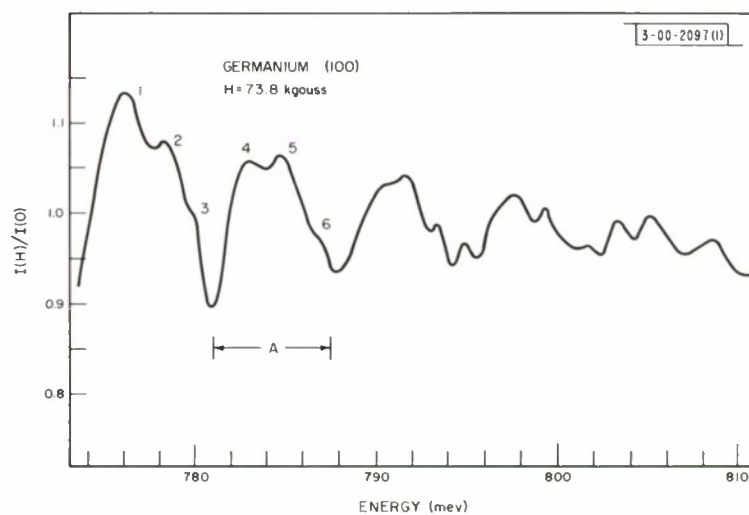| TABLE IV-1			
EFFECTIVE ELECTRON RESONANCE MASSES IN Ge			
Mognetic Field Direction	[100]	[111]	[110]
m^*/m	0.131 ± 0.003	0.197 ± 0.005 0.079 ± 0.002	0.340 ± 0.014 0.101 ± 0.002

Fig. IV-3. Plot of $[I(H)/I(0)]$ os o function of energy for [100] orientotion.

For both the [100] and [110] orientations, a splitting was observed in the first step of the transmission traces at the highest fields used (74 kgauss). This was interpreted as spin splitting in the conduction band since no other energy difference could fit it. These splittings correspond to electronic g-factors of (1.8 ± 0.3) and (1.5 ± 0.3), respectively, which are in agreement with the theoretical work of Roth and Lax.[7]

J. Halpern
B. Lax

D. ZEEMAN SPLITTING OF THE INDIRECT EXCITON IN GERMANIUM

The Zeeman splitting of the indirect exciton was investigated in the Faraday configuration. Data were obtained for the [100], [111], and [110] orientations. In Fig. IV-4 the energies corresponding to the peaks of the exciton absorption have been plotted as a function of magnetic field for H perpendicular to a (100) face. The solid curves in the figure represent transitions which can be followed unambiguously through the entire range of fields. Although one cannot state so with certainty, it appears, from the experimental data for all three orientations, that there is a crossing of the lines of the two components at the field values where the Zeeman splitting is of the same magnitude as the zero field splitting. The difficulty in identification arises from the fact that at the critical fields the entire spectrum converges.

The low and intermediate field data are consistent with the experimental results of Button, et al.,[8] and with the phenomenological Hamiltonian developed by Roth and Kleiner.[8] In the high-field region a linear behavior is observed; this is not surprising since in this régime the magnetic energy is much greater than the electric energy and one might expect the exciton line to follow the Landau level. Hence, it would be necessary to reformulate the theory for the high field region, since the Hamiltonian of Roth and Kleiner (which contains a quadratic term representing a diamagnetic contribution) clearly does not apply.
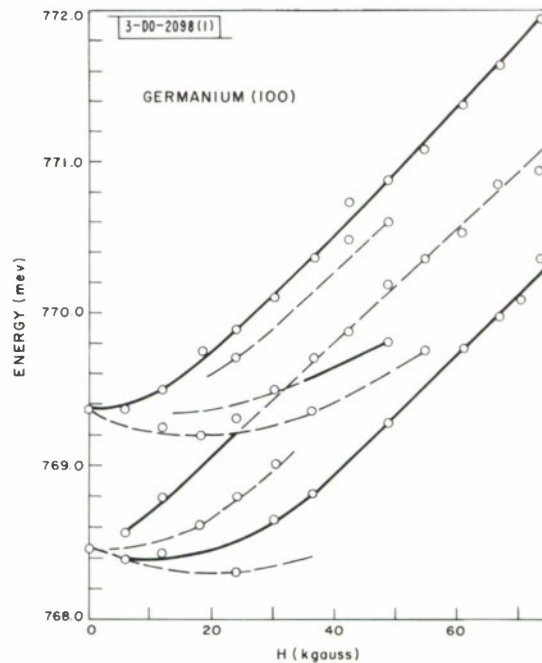
J. Halpern

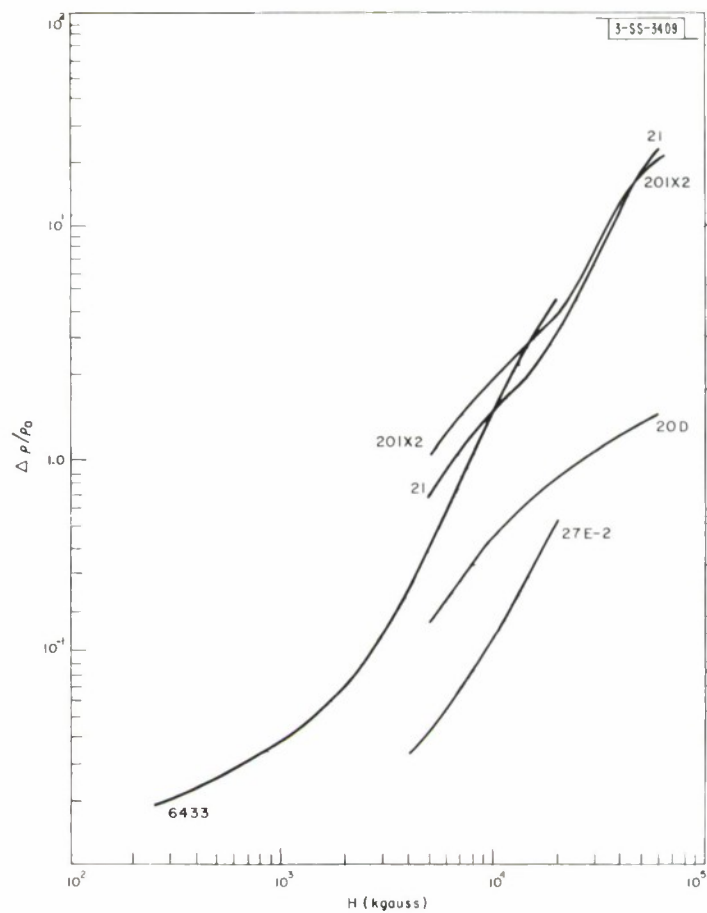Fig. IV-4. Zeeman spectrum of indirect exciton in germanium at 1.7°K for [100] orientation.

Fig. IV-5. Mognetoresistivity for HgTe ot 4.2°K.

E. ULTRAVIOLET REFLECTIVITY OF Mg_2Ge

Preliminary measurements at 77 °K on Mg_2Ge have indicated several peaks in the reflectivity at photon energies between 2.5 and 11 ev. An attempt is now being made to correlate the experimental results with Lee's[9] calculated band structure for this semiconductor. However, since the band structure calculation is limited in accuracy, it appears that definite assignments of the experimental peaks will probably not be possible until corresponding measurements and correlations have been made in Mg_2Si.

W. J. Scouler

F. MAGNETORESISTANCE AND MAGNETO-HALL EFFECTS IN HgTe

Measurements of magnetoresistance $(\Delta\rho/\rho_o)$ and Hall coefficient R as a function of magnetic field H have been initiated on rectangular bars of HgTe to obtain information on the charge carrier densities in this semimetal.

1. Anisotropy Experiments

To search for anisotropy, ρ was measured at 60 kgauss at 77° and 4.2 °K as a function of the angle of rotation of the sample about the direction of current flow perpendicular to the magnetic field. The samples were in the mixed conduction region (see below). The measured ρ values did not deviate by more than 8 percent from the mean. Since the conduction band is isotropic,[10] the effect of departures by the valence band from isotropy on electrical properties must be small. Thus, the isotropic mixed conduction theory[11] may be used as a first approximation to interpret the data cited below.

2. Variation of $\Delta\rho/\rho_o$ and R with H

The changes of $\Delta\rho/\rho_o$ and of R (which is negative) with H in the range $0 < H < 110$ kgauss at 4.2 °K are shown in Figs. IV-5 and IV-6 for several HgTe specimens. Sample 20D exhibits a marked decline of $|R|$ and a saturation of $\Delta\rho/\rho_o$ with increasing H. This variation of R with H is incompatible with one-band effects, but the experimental results are consistent with mixed conduction characterized by $p/n \gg 1$ and $p/n < b^2$, where n and p are the electron and hole densities and b is the electron to hole mobility ratio. Samples 21 and 201X2 show an irregular decrease of $|R|$ with increasing H, $\Delta\rho/\rho_o$ varying as H^2, and values of $\Delta\rho/\rho_o$ in excess of 20 at 60 kgauss. The magneto-Hall fluctuations at 4.2 °K may be due to quantum oscillatory effects; the magnetoresistance behavior is incompatible both with one-band and with nonoscillatory quantum effects. Here the p/n ratio is smaller than for sample 20D. Specimens 6433 and 30-B2 show only a weak decrease of $|R|$ with H, and for 6433, $\Delta\rho/\rho_o$ varies as H^2 and exceeds 4 at 20 kgauss; in these cases, p and n are roughly comparable in magnitude. Finally, for specimens 28-1, 27E-2, and 27-1, R is almost independent of H and relatively small; the measured $\Delta\rho/\rho_o$ are also less than for other samples. These results are compatible with the case $n/p \gg 1$.

This work provides further evidence for the semimetal band model previously proposed[12] for HgTe, since it shows that at 4.2 °K electrons and holes are present simultaneously in some samples at concentrations of the order of 10^{13} to 10^{16} cm^{-3}. If HgTe were a semiconductor, its intrinsic carrier concentration at 4.2 °K would be too small to permit the above mixed conduction effects to be observed. The data are being analyzed for a quantitative fit to theory.
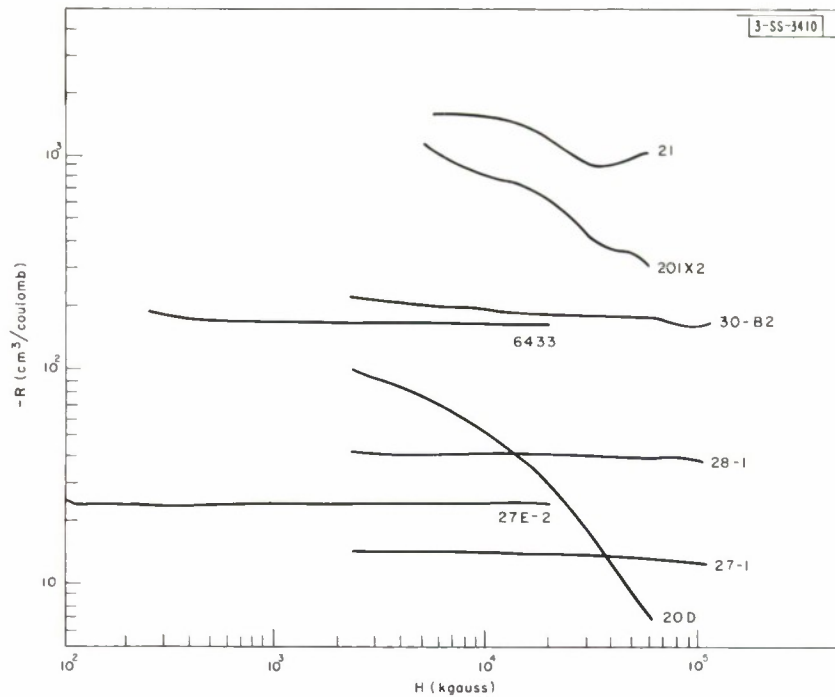
Fig. IV-6. Magneto-Hall measurements for HgTe at 4. 2°K.

Magnetoresistance and magneto-Hall data taken on three samples at 77 °K give results which are qualitatively similar to those for 4.2 °K.

T. C. Harman
J. M. Honig
A. J. Strauss

G. SYMMETRY THEORY OF SEEBECK COEFFICIENT IN A MAGNETIC FIELD

The symmetry theory has been developed for the Seebeck coefficient tensor field $\overleftrightarrow{\alpha}(\vec{H})$ of a crystal in a uniform magnetic field $\vec{H}$ of arbitrary strength. In zero field, $\overleftrightarrow{\alpha}$ is a polar tensor of second rank. Spatial symmetry leads to certain restrictions on the form of $\overleftrightarrow{\alpha}(\vec{H})$ and allows all information about $\overleftrightarrow{\alpha}(\vec{H})$ to be expressed in terms of a subregion of the space spanned by $\vec{H}$. Tables, which specify the above-mentioned restrictions and subregions for the symmetry directions of $\vec{H}$ for every crystal symmetry (magnetic as well as nonmagnetic), are being prepared to provide easy access to the results of symmetry theory.

The results have been found useful in developing the microscopic galvano-thermomagnetic theory of bismuth.[13,14]

When $\overleftrightarrow{\alpha}(\vec{H})$ is expanded in powers of the components of $\vec{H}$, the results of the theory lead to restrictions on the tensor expansion coefficients. Resulting special forms for these coefficients arc available in the literature[15-17] for the first few orders.

W. H. Kleiner

REFERENCES

1. M. Ia. Azbel', Zh. Eksperim. i Teor. Fiz. 34, 969 (1958) [translation: Soviet Phys. — JETP 7, 801 (1958)]; D.C. Mattis and G. Dresselhaus, Phys. Rev. 111, 403 (1958).

2. D. Shoenberg, Phil. Trans. Roy. Soc. (London) A245, 1 (1952); Y. Saito, J. Phys. Soc. Japan 18, 452 (1963).

3. J. Ketterson and Y. Eckstein, Phys. Rev. 132, 1885 (1963); G.N. Rao, H.N. Zebouni, C.G. Grenier, and J.M. Reynolds, Phys. Rev. 133, A141 (1964).

4. J.B. Ketterson, Phys. Rev. 129, 18 (1963).

5. B. Lax, H.J. Zeiger, and R.N. Dexter, Physica 20, 818 (1954).

6. R.R. Goodman, Ph.D. Thesis, University of Michigan (1958).

7. L.M. Roth and B. Lax, Phys. Rev. Letters 3, 217 (1959).

8. K.J. Button, L.M. Roth, W.H. Kleiner, S. Zwerdling, and B. Lax, Phys. Rev. Letters 2, 161 (1959).

9. P.M. Lee, Phys. Rev. (to be published).

10. M. Rodot, H. Rodot, and R. Triboulet, J. Appl. Phys. 32, 2254 (1961).

11. See for example, E.H. Putley, The Hall Effect and Related Phenomena (Butterworths, London, 1960), Chap. III.

12. A.J. Strauss, T.C. Harman, J.G. Mavroides, D.H. Dickey, and M.S. Dresselhaus, Proceedings of the International Conference on the Physics of Semiconductors, Exeter (1962), p. 703.

13. T.C. Harman and W.H. Kleiner, Bull. Am. Phys. Soc. 8, 206 (1963).

14. T.C. Harman, J.M. Honig, and B.M. Tarmy, Proceedings of the International Conference on the Physics of Semiconductors, Paris (1964) (in press).

15. T.C. Harman, J.M. Honig, and B.M. Tarmy, Advanced Energy Conversion (to be published).

16. R. Fieschi, Physica 24, 972 (1957).

17. C.S. Smith, Solid State Physics 6, 175 (1958).

V. MAGNETISM AND RESONANCE

A. THEORY

1. Aspherical Spin-Density in S-State Cations

The following is the abstract of an article that has been submitted to the Physical Review:

"A calculation of the first-order effect of spin-orbit coupling on a $(3d)^5$ unperturbed S-state ion in a cubic crystal field has led to a new contribution $\sigma_1(r)$ to the ionic spin-density. The integral over space of $\sigma_1(r)$ is zero and $\sigma_1(r)$ is perpendicular to the unperturbed spin-density $\sigma_0(r)$; while $\sigma_0(r)$ is spherically symmetric about the nucleus, $\sigma_1(r)$ is highly aspherical. In α-Fe_2O_3 at room temperature, the spin-density consists of the large "antiferromagnetic" component σ_0, the new term σ_1, plus the weak ferromagnetic or Dzialoshinsky term σ_D, which is spherical. In neutron scattering, it is found that σ_1 contributes to the same "ferromagnetic" Bragg peaks as does σ_D, and in the same order of magnitude. Hence the new term is probably important for understanding the surprising, highly aspherical ferromagnetic spin-density distribution recently observed in α-Fe_2O_3 by Pickart, Nathans and Halperin. In general, $\sigma_1(r)$ will be non-zero under much less restrictive symmetry requirements than those needed for nonvanishing of σ_D."

In the course of discussion, it is pointed out that the Dzialoshinsky-Moriya theory of the weak ferromagnetism in α-Fe_2O_3, for example, implies that the application of a spatially uniform magnetic field should influence the distribution of domains of antiferromagnetic spin-components. This effect was observed by Pickart, et al.

T. A. Kaplan

2. Sinusoidal Magnetostriction in Rare-Earth Metals

From a simple theory, based on a direct-exchange magnetostriction, it follows that there should be a sinusoidal variation in the c-axis spacing in thulium and in the high-temperature phase of erbium. The period of the distortion is exactly half that of the magnetic structure and should result in the appearance of superstructure lines in the x-ray diffraction patterns of these crystals at low temperatures. A calculation of the magnitude of this distortion, based on the Ruderman-Kittel-Kasuya-Yoshida (RKKY) superexchange interaction,[1-4] indicates that the x-ray superstructure should be observable in single crystals.

The high-temperature phases of erbium and thulium possess sinusoidally modulated spin structures given by[5-7]

$$\vec{S}_m = \vec{S} \cos \vec{Q} \cdot \vec{R}_m \quad , \tag{1}$$

where $\vec{Q}$ is a vector directed along the c-axis of the crystal, and the spin $\vec{S}$ also points along

the c-axis. The Heisenberg exchange energy, including magnetostriction is given, to first order in the atomic displacements $\Delta \vec{R}_n$, by $H_s = H_s^o + H_{me}$, where

$$H_s^o = -NS^2 \sum_{\vec{K}} J(\vec{K} + \vec{Q}) \; F(\vec{K}) + S^2 \sum_{\vec{q}} J(\vec{q}) \tag{2}$$

is the magnetic energy of the undistorted lattice[4] and

$$H_{me} = NS^2 \; \vec{\epsilon} \cdot \sum_{\vec{K}} (\vec{K} + \vec{Q}) \; J(\vec{K} + \vec{Q}) \; F(\vec{K}) \tag{3}$$

is the magneto-elastic energy [$\vec{K}$ is a reciprocal lattice vector, N is the number of unit cells in the crystal, $F(\vec{K})$ is the structure factor for the hexagonal close packed lattice, and $J(\vec{q})$ is the Fourier transform of the exchange interaction]. The atomic displacements are given by

$$\Delta R_n = \vec{\epsilon} \; \sin(2\vec{Q} \cdot \vec{R}_n) \quad , \tag{4}$$

where $\vec{\epsilon}$ is parallel to the c-axis. The magneto-elastic energy H_{me} must be balanced against the elastic energy of the crystal given by

$$\Phi = \frac{1}{2} \; Nm \; \omega_{2\vec{Q}}^2 \; \epsilon^2 \quad , \tag{5}$$

where m is the nuclear mass of the rare-earth atom and $\omega_{2\vec{Q}}^2$ is the angular frequency of the elastic mode of the wave vector $2\vec{Q}$. The equilibrium value of ϵ, given by $\partial \Phi / \partial \epsilon + \partial H_{me} / \partial \epsilon = 0$, is

$$\vec{\epsilon} = -\frac{S^2}{m\omega_{2Q}^2} \sum_{\vec{K}} (\vec{K} + \vec{Q}) \; J(\vec{K} + \vec{Q}) \; F(\vec{K}) \quad . \tag{6}$$

The sum in Eq. (6) was evaluated on an IBM 7094 computer using the RKKY form for $J(\vec{K} + \vec{Q})$ and the values of the various parameters given by Yoshida and Watabe.[4] The result is

$$\epsilon \simeq 1.6 \times 10^{15} \; cm/sec^2 \cdot \frac{S^2}{\omega_{2\vec{Q}}^2} \quad . \tag{7}$$

In erbium, ω_{2Q} is in the "optical" phonon branch near the hexagonal Brillouin zone edge. We can estimate ω_{2Q} from Debye temperature Θ_{Er} and from $\omega_{2Q}(Er) \simeq \omega_{2Q}(A\ell) \; \Theta_{Er}/\Theta_{A\ell}$, where $\omega_{2Q}(A\ell)$ is known from neutron diffraction.[8] These estimates give $\omega_{2Q} \simeq 1.5 \times 10^{13} \; sec^{-1}$. This results in an estimate for the displacement of

$$\epsilon \simeq 1.6 \times 10^{-11} \; cm \simeq 3 \times 10^{-4} \; c \tag{8}$$

for $S = 3/2$, where c is the length of the unit cell along the hexagonal axis ($c = 6 \times 10^{-8} \; cm$). The resultant sinusoidal magnetocrystalline distortion, Eq. (4), with an amplitude given by Eq. (8), should be observable in single crystals. A comparable distortion of the same form is

predicted also for thulium, although other modes should be present as well, because the spin structure in this material becomes a square wave at low temperatures.

J. O. Dimmock

3. Transition-Metal Oxides with Metallic Conductivity

Examination of the oxide bronzes leads to the conclusion that frequently transition-metal oxides cannot be considered ionic even in zero-order approximation. Since the electronegativity differences between oxygen and the transition elements are large, the broad bands are separated by a large energy gap and the conduction electrons are not broad-band electrons. Consider the schematic energy diagrams for ReO_3, which are shown in Fig. V-1(a-b). In the ReO_3 structure, the cations are in octahedral anion interstices and form a simple-cubic array, neighboring cation octahedra sharing common corners. The crystalline-field splittings are indicated for the separate ions. The difference between the Madelung energy and ionization energies, $E_M - E_I$, depends upon the magnitude of the effective charges at cation and anion. Figure V-1(a) corresponds to the conventional molecular-orbital (MO) energy scheme for ionic crystals, in which the cation d orbitals are localized and, in zero approximation, are the atomic orbitals. Figure V-1(b) corresponds to sufficient covalence via both σ- and π-electrons that neither those d-electrons with e_g symmetry nor those with t_{2g} symmetry can be assumed localized in zero approximation, but are mixed with anion (sp_σ) and p_π^2 orbitals to form collective-electron, bonding and antibonding bands. Since the magnetic and electrical properties due to cationic d-electrons will be quite different for the two cases, it is important to know under what conditions collective-electron vs localized-electron behavior can be expected. It is clear that collective-electron behavior is favored the more covalent the bonding. Therefore, the existence of collective-electron π-electrons implies collective-electron σ-states, although not necessarily vice versa. Moreover, the existence of collective-electron states in oxides implies collective-electron states in isoelectronic and isostructural sulfides, selenides, and tellurides, although not necessarily vice versa.

These considerations lead to a threefold classification of transition-metal oxides with metallic conductivity.

Class I: The cationic d orbitals are localized to the cation sublattice, in zero approximation, but the cation-cation separation is $R < R_c$, where R_c is the critical separation for a collective-electron vs a localized-electron description for the cation-sublattice electrons. This would be illustrated by the hypothetical case of a purely ionic ReO_3 having sufficient overlap of the Re 5d orbitals with t_{2g} symmetry across the cube faces that the t_{2g} levels of Fig. V-1(a) are broadened into a narrow band. This type of band formation occurs in some oxides having cations in octahedra that share common edges or faces.

Class II: The cationic d orbitals mix with the anionic states to form partially filled antibonding π^* states. This is illustrated in Fig. V-1(b), which appears to correspond to the actual situation in ReO_3 (see Sec. V-B-5). The metallic properties of Na_xWO_3 are readily interpreted in this same way.[13]

3-SS-3411
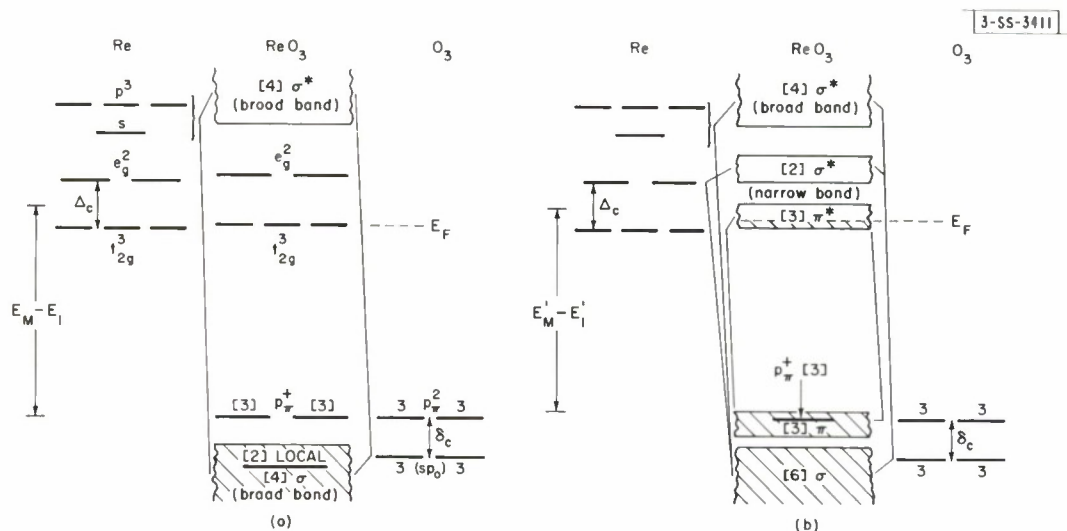
Fig. V-1. Possible one-electron energy-level schemes for ReO_3. (a) Ionic model having localized cationic levels of e_g and t_{2g} symmetry. (b) Covalent model having collective electron σ-bond and π-bond states. Spin degeneracy not shown and $(E_M' - E_I') < (E_M - E_I)$. Ionic model valid if ReO_3 a semiconductor and magnetic susceptibility obeys a Curie-Weiss law. Covalent model valid if ReO_3 is metallic and Pauli paramagnetic.

3-SS-3412
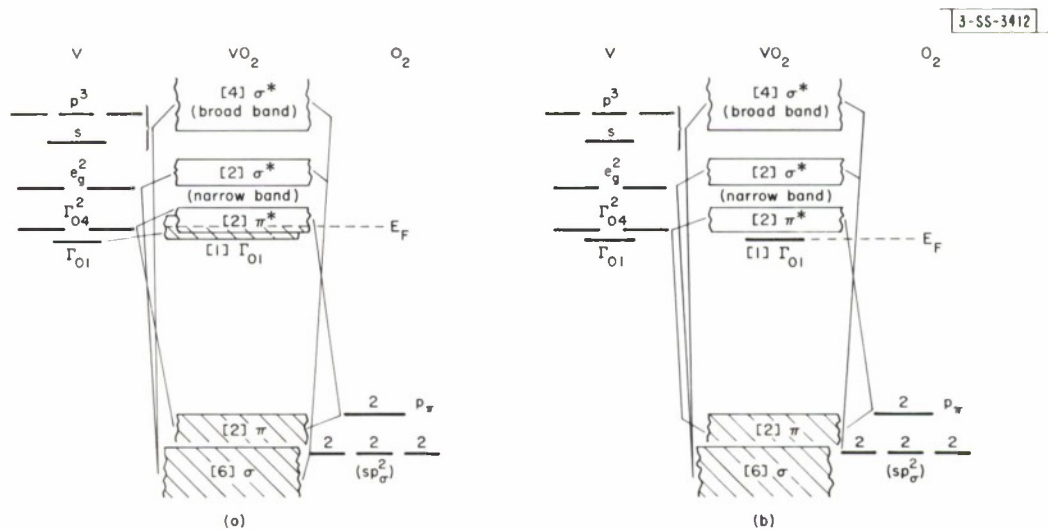
Fig. V-2. Possible one-electron energy-level schemes for VO_2. (a) Covalent model with $R < R_c$ along c-axis. (b) Covalent model with $R > R_c$ along c-axis. (If V^{4+}-V^{4+} pairs form, as in low-temperature VO_2, the Γ_{01} level corresponds to a homopolar-bond state rather than a localized Γ_{01} level of unpaired spin.) With two molecules per unit cell, π^* bond may be split in two. Spin degeneracy is not shown.

Class III: The cationic d orbitals mix with the anionic states to form partially filled, antibonding σ^* states. We believe that this may be illustrated by some oxides, which are under investigation; that it will manifest itself in many sulfides, selenides, and tellurides.

Slightly reduced rutile is particularly interesting because it illustrates simultaneously both Class I and Class II. In this structure, each oxygen ion has three, coplanar near-neighbor cations. Therefore, one p_π orbital is available for π bonding. Along the c-axis cation octahedra share common edges. Figure V-2(a) corresponds to $R < R_c$ along the c-axis, which is exemplified by TiO_2 and high-temperature VO_2; Fig. V-2(b) corresponds to $R > R_c$, which is found in CrO_2. In TiO_2, the Fermi level E_F falls between the filled π band and an empty Γ_{01} and π^* band. If electrons are photoexcited in pure TiO_2 from the top of the π band to the bottom of the Γ_{01} band, the electrical conductivity exhibits an anisotropy of 10^4 to 1 favoring the c-axis. However, as many electrons are excited, the conductivity becomes nearly isotropic, presumably because the π^* band is also partially occupied. It is for this reason that the two conduction bands (a cation-cation Γ_{01} and a π^*) overlap as shown in Fig. V-2(a).

Vanadium dioxide exhibits a semiconducting $\rightleftarrows$ metallic transition at low temperatures as a result of the formation of isolated V^{4+}-V^{4+} homopolar bonds along the c-axis. The energy diagram for distorted, low-temperature VO_2 would be similar to Fig. V-2(b), but the Γ_{01} level now represents a homopolar-bond state rather than a localized state. Molybdenum dioxide also has the low-temperature VO_2 structure, but it is a metal with nearly isotropic conductivity. This is consistent with Fig. V-2(b) since the one more electron per molecule in MoO_2 raises E_F into the π^* band.

Nonstoichiometric chromium dioxide is metallic and ferromagnetic. It is discussed elsewhere in this report, where the exchange splitting, which removes the spin degeneracy of the levels shown in Fig. V-2(b), is also included.

                                                                        J. B. Goodenough

4. Combined Valence-Bond Plus Molecular-Orbital Method for Many-Electron Systems

The abstract of a thesis of this title for the Department of Chemistry, M.I.T., reads as follows:

> "This thesis addresses itself to the problem of obtaining ground-state approximate wave functions and energies for cyclic systems formed by $4M + 2$ one-electron atoms, and systems whose wave functions can be approximated in such a manner (notably, the benzene molecule). One of the methods developed appears to be capable of being extended to infinite three-dimensional lattices of one-electron atoms.

> "The author first develops a method which involves the configuration-interaction of the ground-state MO function with a peculiar Valence-Bond function. This method leads to energy values, for the hexagonal ring of hydrogen atoms, which compare favorably with those of the full configuration-interaction of Mattheiss.[9] The energy values are lower than those reported by Moskowitz[10] for the delocalized Alternant-Molecular-Orbital method at all lattice spacings given, except $D = 2$, and arguments are presented to show

that Moskowitz's energy-value must be in error at this lattice-spacing. However, the new method does not appear to be extendable to systems larger than the eighteen-atom ring.

"Then the author outlines another method which may be described as a "localized alternant-molecular-orbital" method. This method is much easier to implement and leads to energy values which are even better than those of the first new method, at all but very large values of the lattice spacing. Furthermore, this second new method appears to be capable of extension to rings of arbitrarily large M. Extension even to infinite three-dimensional lattices appears to be practicable.

"Explicit energy formulas for both new methods are given (in terms of the distinct one-electron and two-electron integrals among the orthogonalized atomic orbitals) for the hexagonal ring of one-electron atoms."

E. G. Larson

B. EXPERIMENT

1. Magnetic Structure of $MnCr_2S_4$

We have completed a neutron-diffraction study of two powdered samples of $MnCr_2S_4$, which we find to be a normal cubic spinel with a cell edge of about $10.115 \overset{\circ}{A}$. Both samples were prepared by A. Wold (Brown University) from the reaction of H_2S with $MnCr_2O_4$. One sample contains some of the chromite as an impurity because of insufficient reaction, whereas the other contains some MnS and Cr_3S_4 impurities because of excessive heating. However, these impurity contributions to the neutron diffraction patterns are distinct from the pattern attributable to the manganese thio-chromite, and consequently they neither constitute a serious problem, nor do they detract from the reliability of the results presented below.

The combined results obtained with our two samples are presented in Table V-1. The second column gives the intensities (in total number of neutrons counted for a fixed monitor count) of the nuclear peaks, as observed at room temperature but corrected by means of the Debye-Waller factor. As can be seen from a comparison of these numbers with those given in the next column, the experimental values are in good agreement with those calculated on the basis of a normal spinel with an "oxygen" u-parameter of 0.3876. It is interesting to note that this u-parameter is not much smaller than the value of 0.3892 observed in $MnCr_2O_4$ despite the large expansion of the unit cell.

The total intensity at 4.2°K is comprised of both nuclear and magnetic contributions. Our experimental findings are given in the fourth column, and they agree well with the theoretical values listed in the next column. These theoretical intensities were obtained by adding the magnetic contributions computed for a Néel configuration with respective A- and B-site moments of 4.7 and $3.0 \mu_B$ to the nuclear values given in the third column. The experimental form factor for manganese and the Watson-Freeman theoretical form factor for chromium were used in this calculation. These assignments of magnetic moments also agree with our observation of a spontaneous magnetization of $1.3 \mu_B$ in this material.

	TABLE V-1			
	INTEGRATED NEUTRON DIFFRACTION PEAK INTENSITIES FOR $MnCr_2S_4$			
(h k l)	Nucleor Intensity		Total Intensity (Nuclear and Magnetic)	
	Experimentol[*]	Theoreticol[†]	Experimentol[‡]	Theoreticol[§]
111	6089	6100	23251	23182
200	0	0	0	0
220	774	708	4462	4609
113	0	24	0	42
222	356	388	2775	2699
400	7326	7266	10652	10571
331	809	865	Observed[¶]	4205
420	0	0	0	0
422	660	655	Observed[¶]	1785
333-115	716	698	617	704
440	2997	3021	3094	3040

[*] Deduced from measurements at 300°K by the opplicotian of the Debye–Waller correction factor determined from o leost-squores fit ta the doto.

[†] Computed on the basis of a scottering omplitude of 0.28×10^{-12} cm far the sulfur, on "axygen" u-parameter of 0.38755, and perfect normality.

[‡] Meosured ot 4.2°K.

[§] The mognetic contributian wos computed on the basis of a collinear, Néel spin configurotian, with the ossignments of 4.7 μ_B to the Mn^{++} ions and 3.0 μ_B to the Cr^{+++} ions.

[¶] These peaks were overlapped by peoks arising from the aluminum somple halder.

The departure of the manganese moment from its spin-only value of $5\,\mu_B$ cannot be attributed to any canting of the A-site moments, since such a spin configuration would have given rise to an experimental intensity of 640 counts for the 200 peak, in contradiction with our findings. In addition, S. Foner (National Magnet Laboratory, M.I.T.) has examined part of our sample in magnetic fields up to 50 koe and has found no evidence of any high-field susceptibility, such as would be characteristic of spin canting. Thus, our assumption of a Néel spin configuration is confirmed, and we can unequivocally conclude that divalent manganese ions on the tetrahedral A-sites in $MnCr_2S_4$ possess magnetic moments of $4.7\,\mu_B$ and cannot be in a pure $^6S_{5/2}$ electronic state.

<div style="text-align:right">

K. Dwight
N. Menyuk

</div>

2.   ESR in $CoCr_2O_4$

Further spin resonance measurements on the spinel $CoCr_2O_4$, which has a complex spiral-spin configuration, have been made to study the static-magnetic-field dependence of the resonant modes upon temperature and excitation frequency. The resonant mode associated with the higher temperature region (Region 3, see the last Solid State Research Report[†]) was observed at 317 kMcps, the magnetic field for resonance decreasing from approximately 20 koe to several kilo-oersteds in the temperature range from 67 to 50°K. Thus, at higher frequencies, a resonance mode associated with region 3 has been observed to extrapolate smoothly to region 2, to as low in temperature as 50°K (see Fig. V-3).

The weaker resonances previously reported and believed associated with the uniform precession mode were found to be instrumental effects; they disappeared when the detection system was properly shielded.

<div style="text-align:right">

J. J. Stickler
H. J. Zeiger

</div>

3.   Spin-Wave Resonance at Millimeter Wavelengths

The amount and accuracy of the information obtainable from the interpretation of spin-wave resonance measurements depend on the number of measurable spin-wave peaks which are excited in the useful magnetic field interval between the main ferromagnetic peak and the saturation magnetization value of the sample. Since the extent of this interval is almost directly proportional to the frequency of the microwave excitation and since the separation between adjacent spin-wave peaks is independent of the frequency of excitation, it is desirable to use microwave excitation of as short a wavelength as possible.

The spin-wave resonance techniques have been extended from 10 to 70 Gcps (a wavelength of 4 mm). At the higher frequency, the useful magnetic field interval for a given film sample is approximately seven times larger than at the lower frequency. For an 80% Ni-20% Fe film (80-20 Permalloy), for example, the interval is approximately 27 koe at 70 Gcps.

To date, well-resolved spin-wave spectra have been observed in 80-20, 70-30, and 65-35 vacuum-evaporated Permalloy films of approximately 1000-Å thickness. These spectra have indicated that the values of the effective magnetizations and the effective g-values are in essential agreement with those for the corresponding bulk materials.
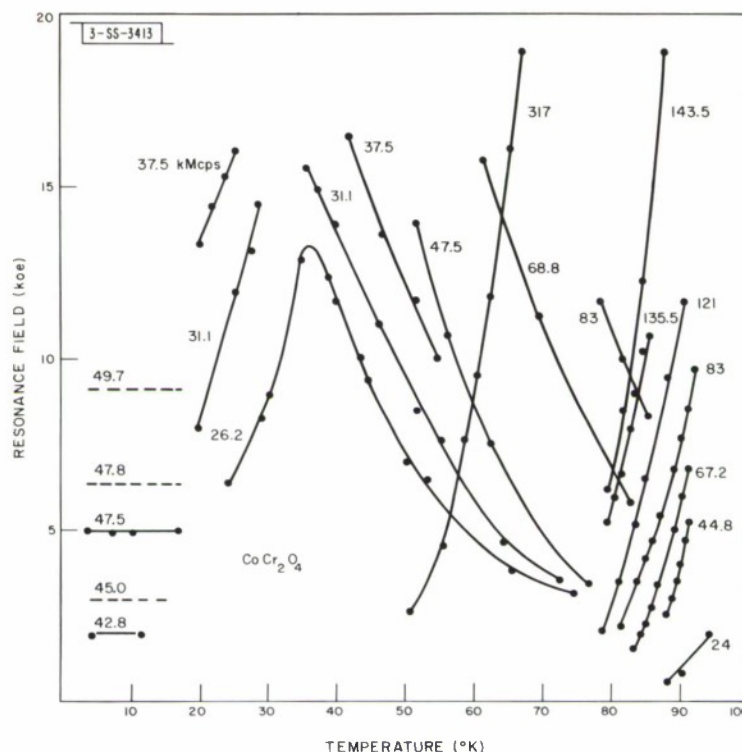
---

† 1964:1, p. 48. DDC 601830.

Fig. V-3. Field for resonance in "modified exchonge mode" of $CoCr_2O_4$ os o function of temperature, ot o number of microwove frequencies.

We plan to prepare a series of Ni-Fe films of varying composition (from 100 percent Ni to 100 percent Fe) to allow the determination of the exchange constant and the spin-wave dispersion law as a function of composition and temperature. The accuracy gained by the increase in the number of measurable peaks, in addition to the shorter spin-wave wavelengths which are available, may make it possible to measure, for the first time, the quartic term in the dispersion relation and long-range exchange interactions.

Again, because of the accuracy gained by the increase in the number of measurable peaks, and because the wide useful-magnetic-field interval available provides a correspondingly wider variation in k-number, it may be possible to detect the effects of spin-wave-phonon coupling on the dispersion law by having the crossover region (coincidence of ω and k for phonons and spin waves) fall within the observable spectra of a series of films of varying compositions.

R. Weber
P. E. Tannenwald
J. W. Burke

4. Compounds with B31 $\rightleftarrows$ B8$_1$ Transitions

Manganese arsenide exhibits a temperature interval between 315 and 403 °K over which the crystallographic structure is slightly distorted from the hexagonal B8$_1$ symmetry of NiAs to the orthorhombic B31 symmetry of MnP. The B8$_1$ $\rightleftarrows$ B31 transition at 315°K is first-order and
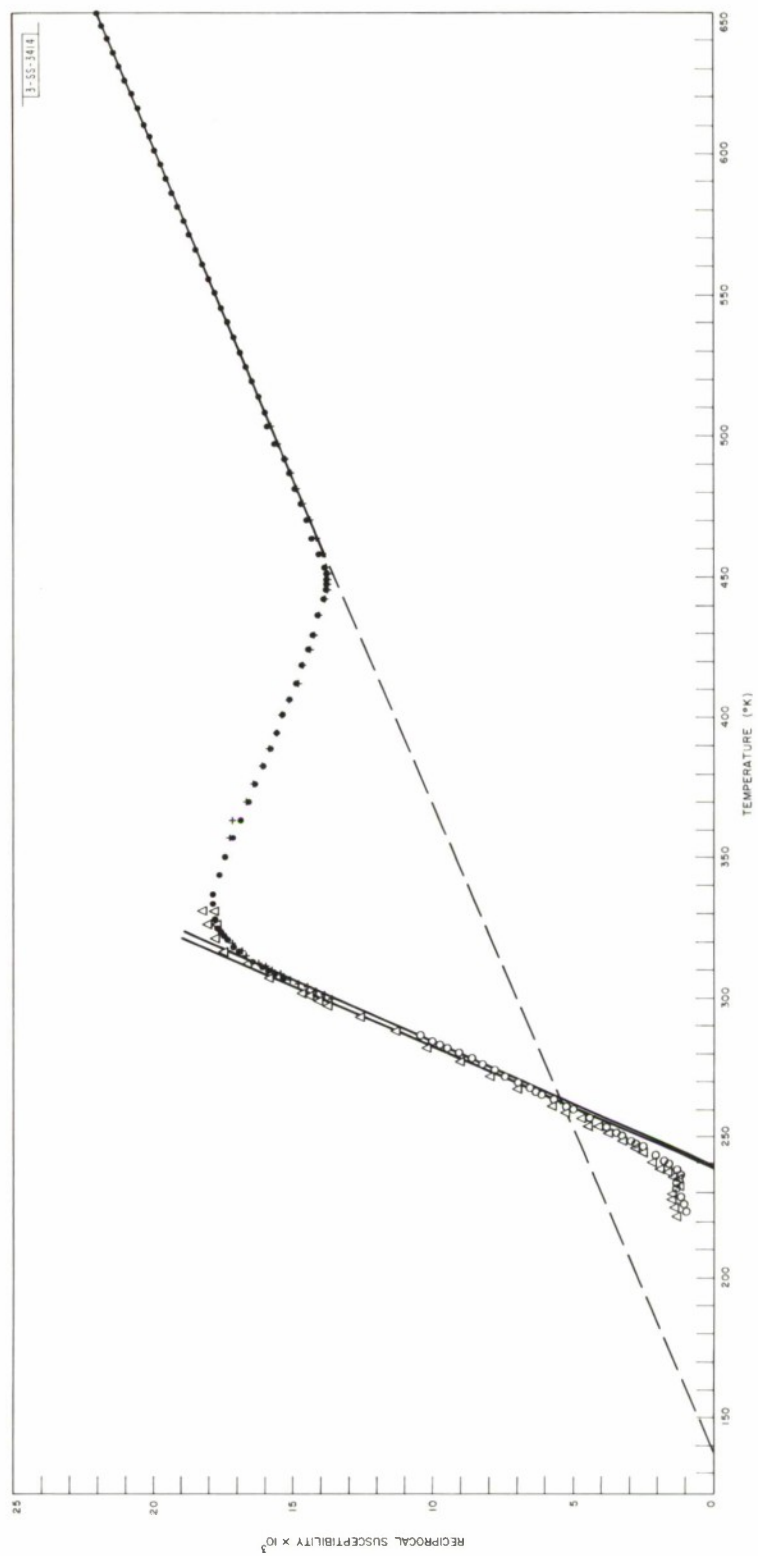
Fig. V-4. Paramagnetic susceptibility of MnAs$_{0.90}$P$_{0.10}$.

corresponds to a ferromagnetic Curie temperature T_c. The B31 $\rightleftarrows$ B8$_1$ transition at 403°K may be second order. Although the magnetic susceptibility exhibits a pronounced maximum at 403°K, there is no evidence of antiferromagnetic ordering below this temperature. In order to investigate whether the occurrence of the B31 phase signals the onset of spin quenching with decreasing temperature, we have initiated a crystallographic and magnetic study of the systems $MnAs_{1-x}P_x$ and $MnAs_{1-y}Sb_y$. The crystallographic data, which show a predicted decrease in the B31 temperature interval with increasing y, but an increase in the interval with increasing x, were presented in the last Solid State Research report. For x > 0.04, the B31 phase is stable to lowest temperatures. We restrict ourselves here to a discussion of the paramagnetic susceptibility of a sample with x = 0.1, which is shown in Fig. V-4.

The B31 $\rightleftarrows$ B8$_1$ transition occurs at 449°K, and above 460°K the χ_m^{-1} vs T curve is a good straight line having a Curie constant $C_{mole} = 2.93$, corresponding to a $\mu_{eff} = 4.84\,\mu_B$ per manganese, or to a manganese spin S = 1.97, which is close to a theoretical S = 2.0 for a high-spin-state Mn^{3+} ion.

In order to determine the extent of the apparent spin quenching between 330° and 460°K, where χ_m^{-1} vs T has a <u>positive</u> slope, two estimates are possible. First, between 330°K and the Curie temperature of about 230°K, χ_m^{-1} vs T exhibits a short linear region with negative slope corresponding to $C_{mole} = 0.550$, or a $\mu_{eff} = 2.10\,\mu_B$ per manganese and an S = 0.62. This value for the manganese spin corresponds closely to an S = 0.65 found from the saturation magnetization of orthorhombic (B31) MnP. Second, extrapolation of the high-temperature (T > 460°K) susceptibility χ_1 to the low-temperature interval 240°K < T < 330°K via a Curie-Weiss law with Curie constant C, gives for a susceptibility χ_2 in the low-temperature interval: $C_2 = C_1(1/\chi_1)/(1/\chi_2) - \chi_2(\Theta_2 - \Theta_1)$, where the paramagnetic Curie temperatures are obtained from extrapolation of the straight-line portions of the curves as $\Theta_1 = 137$°K and $\Theta_2 \approx 240$°K. This method gives a low-temperature spin of S ≈ 0.7. These estimates are self-consistent and strongly support the suggestion that the interval of positive slope in χ_m^{-1} vs T, which occurs over a temperature interval $\Delta T > 100$°C below the B31 $\rightleftarrows$ B8$_1$ transition, reflects spin quenching from high-spin manganese ($\mu_{Mn} \sim 4\,\mu_B$) to low-spin manganese ($\mu_{Mn} \sim 2\,\mu_B$).

D. H. Ridgley
W. A. Newman
J. B. Goodenough

5. Electrical Conductivity of ReO_3 and $SrMg_{0.5}Re_{0.5}O_3$

The metallic conductivity of the bronze system Na_xWO_3 has been shown to be due to <u>x</u> < 1.0 electrons per molecule in a partially filled band of collective-electron states. Three proposals for the origin of this conduction band have been made:

(a) Model I: Na-Na bonding via direct overlap of sodium 3p orbitals,[11]

(b) Model II: W-W bonding via direct overlap of tungsten t_{2g} orbitals,[12]

(c) Model III: Covalent π bonding via mixing of tungsten t_{2g} and oxygen p_π orbitals.[13]

In order to discriminate experimentally between these three proposals, the electrical conductivities of ReO_3 and $SrMg_{0.5}Re_{0.5}O_3$ have been investigated.

Na_xWO_3 has the cubic perovskite structure of Fig. V-5, but with only x of the cation A-sites randomly occupied by sodium atoms. Cubic ReO_3 has no cations in the A-positions and Re^{6+}, like W^{5+}, has a $5d^1$ configuration. According to Model I, ReO_3 should be a semiconductor (or insulator if stoichiometric). Since the radial extensions of the 5d orbitals of tungsten and rhenium are similar, metallic conductivity is anticipated from Model II. Since covalent bonding will be as strong or stronger for the cation of higher formal charge, metallic conductivity is also predicted from Model III. Therefore, if ReO_3 is metallic, an additional experiment is required to distinguish between Models II and III. In the perovskite $SrMg_{0.5}Re_{0.5}O_3$ the Mg^{2+} and Re^{6+} ions order[14] on the B-sites to form two interpenetrating, f.c.c. sublattices. In such a structure there would be no interference of Re^{6+}-$Re^{6+}t_{2g}$ overlap across the cube faces, so that metallic properties are anticipated from Model II. On the other hand, the formation of collective-electron π and π^* band states requires Re^{6+} on each side of an oxygen ion, which does not occur. Therefore, from Model III, $SrMg_{0.5}Re_{0.5}O_3$ is expected to be a semiconductor or insulator. Since reliable data for these materials do not exist, an experimental investigation of their electrical properties has been initiated.
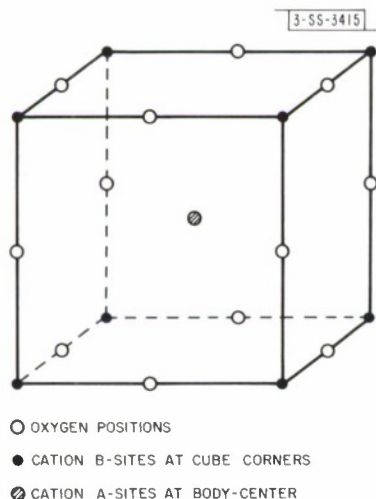

Fig. V-5. The structure of cubic perovskite. For ReO_3 only the cation B-sublattice is occupied. For cubic Na_xWO_3 the B-sublattice is filled with W, and x of the A-sites are randomly occupied by Na.

O OXYGEN POSITIONS
● CATION B-SITES AT CUBE CORNERS
⊘ CATION A-SITES AT BODY-CENTER

Considerable difficulty was experienced in the preparation of stoichiometric ReO_3. There are two reportedly dependable methods of preparation involving the reduction of rhenium heptoxide by dioxane[15,16] or by carbon monoxide.[15] These authors determined their product purity through analyses for total rhenium. A more direct measure of cation oxidation state is the determination of total reducing power in the product. When the method of Wickham and Whipple[17] for total reducing power was applied to several products obtained via the dioxane process, results were obtained which were too high by several percent. Somewhat better products resulted from reduction with CO. However, in this method, equilibrium is difficult to achieve and there was a tendency for the products to be low in reducing power. Similar results have been indicated by King and Cobble.[18] Since all products possessed the characteristic bright-red color of ReO_3, and since they all appeared to be single phase by x-ray diffraction, it would seem that a considerable range of stoichiometry is possible for this material. One reduction attempt, via the CO

process in which reaction conditions were carefully maintained for a period of four weeks, gave a sintered product having 100.0 percent of its theoretical reducing power. From this product a bar was cut for conductivity measurements.

The ordered perovskite $SrMg_{0.5}Re_{0.5}O_3$ was easily prepared by the reaction

$$3SrCl_2 + 6KReO_4 + Re + 11SrO + 7MgO \xrightarrow[\text{in vacuo}]{900°C} 6KCl + 14SrMg_{0.5}Re_{0.5}O_3 \quad .$$
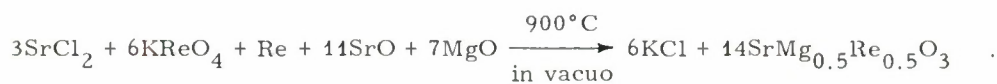
After leaching with water to remove the potassium chloride, the product was pressed into the form of a bar, sealed in an evacuated silica tube, and sintered at 900°C.

Conductivity measurements were made with alternating current in order to avoid contact resistance and grain boundary effects. Resistivity at each temperature was checked with variable frequencies between 0.2 and 20 kcps. No frequency dependence was noted. The conductivity of ReO_3 was found to have a negative temperature dependence characteristic of metals with a room temperature resistivity of 3×10^{-2} ohm-cm. However, $SrMg_{0.5}Re_{0.5}O_3$ appears to be a semiconductor with an activation energy of 0.31 ev and a resistivity at room temperature of $\sim 10^5$ ohm-cm. It is therefore concluded that Model III gives the most appropriate description of transition-metal oxides, with perovskite or ReO_3 structures, that exhibit metallic conductivity. This includes the tungsten bronzes.

<div align="right">
A. Ferretti
D. B. Rogers
J. B. Goodenough
</div>

6. Single-Crystal Growth of Vanadium Spinels by Electrolytic Reduction

In the previous Solid State Research Report, initial results of our program of crystal growth of vanadium spinels by electrolytic reduction from fluxes were given. It was pointed out that reduction of pentavalent vanadium in the presence of Co^{+2} leads to the precipitation of $Co_{1+x}V_{2-x}O_4 (0 \leqslant x \leqslant 1)$ from fluxes of $Na_2WO_4 - WO_3$. The value of x is dependent on a number of factors including the initial ratio of the Lewis base Na_2WO_4 to the Lewis acid WO_3, the temperature at which electrolysis is conducted, and the initial concentration of Co^{+2} and V^{+5}. Under conditions of inert atmosphere and low current density, it is possible to effect crystal growth of several compositions in the "mixed" spinel system. Work on this system has continued and our results are summarized in Table V-2.

Initially, product precipitation was obtained on cathodes consisting of platinum gauze, which resulted in a maximum crystal size of about 3 to 4 mm. More recent experiments have utilized cathodes consisting of crystals from previous experiments. These act as seeds from whose octahedral faces it has been possible to grow new crystals up to a centimeter in diameter. Figure V-6 shows two such crystals grown from the same seed. These crystals have the approximate composition $Co_{1.29}V^{+3}_{1.42}V^{+4}_{0.29}O_4$.

<div align="right">
D. B. Rogers
A. Ferretti
E. J. Delaney
</div>

7. Effect of Mn^{+3} on Cation Ordering in Lithium Spinels

Octahedrally coordinated Mn^{+3} and Cu^{+2} are Jahn-Teller ions that are known to produce unique effects. In the spinel lattice tetragonal distortions are induced at sufficiently high B-site

| TABLE V-2				
EXPERIMENTAL CONDITIONS FOR GROWTH OF VANADIUM SPINELS BY FUSED SALT ELECTROLYSIS				
Initial Flux Composition	Current Density (ma/cm^2)	Temperature $(^\circ C)$	Duration of Electrolysis (Days)	Approximate Product Composition
$1CoO:1V_2O_5:0.72WO_3:3.28Na_2WO_4$	~130	800	3	$Co_{1.54}V_{1.46}O_4$
$1CoO:1V_2O_5:0.4WO_3:3.6Na_2WO_4$	~20	900	10	$Co_{1.38}V_{1.62}O_4$
$1CoO:1V_2O_5:0.2WO_3:3.8Na_2WO_4$	~100	900	1	$Co_{1.22}V_{1.78}O_4$
	~10	900	7	
$1CoO:1V_2O_5:Na_2WO_4$	~15	900	10	$Co_{1.11}V_{1.89}O_4$
$1CoO:1V_2O_5:1.2WO_5:2.8Na_2WO_4$	~10	960	7	$Co_{1.29}V_{1.71}O_4$
$1.7CoO:1.7V_2O_5:4Na_2WO_4$	~20	920	10	$Co_{1.56}V_{1.44}O_4$
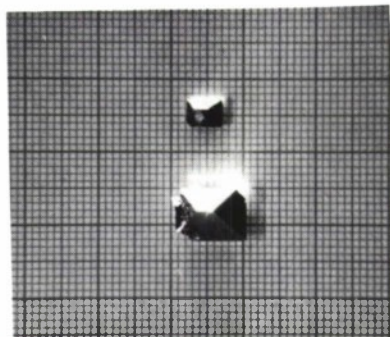
Fig. V-6. Single crystals of $Co_{1.29}V_{1.71}O_4$ grown from the some cathode seed by fused salt electrolysis.

concentrations of these ions.[19,20] In certain ferrite memory-core materials, one method of obtaining maximum B-H loop squareness is the substitution of Mn^{+3} or Cu^{+2} on about 20 to 25 percent of the occupied octahedral sites.[21,22] Although the concentration of these ions is much too small to induce long-range cooperative distortion of the lattice, the latter effect may be indicative of a tendency for the Jahn-Teller ions to form small clusters in an apparently homogeneous material. Such clusters have never been observed.

In general, spinels of the type $M^{+3}[Li_{0.5}M^{+3}_{1.5}]O_4$ (where M^{+3} is not a Jahn-Teller ion) are found to possess primitive cubic symmetry which indicates an ordering of the lithium ions on the occupied octahedral sites. The ordering energy in such spinels has been estimated[23] to be about 119 kcal/mole. If a tendency exists for Jahn-Teller ions to cluster in a spinel host and if the energy gain for such clustering is sufficiently high, it would appear reasonable that Mn^{+3} substitutions of the type $M^{+3}[Li_{0.5}M^{+3}_{1.5-x}Mn^{+3}_x]O_4$ might destroy long-range octahedral order at a value of $\underline{x}$ less than that required for cooperative tetragonal distortions of the lattice. In the previous Solid State Research report, preliminary evidence was given which indicated that no ordering of lithium is observed in the spinel system $Li_{0.5}Ga_{2.5-x}Mn_xO_4$ when $x \gtrsim 0.3$ and that Mn^{+3} appears to be unique among the trivalent ions investigated in its ability to destroy this order. At present, our investigation of this phenomenon in the system $Li_{0.5}Ga_{2.5-x}Mn^{+3}_xO_4$ and $Li_{0.5}Fe_{2.5-x}Mn^{+3}_xO_4$ is near completion. Crystallographic data for these systems are summarized in Table V-3 and the lattice parameters are shown as a function of composition in Fig. V-7. Since volatility of lithium is usually a problem in the synthesis of lithium spinels, all members of the gallate series and some of the ferrites were spectrographically analyzed for total lithium. In all cases, the lithium content was within 3 percent of the theoretical value.

The data of Table V-3 indicate that only 13 to 15% Mn^{+3} on the spinel octahedral sites is sufficient to destroy lithium ordering in the systems studied. It is also apparent from Fig. V-7 that the loss of order is accompanied by an anomalous increase in the lattice parameters in both systems. This increase presumably reflects the decrease of electrostatic binding energy associated with disordering. An estimate of this decrease, based on a purely ionic model[23] that neglects changes in Born repulsion terms as well as short-range ordering, gives ~147 kcal/mole. Although the actual decrease in binding energy is considerably lower, it is still larger than can be accounted for by entropy alone. Since there must be a total gain in lattice energy for the disordered vs ordered states given $x > 0.3$, it is evident that there must be an energy compensation that is uniquely associated with the Mn^{+3} as against other trivalent ions. A reasonable possibility

TABLE V-3		
CRYSTALLOGRAPHIC PROPERTIES OF THE SPINEL SYSTEMS		
$Li_{0.5}Ga_{2.5-x}Mn_x^{+3}O_4$ AND $Li_{0.5}Fe_{2.5-x}Mn_x^{+3}O_4$		
Composition	Lattice Parameter (Å)	Octahedral-Site Order
$Li_{0.5}Ga_{2.5}O_4$	8.203	Present
$Li_{0.5}Ga_{2.4}Mn_{0.1}O_4$	8.204	Present
$Li_{0.5}Ga_{2.35}Mn_{0.15}O_4$	8.211	Present
$Li_{0.5}Ga_{2.3}Mn_{0.2}O_4$	8.213	Present
$Li_{0.5}Ga_{2.25}Mn_{0.25}O_4$	8.248	Present, but very weak
$Li_{0.5}Ga_{2.238}Mn_{0.262}O_4$	8.253	Absent
$Li_{0.5}Ga_{2.2}Mn_{0.3}O_4$	8.259	Absent
$Li_{0.5}Ga_{2.0}Mn_{0.5}O_4$	8.273	Absent
$Li_{0.5}Ga_{1.8}Mn_{0.7}O_4$	8.287	Absent
$Li_{0.5}Fe_{2.5}O_4$	8.332	Present
$Li_{0.5}Fe_{2.4}Mn_{0.1}O_4$	8.334	Present
$Li_{0.5}Fe_{2.3}Mn_{0.2}O_4$	8.341	Present
$Li_{0.5}Fe_{2.2}Mn_{0.3}O_4$	8.353	Extremely weak
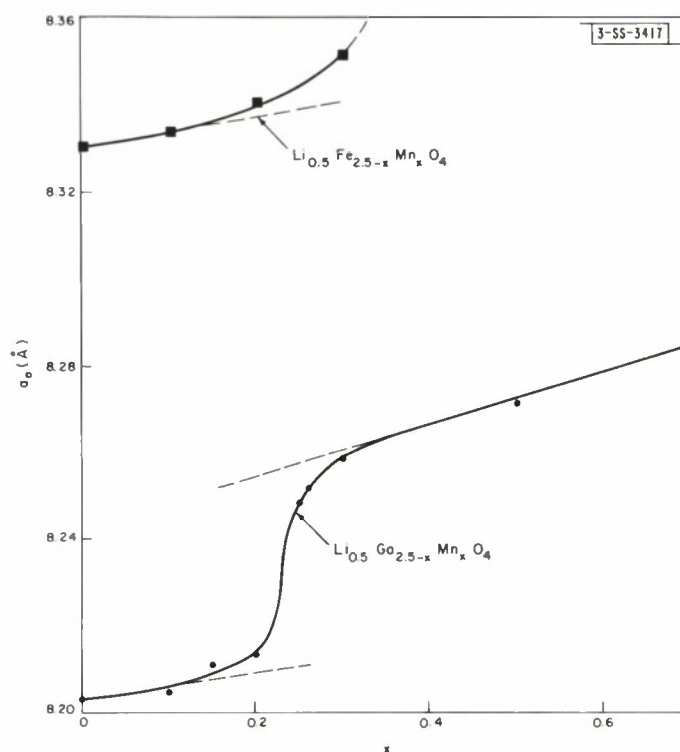
Fig. V-7. Compositional dependence of unit cell edge a_o for the systems $Li_{0.5}Fe_{2.5-x}Mn_xO_4$ and $Li_{0.5}Ga_{2.5-x}Mn_xO_4$.

for such a mechanism would be an intra-cluster Jahn-Teller stabilization that is made possible via cooperative vibrational modes in a cluster of Jahn-Teller ions.

<div align="right">

R. W. Germann
R. J. Arnott
D. B. Rogers

</div>

8. Temperature Dependence of Attenuation of 70-kMcps Acoustic Waves in Quartz

A preliminary analysis has been made of the data obtained from the measured variation with temperature of echo pulse heights of 70-kMcps acoustic waves in x-cut quartz. A log-log plot of the smoothed echo pulse heights gives a temperature dependence of the attenuation very nearly T^4, as shown in Fig. V-8. In order to avoid error that might be introduced by temperature-dependent changes in coupling and excitation, it is desirable to measure the difference in attenuation between a pair of phonon echoes. So far, due to a moderately large, temperature-independent decrement between successive echoes and the large attenuation at the higher temperatures, this has only been possible up to 25°K; up to this temperature the first echo height data give the same result within the experimental error of ±0.5 db.

The observed behavior as a function of temperature and frequency can be compared with that expected on the basis of phonon-phonon scattering theory. At 70 kMcps and at the low temperatures at which the attenuation measurements were made, the condition $\omega\tau \gg 1$ is well
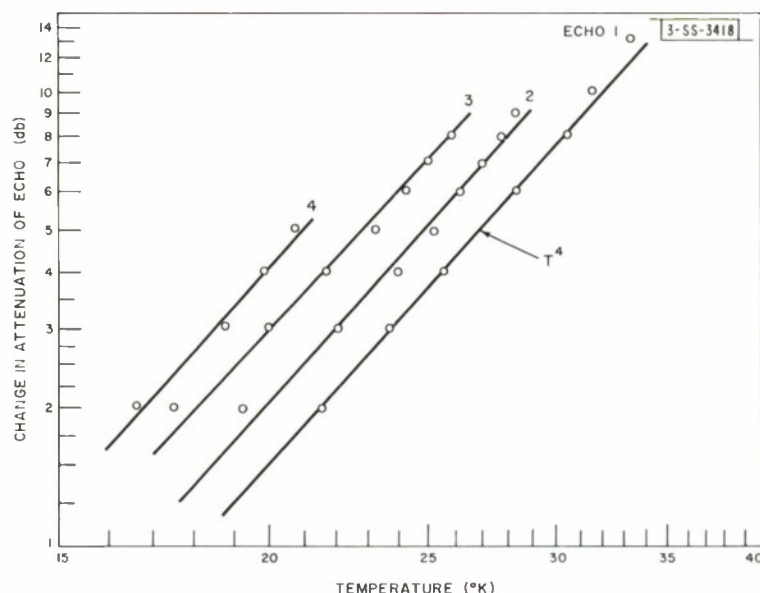
Fig. V-8. Relotive chonge in echo attenuation of temperature for first four echoes observed in x-cut noturol quortz.

satisfied. Here ω is the circular frequency of the acoustic waves and τ is a phonon-phonon scattering time. In this regime, existing theoretical treatments,[24,25] each based on Akhiezer's basic concept that the acoustic wave disturbs the distribution of the thermal phonons, give the same result for the frequency and temperature dependence of the attenuation, namely ωT^4. (The results of Landau and Rumer were derived for transverse waves.)

There exists some disagreement in attenuation data taken at lower frequencies. For example, at 510 Mcps, a T^4 dependence was found in x-cut quartz,[26] whereas T^7 was found at 9 kMcps.[27] However, in the latter case, annealing was shown to have some effect on the intrinsic attenuation. Very recent preliminary results[28] at 9 kMcps give close to a T^4 dependence for both longitudinal and transverse phonons, but the authors point out that the similarity in behavior of longitudinal and transverse wave attenuation is unexpected and requires a new theoretical approach.

It is evident from past experience at 70 kMcps that a more accurate determination of the phonon attenuation can be made with additional measurements and by having optimum performance (simultaneously) of all components of the existing experimental system. The present experiments will be continued to improve the accuracy of the data and to include possible influence of annealing on the attenuation. However, no drastic improvement can be expected using current techniques, which originated with Bömmel and Dransfeld in the low kilomegacycle range;[29] these techniques are approaching the limit of the possible at 70 kMcps. In order to make other physical measurements, modification of these techniques will have to be sought.

J. B. Thaxter
C. D. Parker
P. E. Tannenwald

9. Cyclotron Resonance in PbSe

Cyclotron resonance studies are being performed on single crystals of p-type lead selenide at a frequency of 70 kMcps and at 4.2°K. Measurements are being carried out in the Azbel-Kaner geometry where the magnetic field is parallel to the sample surface. This geometry, usually employed in the study of cyclotron absorption in metals, where the skin depth is small compared to the sample size, is appropriate for PbSe, which is distinctly metallic at liquid helium temperatures.

In preliminary measurements, structure in the absorption curve has been observed at fields below about six kgauss. Efforts are under way to determine whether this structure is attributable to cyclotron-resonance absorption or to other effects. Efforts are also being made to improve the quality of the sample surface by electropolishing and to increase the sensitivity of the micro-wave spectrometer.

<div style="text-align: right">

S. Bermon
W. Kernan

</div>

REFERENCES

1. M.A. Ruderman and C. Kittel, Phys. Rev. 96, 99 (1954).

2. T. Kasuya, Prog. Theor. Phys. 16, 45 (1956).

3. K. Yoshida, Phys. Rev. 106, 893 (1957).

4. K. Yoshida and A. Watabe, Prog. Theor. Phys. 28, 361 (1962).

5. J.W. Cable, E.O. Wollan, W.C. Koehler, and M.K. Wilkinson, J. Appl. Phys. 32, 49S (1961).

6. W.C. Koehler, J.W. Cable, E.O. Wollan, and M.K. Wilkinson, Phys. Rev. 126, 1672 (1962).

7. R.J. Elliott, Phys. Rev. 124, 346 (1961).

8. B.N. Brockhouse and A.T. Stewart, Rev. Mod. Phys. 30, 250 (1958).

9. L.F. Mattheiss, "The Antiferromagnetic Linear Chain," Ph.D. Thesis, Department of Physics, M.I.T. (1960).

10. J.W. Moskowitz, Quarterly Progress Report No. 44, Solid State and Molecular Theory Group, M.I.T. (15 April 1960).

11. A.R. Mackintosh, J. Phys. Chem. 38, 1991 (1963).

12. M.J. Sienko, Paper 21 of Nonstoichiometric Compounds, R. Ward, ed., Advances in Chemistry Series 39 (American Chemical Society, Washington, D.C., 1963), p. 224.

13. J.B. Goodenough, International Colloquium of the Centre National de la Recherche Scientifique, The Oxy-Compounds of the Transition Elements in the Solid State, Bordeaux, France (24-27 September 1964) (to be presented).

14. J. Longo and R. Ward, J. Am. Chem. Soc. 83, 2816 (1961).

15. L.F. Audrieth, Inorganic Syntheses (McGraw-Hill, New York, 1950) Vol. 3, pp. 186, 187.

16. N. Nechamkin, A.N. Kurtz, and C.F. Hiskey, J. Am. Chem. Soc. 73, 2828 (1951).

17. D.G. Wickham and E. Whipple, Talanta 10, 314 (1963).

18. J.P. King and J.W. Cobble, J. Am. Chem. Soc. 79, 1559 (1957).

19. J.B. Goodenough, Phys. Rev. 98, 391 (1955).

20. D.G. Wickham and W.J. Croft, J. Phys. Chem. Solids 7, 351 (1958).

21. P.K. Baltzer, Proceedings of the Conference on Magnetism and Magnetic Materials (American Institute of Electrical Engineers, 1955), p.247.

22. W. Wiechec and C.M. Kelley, J. Appl. Phys. 33, 3054 (1962).

23. G. Blasse, Ph.D. Thesis, University of Leiden (1964), p.8.

24. T.F. Woodruff and H. Ehrenreich, Phys. Rev. 123, 1553 (1961).

25. L. Landau and G. Rumer, Physik. Z. Sowjetunion 11, 18 (1937).

26. T.M. Fitzgerald and R. Truell, "The Interaction of Thermal and Ultrasonic Waves in Insulators and Semiconductors," Brown University, Metals Research Laboratory Technical Note (April 1963).

27. R. Nava, R. Arzt, I. Ciccarello, and K. Dransfeld, Phys. Rev. 134, A581 (1964).

28. A.H. Nethercot, M. Pomerantz, and N.S. Shiren, "Phonon Interactions in Crystals," IBM Report No.3 (15 February 1964).

29. H.E. Bömmel and K. Dransfeld, Phys. Rev. Letters 2, 298 (1959).

DOCUMENT CONTROL DATA - R&D

(Security classification of title, body of abstract and indexing annotation must be entered when the overall report is classified)

1. ORIGINATING ACTIVITY (Corporate author)	2a. REPORT SECURITY CLASSIFICATION
Lincoln Labs., Lexington, Mass.	UNCLASSIFIED
	2b. GROUP N/A

3. REPORT TITLE

Solid State Research

4. DESCRIPTIVE NOTES *(Type of report and inclusive dates)*

None

5. AUTHOR(S) *(Last name, first name, initial)*

None

6. REPORT DATE	7a. TOTAL NO. OF PAGES	7b. NO. OF REFS
Sep 64	96	80

8a. CONTRACT OR GRANT NO.	9a. ORIGINATOR'S REPORT NUMBER(S)
AF19(628)500	
b. PROJECT NO.	
c.	9b. OTHER REPORT NO(S) (Any other numbers that may be assigned this report)
d.	ESD-TDR-64-351

10. AVAILABILITY/LIMITATION NOTICES

Qualified Requesters May Obtain Copies From DDC.

11. SUPPLEMENTARY NOTES	12. SPONSORING MILITARY ACTIVITY
	ESD, L.G. Hanscom Field, Bedford, Mass.

13. ABSTRACT

A summary of Solid State Research to date.

DD FORM 1 JAN 64 1473

14. KEY WORDS	LINK A		LINK B		LINK C	
	ROLE	WT	ROLE	WT	ROLE	WT
Solid State Laser Research Radiation Materials Magnetism Physics						

INSTRUCTIONS

1. ORIGINATING ACTIVITY: Enter the name and address of the contractor, subcontractor, grantee, Department of Defense activity or other organization (corporate author) issuing the report.

2a. REPORT SECURITY CLASSIFICATION: Enter the overall security classification of the report. Indicate whether "Restricted Data" is included. Marking is to be in accordance with appropriate security regulations.

2b. GROUP: Automatic downgrading is specified in DoD Directive 5200.10 and Armed Forces Industrial Manual. Enter the group number. Also, when applicable, show that optional markings have been used for Group 3 and Group 4 as authorized.

3. REPORT TITLE: Enter the complete report title in all capital letters. Titles in all cases should be unclassified. If a meaningful title cannot be selected without classification, show title classification in all capitals in parenthesis immediately following the title.

4. DESCRIPTIVE NOTES: If appropriate, enter the type of report, e.g., interim, progress, summary, annual, or final. Give the inclusive dates when a specific reporting period is covered.

5. AUTHOR(S): Enter the name(s) of author(s) as shown on or in the report. Enter last name, first name, middle initial. If military, show rank and branch of service. The name of the principal author is an absolute minimum requirement.

6. REPORT DATE: Enter the date of the report as day, month, year; or month, year. If more than one date appears on the report, use date of publication.

7a. TOTAL NUMBER OF PAGES: The total page count should follow normal pagination procedures, i.e., enter the number of pages containing information.

7b. NUMBER OF REFERENCES: Enter the total number of references cited in the report.

8a. CONTRACT OR GRANT NUMBER: If appropriate, enter the applicable number of the contract or grant under which the report was written.

8b, 8c, & 8d. PROJECT NUMBER: Enter the appropriate military department identification, such as project number, subproject number, system numbers, task number, etc.

9a. ORIGINATOR'S REPORT NUMBER(S): Enter the official report number by which the document will be identified and controlled by the originating activity. This number must be unique to this report.

9b. OTHER REPORT NUMBER(S): If the report has been assigned any other report numbers (either by the originator or by the sponsor), also enter this number(s).

10. AVAILABILITY/LIMITATION NOTICES: Enter any limitations on further dissemination of the report, other than those

imposed by security classification, using standard statements such as:

(1) "Qualified requesters may obtain copies of this report from DDC."

(2) "Foreign announcement and dissemination of this report by DDC is not authorized."

(3) "U. S. Government agencies may obtain copies of this report directly from DDC. Other qualified DDC users shall request through

_____ ."

(4) "U. S. military agencies may obtain copies of this report directly from DDC. Other qualified users shall request through

_____ ."

(5) "All distribution of this report is controlled. Qualified DDC users shall request through

_____ ."

If the report has been furnished to the Office of Technical Services, Department of Commerce, for sale to the public, indicate this fact and enter the price, if known.

11. SUPPLEMENTARY NOTES: Use for additional explanatory notes.

12. SPONSORING MILITARY ACTIVITY: Enter the name of the departmental project office or laboratory sponsoring (paying for) the research and development. Include address.

13. ABSTRACT: Enter an abstract giving a brief and factual summary of the document indicative of the report, even though it may also appear elsewhere in the body of the technical report. If additional space is required, a continuation sheet shall be attached.

It is highly desirable that the abstract of classified reports be unclassified. Each paragraph of the abstract shall end with an indication of the military security classification of the information in the paragraph, represented as (TS), (S), (C), or (U).

There is no limitation on the length of the abstract. However, the suggested length is from 150 to 225 words.

14. KEY WORDS: Key words are technically meaningful terms or short phrases that characterize a report and may be used as index entries for cataloging the report. Key words must be selected so that no security classification is required. Identifiers, such as equipment model designation, trade name, military project code name, geographic location, may be used as key words but will be followed by an indication of technical context. The assignment of links, rules, and weights is optional